# Semi-analytical Methods of Orbit Propagation for Near-Earth Asteroids

by

**O. Fuentes-Muñoz**

B.S., Universitat Politècnica de Catalunya, 2017

M.S., University of Colorado Boulder, 2019

A thesis submitted to the

Faculty of the Graduate School of the

University of Colorado in partial fulfillment

of the requirements for the degree of

Doctor of Philosophy

Department of Aerospace Engineering Sciences

2023

Committee Members:

Daniel J. Scheeres, Chair

Jay W. McMahon

Hanspeter Schaub

David Nesvorný

Davide Farnocchia

Fuentes-Muñoz, O. (Ph.D., Aerospace Engineering Sciences)

Semi-analytical Methods of Orbit Propagation for Near-Earth Asteroids

Thesis directed by Prof. Daniel J. Scheeres

The long-term dynamics of Near-Earth Objects (NEOs) are driven by the secular perturbations of the solar system and the presence of planetary close encounters. Close encounters with the inner solar system planets cause the orbits of NEOs to become chaotic, thus we study their long-term evolution stochastically. We combine analytical solutions of the long-term secular perturbations with the numerical evaluation of close encounters, allowing the rapid propagation of NEO orbit trajectories. Using the semi-analytical propagation tool we obtain statistics of the orbit long-term dynamics, characterizing their stochastic behavior.

Many of the physical properties of NEOs evolve over time. This evolution is usually coupled with the orbit evolution through close encounters, long-term effects, or at least conditioned by the location of the asteroid within the solar system. Planetary close encounters excite the relative orbits of binary asteroids. Using the semi-analytical propagation we gather statistics of the close encounters. Combined with models for the excitation of binaries we compute the probability of experiencing encounters that disrupt binary systems. We conduct this analysis for the NASA Janus and NASA/APL DART mission targets.

The rotational state of asteroids evolves under thermal torques or YORP effect. This effect depends on the obliquity, the angle between the spin pole and the orbit plane. YORP theories predict that the spin poles is torqued into equilibrium obliquities of 0, 90 or 180 degrees. Modeling the obliquity component of the torque while propagating the orbit with the semi-analytical model we obtain oscillations in obliquity that are near but offset from the equilibrium configurations.

We characterize the long-term impact hazard of asteroids by propagation of the Minimum Orbit Intersection Distance (MOID). The MOID limits the closest encounters that can occur and its uncertainty grows much slower than the overall uncertainty in the position of asteroids. Thus,

we can extend the timescales of typical impact characterization analyses. We combine analytical estimates of the intrinsic probability of collision with the propagation of the orbits to rank the km-sized NEO population and PHAs, large asteroids ($H < 22$) currently with an Earth MOID $< 0.05$au.

The analytical theories of planetary close encounters assume a constant MOID to find keyholes, regions that lead to a future impact. We analyze different models for the evolution of the MOID as corrections to the analytical theory. We find that the short-period oscillations and shallow encounters play a significant role in the definition of keyholes, as the variations can be in the order of tens of Earth Radii in a few years.

## Dedication

To my parents Lola and Chesco, who believed with conviction in the importance of higher education even if they did not have opportunities for themselves. To you and my brother Victor, without your support I wouldn't be writing these lines today.

To my grandparents, who immigrated looking for a better future for their kids and generations to follow. Especially for la iaia Carmen, who with her great heart took care of me and my cousins in countless occasions and left us during the pandemic.

To all other Fuentes and Muñoz, with whom we looked up to the stars and down to Earth for opportunities such as this one.

To my support circle in Boulder: my Caldi second family, John, the Balsells/hispanic community, all my CSML and CCAR friends, the ritmos community, and CAPS. Thank you for being there in the hard times, through fire, snow, a pandemic and many other uncertainties.

To Carolina, for your love and support in the past, present and future.

I'm deeply grateful to you all,

*Moltíssimes gràcies a tots,*

## Acknowledgements

This dissertation was the product of many years of work and crucial support that I will try to acknowledge in one page. First, prof. Dan Scheeres, thank you for the opportunity and guidance along the way. It has been an honor and a pleasure to learn from your problem-solving and academic philosophies. I want to thank my committee, Prof. McMahon, Prof. Schaub, Dr. Nesvorný and Dr. Farnocchia for their time and helpful feedback. Thanks to Prof. Bosanac for her feedback as member of the committee of my comprehensive exam.

My graduate education was initially funded by the Balsells Fellowship Program, an invaluable kick-starter for my academic career as international student. Then, this research has been supported by missions NASA Janus, DART and the AIDA collaboration, grant support from JPL and NASA's YORPD program, and the ASEN department at CU Boulder. Thank you Drs. Park and Farnocchia for allowing me to work with you at JPL's SSD Group. Just a few years ago I couldn't have conceived all of these amazing opportunities.

The Smead Aerospace Engineering Sciences Dept. and CU have given me the opportunity to become an educator as part of my doctoral training, an opportunity for which I am very grateful. Thank you, Profs. Mah, Glusman and Schaub for being educational role models that I look up to.

It took a lot of referents and support to continue in higher education all the way to a PhD. I want to thank the late Prof. García-Berro from UPC for his encouragement and mentoring, he is dearly missed; as well as Prof. Muntanya for my first research experiences as undergrad at UPC. Last, me and my family couldn't have made it this far without a high-quality universal public education system and a universal health care system, which laid out the conditions for this success.

# Contents

**Chapter**

# Tables

**Table**

# Figures

**Figure**

# Chapter 1

# Introduction

The study of asteroids is an opportunity to learn about the origin of the solar system as they are remnants of primordial planetary formation. In addition, asteroids are considered as potential resources for space exploration. More existentially, the risk of a natural disaster by an asteroid impact can be mitigated if properly characterized. All of these opportunities are more or less accessible to humankind depending on the orbits of the asteroids. Near-Earth objects (or NEOs, asteroids or comets with $q < 1.3$ au) are the most accessible, and have been explored from ground-based telescopes, space-based telescopes and in-situ exploration missions, both as flybys and rendezvous missions.

From less than a 1000 NEOs being discovered in the 20th century, as of 2023 there are 32,000 discovered NEOs, with half of them being discovered in the last 6 years. Figure 1.1 shows the current estimated completeness of the NEO catalog as function of size. The kilometer-sized population is believed to be almost completely discovered, whereas the 140 m of diameter population is roughly 40% discovered. At even smaller sizes, the percentage is greatly reduced because of the difficulty to discover such faint bodes. The frequencies of impacts from asteroids that are km-sized, 140 m, or 50 m, is respectively of $\sim$1 million years, 20,000 years and 1000 years.

The next generation of surveys is expected to increase the total number of NEOs by another order of magnitude [Jones et al., 2018], which will multiply these opportunities for humanity. The rapid analysis of the impact hazard and the detection of relevant scientific assets will be more necessary as these new generations of datasets become available to the community.

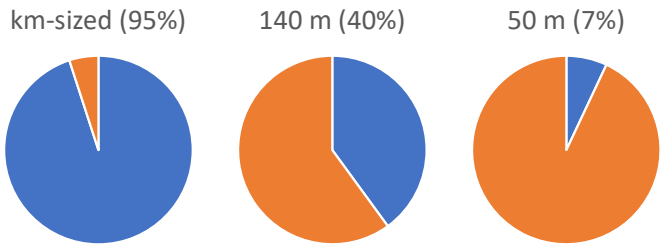


Figure 1.1 Discovery rates of NEOs by size. Source: NASA and FEMA Planetary Defense TTX4 Read-ahead materials, February 2022.

## 1.1 Orbit long-term dynamics of NEOs

One of the main characteristics of the orbits of near-Earth asteroids is that they experience planetary close encounters while being drifted by secular perturbations [Michel et al., 1996b]. Planetary close encounters have a variety of effects: from abrupt changes in the orbits to changes in the physical properties such as their spin states, the relative orbit of binary asteroids or changes in their surfaces. The changes due to planetary close encounters are very sensitive to the initial conditions, i.e., predictions of the past or future evolution can become chaotic [Tancredi, 1998]. After many planetary close encounters the orbits of near-Earth asteroids become stochastic and must be studied statistically. For example, the origin of asteroids coming into the inner solar system is expressed by the probability of the different source regions over millions of years [Granvik et al., 2018]; or the probability of an Earth collision is obtained as the result of large Monte Carlo simulations from the uncertainties of their orbits [Chamberlin et al., 2001, Roa et al., 2021].

The orbital motion of near-Earth asteroids is driven by different dynamical effects, which dominate in different timescales. Asteroids move under the gravitational force of the Sun and, in general, the long-term perturbations are dominated by the gravitational forces of the gas giants. The secular components of these contributions are characterized by cycles of $\sim$100,000 years, which define hundreds-to-thousand year windows when close encounters with the terrestrial planets are possible. In the NEO regime and these timescales, smaller force contributions such as the Yarkovsky acceleration can be shadowed by the stochastic growth in uncertainty. However, these must be considered in short-term timescales of decades-to-hundreds of years.

These dynamical effects define the orbit propagation tools that can be used to predict the past or the future evolution of near-Earth asteroids. These range from the highest fidelity in numerical integration for precise probability of collision predictions [Farnocchia et al., 2015] to analytical estimates [Öpik, 1951, Wetherill, 1967]. The amount of information required also ranges from spacecraft in-situ measurements to only a few ground-based astrometric observations, as well as the computational expense of producing such predictions.

The orbits of NEOs are poorly determined far from the observation dates because of the sensitivity of the orbits to planetary close encounters. The uncertainty grows the largest along the direction of motion, meaning that the future position of the asteroid along its orbit is the hardest to determine. This justifies models for the uncertainty like the line-of-variations [Milani et al., 2005, Del Vigna et al., 2020], in which the uncertainty is sampled alone a 1-D line that captures the spread along the orbit. However, the variation of the heliocentric orbit is not expected to be as large in the absence of deep planetary close encounters.

## 1.2 Planetary close encounters and impact hazard

The conditions for an impact between two objects can be split in two: first, the orbits of the two must intersect; then, they must meet at the intersection point at the same time. Given the first condition, a very useful metric is the Minimum Orbit Intersection Distance (MOID), the minimum distance between any two points of the orbits of the two bodies. Thus, it indicates the closest possible encounter between them.

Figure 1.2 illustrates these two conditions. First, we need the MOID to be smaller than the radius of the Earth with any gravitational focusing factor. The snapshot of the orbit of 2008 TC3 is shown 2 months before its Earth impact and disintegration over the desert of Sudan [Jenniskens et al., 2009].[1] This was the first time in history that an asteroid was discovered prior to its Earth impact, a situation that has been repeated 6 times since.

[1] Snapshot generated using JPL's Small-Body Database Lookup Tool - Available online at `ssd.jpl.nasa.gov/tools/sbdb_lookup.html`

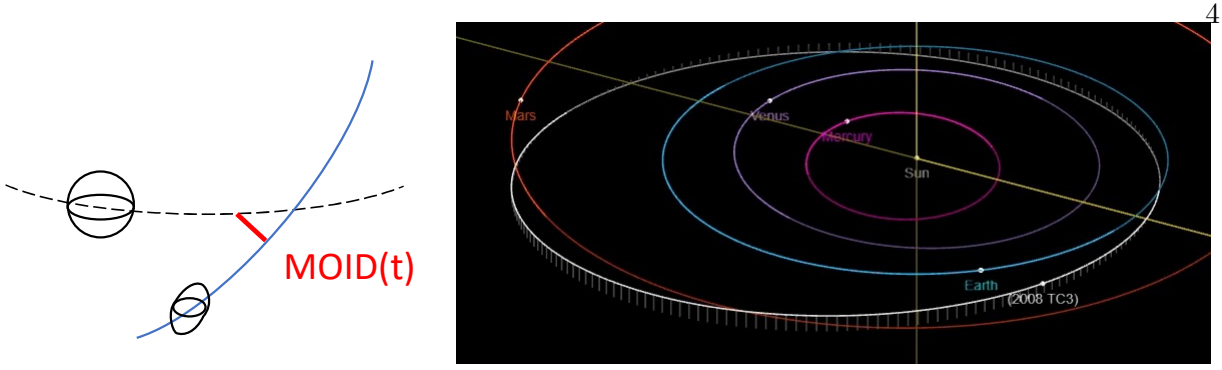


Figure 1.2 Necessary conditions for a collision. Orbit of 2008 TC3 2 months before Earth impact. Source: JPL's Small-Body Database Lookup.

The MOID is currently used to catalog asteroids that are close enough to the Earth to be considered a potentially hazardous or PHA (MOID $< 0.05$ au). The other condition is that they must be large enough to cause regional damage in case of an Earth collision ($H < 22$, $\sim$140 m). There are a few algorithms in the literature to compute the MOID [Gronchi, 2005, Hedo et al., 2018, Wiśniowski and Rickman, 2013]. The evolution of the MOID has been studied in the past for the double averaged 3BP and focusing on the regularization of the evolution when it comes to 0 [Gronchi and Tardioli, 2013, Gronchi and Tardioli, 2011].

The mitigation of the hazards of asteroid impacts is the main goal of planetary defense efforts. The main planetary defense efforts are in asteroid surveying, characterization and deflection. As the near-Earth asteroid catalog is being completed by current and proposed surveys, they provide new candidates of a future collision to study in more detail. Once new observations of NEOs become available, their probability of collision is computed typically for 100 years and made publicly available [Roa et al., 2021]. During a planetary close encounter, asteroids can cross keyholes, regions that lead to a future collision or deep encounter [Chodas, 1999]. The analytical theories to compute the location of keyholes typically assume the MOID to be constant between encounters [Valsecchi et al., 2003].

In long-term predictions the fast angles become completely unknown. Thus, it is common to model them with a uniform distribution. The latter assumption is frequently used to compute probabilities of collision in the order of magnitude of the lifetimes of near-Earth asteroids, which

are on the order of millions of years[Vokrouhlický et al., 2012, Pokorný and Vokrouhlický, 2013, JeongAhn and Malhotra, 2017].

## 1.3 Physical properties of NEOs

The physical properties of NEOs can be used to constrain the orbit history of NEOs. For example, the cratering history informed of the lifetime of the NEO [Ballouz et al., 2020]. Figure 1.3 shows physical properties of binary asteroid system Didymos. The spin state can be characterized by the rotational angular momentum or spin pole and spin rate. Mission NASA/JHAPL DART allowed to briefly observe the shape and surface of Dimorphos, the secondary or satellite of the Didymos system. All of these properties are subject to impulsive excitation during very close planetary close encounters. In addition, some of them also evolve coupled to the long-term dynamical evolution of the orbit.

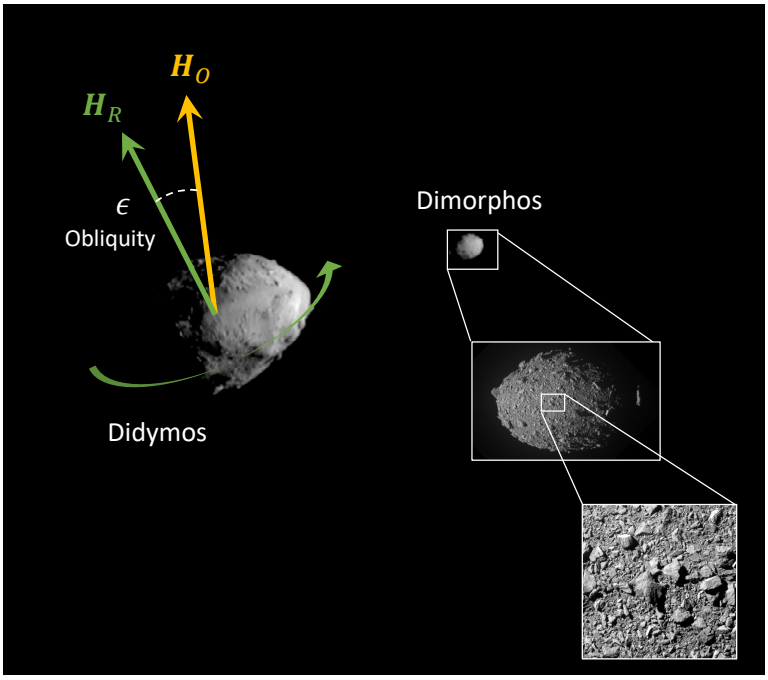


Figure 1.3 Didymos system as imaged by DART. Credit: NASA, JHUAPL.

Asteroids in the inner Solar System experience accelerations and torques as a result of solar radiation pressure, thermal absorption and re-emission. The resulting acceleration from thermal radiation and re-emission is called Yarkovsky effect. The resulting torque is the YORP effect (Yarkovsky–O'Keefe–Radzievskii–Paddack), usually assumed as the resultant torque from solar radiation pressure applied on the surface with negligible thermal inertia [Vokrouhlický et al., 2015]. Both Yarkovsky and YORP effects depend on obliquity, the angle between the orbit normal and rotational angular momentum. Measuring the Yarkovsky acceleration can be one of the main factors for impact hazard characterization [Farnocchia et al., 2021, Farnocchia and Chesley, 2022].

The YORP effect has many influences in the physical properties of asteroids: as asteroids spin up, particles can be ejected, satellites can be formed, contact binaries can experience a fission into binary asteroids, or the asteroid can be completely disrupted [Walsh et al., 2012, Scheeres, 2007, Sánchez and Scheeres, 2016]. The effects of the spin-up can be observed in the surface by effects such as the change in slopes [Bottke et al., 2006] or generation of cavities [Tardivel et al., 2018]. In addition, the rotational accelerations can give information of the internal structure of asteroids [Scheeres et al., 2007, Scheeres and Gaskell, 2008, Lowry et al., 2014], and change the dynamical environment around asteroids [Brown and Scheeres, 2023]. Binary asteroids also experience secular variations in their orbit, in what is called Binary YORP or BYORP [McMahon and Scheeres, 2010].

The relative orbits of binary asteroids are sensitive to the perturbations, such as planetary close encounters. This sensitivity makes them good test cases for a planetary defense missions such as NASA/JHAPL DART [Rivkin and Cheng, 2023], which measured the change in the relative orbital period after a spacecraft kinetic impact. We also find binary asteroids in nature that are in a chaotic spin-orbit state, such as (35107) 1991 VH [Pravec et al., 2016, Scheeres et al., 2020].

## 1.4 Outline

### 1.4.1 Thesis Statement

The semi-analytical propagation of Near-Earth Objects (NEOs) orbits will allow a fast and accurate description of their long-term dynamics as driven by planetary secular perturbations and close encounters. The characterization of planetary close encounters and their frequency will improve our understanding of the evolution of their physical properties and hazardous nature.

### 1.4.2 Dissertation Overview

Chapter 2 describes the semi-analytical orbit propagation tool developed in this dissertation. We compare the propagations using this tool to numerical integration to define a range of applicability and performance. Then, in Chapter 3 we apply it to the study of binary asteroids considering the changes in the orbits of binaries during close encounters. In Chapter 4 we propagate the orbits of asteroids and introduce torques to the rotational angular momentum. This study allows us to model the disturbed equilibrium at which we find the obliquities of near-Earth asteroids. Next, we explore planetary defense applications by studying the hazardous nature of asteroids on two different timescales considering different models for the long-term dynamics of the MOID. First, in Chapter 5, we find the hazardous km-sized NEOs of the next thousands of years proposing a new metric to rank NEOs by their long-term impact hazard probability. Then, we visit the PHA definition to highlight the dynamical nature of this metric in centuries-to-thousands of years. In Chapter 6 we aim to extend analytical Öpik theory of close encounters to find keyholes. We inspect the variation of the MOID between encounters, in timescales of decades. Last, we present our concluding remarks in Chapter 7.

### 1.4.3 Contributions

In this dissertation we developed a semi-analytical propagation tool to rapidly generate time histories of the orbits and close encounters experienced by near-Earth objects. Then, we combine

this information with models for the evolution of physical properties of asteroids. We study the evolution of the Earth MOID as a tool for impact hazard characterization. Overall, in this dissertation we made contributions to the fields of astrodynamics, planetary science and planetary defense, as described next:

In chapter 2 we present a novel propagation tool that allows us to gather statistics of the orbit evolution of near-Earth asteroids in similar fashion as numerical integration, but in a small fraction of the computational time. The computational speed-up propagating 1 particle is found to be of x500-x1000. This allows a flexible use of the tool to gather statistics of close encounters at the desired timescales without having to assume a constant distribution from the asteroid's proper elements or distribution of orbits in its lifetime.

In chapter 3 we demonstrate this approach to compute probabilities of close encounters in thousands of years for a few binary asteroid systems. This prediction in intermediate timescales is needed if the excited state of binary systems was to be caused by close encounters, as in longer timescales these perturbations can dissipate. These methods provide a time-varying distribution of encounters beyond assuming the initial orbit elements or the whole lifetime. This allows us to better understand the recent encounter history of asteroids.

Throughout this dissertation we contributed to the general knowledge of the growth in uncertainty in the orbit of NEOs. In chapters 2 and 3 we show how a random walk can be assumed for semi-major axis, eccentricity and inclination with different timescales depending on the location in near-Earth space. In addition, many analytical theories in the literature assume a uniform distribution of the mean anomaly of the asteroid to compute a probability of collision. In chapter 5 we study how the uncertainty grows from the deterministic part of the propagation all the way to being uniformly distributed. This method bridges the gap between analytical long-term theories and deterministic hazard characterization thanks to the propagation of the MOID between these timescales.

Analytical theories of the evolution of the spin state of asteroids suggest that the obliquities of asteroids under YORP torques go to 0, 90, or 180 deg. In chapter 4 we model the obliquity

component of these torques and predict an offset from equilibrium as more frequently observed in nature. This is a step in the realistic modeling of the long-term dynamics of the spin state of asteroids. The spin rate components of these torques are left as future work.

Chapters 5 and 6 describe our contributions to planetary defense, built on the time propagation of the MOID. The evolution of the MOID was modeled on an individual case basis in the literature. In addition, operational impact monitoring systems typically characterize the hazard for 100 years. Our estimated probability of collision allowed us to rank the km-sized population and to highlight how the PHA category, that assumes a constant MOID threshold, will vary over time.

In chapter 6 we explore the problem of finding keyholes via the exploration of the B-plane. The Öpik theory of resonant close encounters assumes a constant MOID ($\xi$) between encounters. We use the models of chapter 2 as corrections to the theory to model the change in MOID between encounters. In this process we provide novel insight into the dynamics of the MOID. For example, by quantifying the secular rate in the MOID, the amplitude of short-period components, or how the MOID varies along a resonant circle or across the B-plane. These contributions extend the insight of analytical theories for a fast assessment of the hazard of resonant encounters.

### 1.4.4 Publications

**Journal Publications**

This dissertation is comprised of the following publications:

- Fuentes-Muñoz, O., Meyer, A. J., & Scheeres, D. J. (2022). Semi-analytical near-Earth objects propagation: the orbit history of (35107) 1991 VH and (175706) 1996 FG3. The Planetary Science Journal, 3(11), 257. `https://doi.org/10.3847/PSJ/ac83c6` - [Fuentes-Muñoz et al., 2022]

- Fuentes-Muñoz, O., Scheeres, D. J., Farnocchia, D., & Park, R. S. (2023). The hazardous

km-sized NEOs of the next thousands of years. The Astronomical Journal, 166(1):10. https://doi.org/10.3847/1538-3881/acd378 - [Fuentes-Muñoz et al., 2023]

- Richardson, D.C., Agrusa, H.F., ..., **Fuentes-Muñoz, O.**, ..., Tsiganis, K., & Zhang, Y (2022). Predictions for the Dynamical States of the Didymos System before and after the Planned DART Impact. The Planetary Science Journal, 3(7):157, https://dx.doi.org/10.3847/PSJ/ac76c9 - [Richardson et al., 2022]

In addition, the following publications are currently in review or preparation:

- Fuentes-Muñoz, O. & Scheeres, D. J. The disturbed equilibrium of NEA obliquities under stochastic orbital motion (In preparation)
- Fuentes-Muñoz, O., Pedrós-Faura, A., Amato D., Scheeres, D.J., McMahon J.W. Effect of MOID evolution on preliminary keyhole analyses (In preparation)

**Conference Papers**

- Fuentes-Munoz, O. & Scheeres, D.J. (2022). On the long-term hazardous nature of NEOs, AAS 22-672. 2022 AAS/AIAA Astrodynamics Specialist Conference. August 2022. - [Fuentes-Muñoz and Scheeres, 2022]
- Fuentes-Munoz, O., Pedros-Faura, A. & Amato, D. (2021). Effect of non-Keplerian MOID evolution on preliminary keyhole analyses. 7th IAA Planetary Defense Conference. April 2021. - [Fuentes-Munoz et al., 2021]
- Fuentes-Munoz, O. & Scheeres, D.J. (2020). Secular Evolution of the MOID for Near-Earth Objects, AAS 20-584. 2020 AAS/AIAA Astrodynamics Specialist Conference. August 2020. - [Fuentes-Munoz and Scheeres, 2020a]

- Fuentes Munoz, O. & Scheeres, D.J. (2020). Extremely long-term asteroid propagation, AIAA 2020-0464. AIAA Scitech 2020 Forum. January 2020. https://arc.aiaa.org/doi/abs/10.2514/6.2020-0464 - [Fuentes-Munoz and Scheeres, 2020b]

# Chapter 2

# Semi-analytical Orbit Propagation

## 2.1 Introduction

The long-term study of asteroid orbits has been achieved in the past using a wide variety of analytical, semi-analytical and numerical methods. Analytical methods are based on the study of the gravity potential to obtain secular and resonant perturbations [Milani and Knežević, 1990]. Semi-analytical methods are used to map orbital elements to the locations of linear secular resonances, which are resonances involving one planetary and one asteroid frequency [Michel et al., 1997, Michel and Froeschlé, 1997]. Both types of solutions represent the dynamics of asteroids in the absence of planetary encounters by averaging the perturbing potential.

On the other hand, previous studies focus on the accumulation of planetary encounters in contrast to numerical integration [Dones et al., 1999]. The effect of close encounters on the orbit of asteroids can be computed using analytical [Öpik, 1976], semi-analytical or numerical methods. Semi-analytical solutions [Alessi and Sánchez, 2015] allow the computation of flybys treating the planet as a perturbing force in the Lagrange Planetary Equations. Specific numerical integrators are convenient to propagate orbits of asteroids in the long-term, in which symplecticity is desired along with the capacity to accurately solve close encounters [Wisdom and Holman, 1991, Chambers, 1999]. Under multiple resonances asteroids start to encounter planets while their eccentricity increases. This increase often causes the asteroids to eventually collide with the Sun, planets or to be ejected from the Solar System on a hyperbolic orbit [Farinella et al., 1994, Gladman et al., 1997, Milani et al., 1989, Dones et al., 1999, Michel et al., 2005].

In this chapter we aim to provide a simulation framework for the propagation of particles in the Solar System. Our approach consists in the analytical propagation of the particle until a close encounter is found. The propagation is stopped when the trajectory is close to a planet, then the close encounter is evaluated numerically. The evaluation of the encounters is based on a quadrature of the Lagrange Planetary Equations (LPE) around the closest approach date. After the encounter the analytical propagation of the orbit is resumed. The propagation under secular perturbations provides a realistic prediction of when the next encounter can occur as the orbit of the asteroid drifts between different regions of the inner Solar System. This approach reduces substantially the computational time of solutions obtained entirely by numerical integration while providing deeper insight into the dynamics.

The use of the analytical secular model allows the prediction of long-term properties of the asteroid dynamics. Eccentricities, inclinations and angles of asteroid and planets drift secularly. Thus, we can propagate the minimum orbit intersection distance (MOID). The MOID constrains the minimum closest approach distance between the asteroid and the planets and defines if asteroids are potentially hazardous (PHAs). The long-term dynamics of the orbits of NEOs and the MOID are studied by sampling a large number of virtual asteroids from their uncertainty distributions. We use the semi-analytical propagation of these asteroids to show the stochastic nature of the orbital evolution of NEOs.

This chapter is organized as follows. Section 2.2 provides additional background of the long-term dynamics of NEOs in the inner Solar System. Next, section 2.3 describes the propagation methodology including a detailed study of flybys evaluation and the derivation of an analytical N-body secular problem solution. Section 2.4 shows examples of the long-term propagation of asteroids and how the long-term dynamics can be characterized stochastically. Section 2.5 discusses the limitations of the semi-analytical propagation tool. Last, section 2.6 concludes by evaluating the aspects in which this methodology proves beneficial, questions that remained unanswered, and future work with respect to the orbit propagation methodology.

## 2.2 Background

The long-term dynamics of NEOs are governed by their gravitational interactions with the other bodies of the Solar System. The effects of the most massive and external planets have timescales of millennia. However, planetary close encounters can abruptly change an orbit over a timescale of days. The accumulation of such planetary encounters causes the orbits of NEOs to be chaotic [Tancredi, 1998]. This section describes this phenomenon in more detail. The evaluation of close encounters is necessary for the propagation of NEOs, hence the variety of possible flybys is demonstrated later for the validation of the method.

Many asteroids experience long periods of time without flybys. The dominant dynamics in those periods of time are the secular perturbations from massive planets in the Solar System. Likewise, the orbits of the planets evolve secularly over similar timescales. The Laplace-Lagrange secular theory qualitatively describes the evolution of the elements of the planets at any distant time in the future or past. As for the asteroid, the secular solution from external perturbers represents the orbital dynamics of asteroids between encounters.

The presence of repeated encounters is one of the main characteristics of the long-term propagation of asteroids in the inner Solar System. Repeated close encounters cause a random walk in the elements of the asteroids. Very close encounters occur less frequently but change substantially the orbits of NEOs, modifying predictions on the long-term evolution of their orbits. Thus, we propose an informed analytical propagation of the orbits while characterizing planetary close encounters. The proposed methodology is born from the combination of these two dynamical regimes: the long-term effects of secular dynamics and the frequent changes in elements experienced in planetary encounters. Considering the secular drift of the asteroid we model the seasonal variation of the possible encounters with planets.

### 2.2.1 Chaotic dynamics in the inner Solar System

An accurate description of the evolution of orbits of near-Earth asteroids beyond a few centuries is challenging. This is because the succession of planetary encounters disperse neighboring trajectories to become chaotic [Tancredi, 1998]. Small deviations in the orbital period change the timing of the flybys, spreading the uncertainty along the Line of Variation [Milani et al., 2005]. After successive flybys the resulting imaginary stream of particles is spread in highly non-linear distributions. For this reason the study of long-term dynamics is often left to a statistical analysis requiring a large number of particles and computational efforts. In this context we propose the use of this semi-analytical tool to obtain long-term simulations in short computational times.

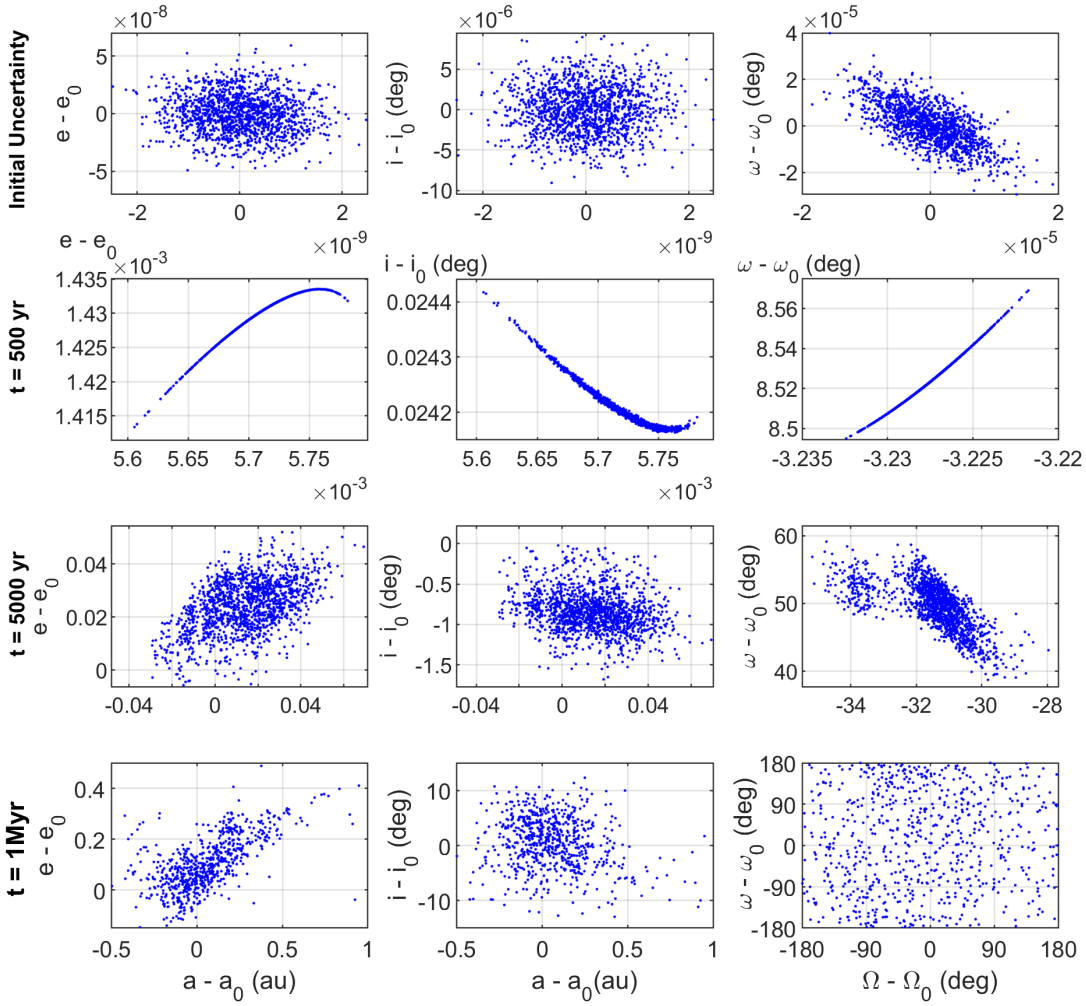


Figure 2.1 Chaotic dynamics of (35107) 1991 VH as obtained from numerical integration.

We exemplify the sensitivity to initial conditions in a numerical integration of asteroid (35107) 1991 VH, which is one of the two targets of mission Janus [Scheeres et al., 2020], a NASA SIMPLEx mission. Figure 2.1 shows 1440 particles generated from the uncertainty in the orbit solution of (35107) 1991 VH, which is included in appendix B. These particles are propagated in the N-body integrator IAS15 [Rein and Spiegel, 2014] including the Solar System planets from Venus to Neptune. The particles are propagated for a million years, although in this section we study in more detail the distributions after shorter periods of time. Each axis represents the variation from the initial value of elements pairs: (left) semi-major axis-eccentricity, (center) semi-major axis-inclination, (right) argument of the node-argument of perihelion in degrees. The orbital evolution is shown at four instants of time: initial (first row), after 500 years (second row), after 5000 years (third row) and after 1 million years (bottom).

After 500 years the initial normal distribution already becomes a stream of particles. While the variation in the elements from the nominal is similar for all the particles, there is a dispersion orders of magnitude smaller that represents the stream of particles. After 5000 years, the distribution becomes completely different: the presence of planetary encounters disperses the particles around the initial orbit. The variation in eccentricities and inclinations has a secular component. However, the variation on the argument of the node and argument of perihelion is dominantly secular after a few millennia. After a million years, the particles are spread along a large region of near-Earth space. In argument of perihelion and ascending node we observe that the distribution becomes almost uniform in the whole 2D angular space.

The secular drift in the arguments defines the possibility of encounters over time. For this reason, it is important to characterize this drift and the secular cycles under the perturbation of the large bodies of the Solar System. When encounters are possible with the inner Solar System planets, these need to be accounted as perturbers of the orbit evolution.

The stochastic nature of the long-term dynamics of NEOs under close encounters implies that the precise determination of their position after hundreds of thousands of years is unachievable. However, we can still collect statistics that give us insight on their orbital history. Another impli-

cation is that the inclusion of higher order dynamics is shadowed under the stochastic dispersion caused by the main gravitational perturbations. For example, the magnitude of the Yarkovsky effect is typically $10^{-4}$ au/Myr [Vokrouhlický et al., 2000, Nesvorný and Bottke, 2004], which is still two orders of magnitude smaller than a typical dispersion after 10,000 yr under repeated close encounters, as observed in the example of Figure 2.1. In section 3.2.1 we show that (35107) 1991 VH is not under a particularly high frequency of close encounters compared to other NEOs.

Similarly, relativistic effects can have a non-negligible effect in the secular rates of the argument of perihelion. These are usually measured in arcseconds per year or century, and typical values are 1-2 orders of magnitude smaller than the typical secular periods of the order of 100,000 years [Benitez and Gallardo, 2008]. Even if the secular rate has an error, the presence of encounters already causes the distributions to become uniform in argument of the node and perihelion after a few secular periods.

### 2.2.2 NEO close encounters in the inner Solar System

Flybys can occur with multiple planets over short periods of time. Even if the encounters are with the same planet, the closest approach distance and relative velocities can change depending on the timing of the flyby. The geometry of the flyby is constrained by the heliocentric elements of the asteroid. If shallow encounters are considered, the position in the asteroid orbit in which the planet is encountered can significantly change the relative velocity. These variations are not well captured by analytical theories, but the proposed propagation tool aims to accurately model these variations. These are different regimes of flybys in which the evaluation tool needs to be accurate.

In order to broadly show the diversity in flybys that different NEOs experience, we generate a list of flybys that will be used to validate the evaluation of close encounters. From the database of NEOs we select the ones with semi-major axis smaller than 2 au [JPL Solar System Dynamics and Center for NEO Studies (CNEOS), 2021]. Then, we propagate their positions using the secular model for 50 years. For such a brief period of time the change in the elements is insignificant for our purposes. Figure 2.2 shows more than 30,000 flybys generated with the described method, with the

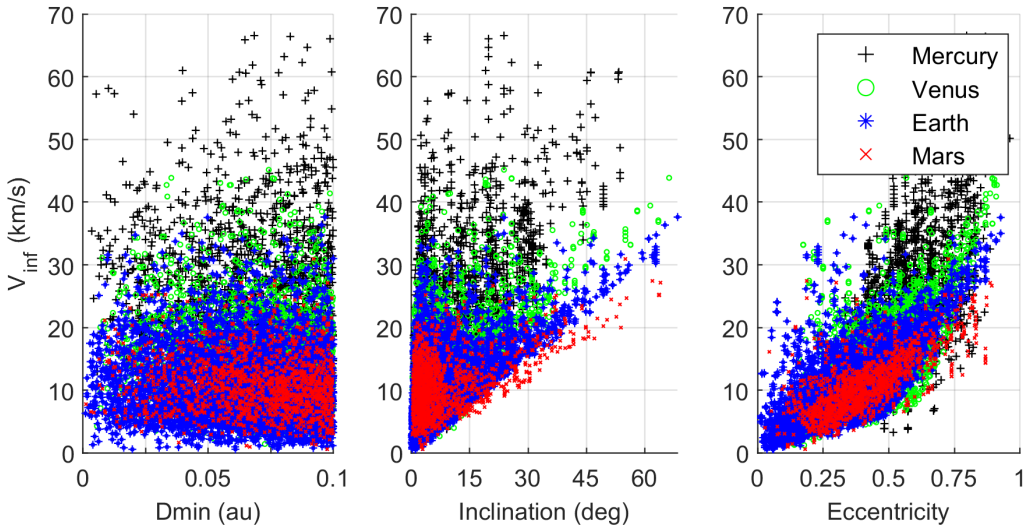


Figure 2.2 Relative velocity at closest approach of flybys generated from the propagation of NEOs.

symbols indicating the planet that the asteroid is encountering. The relative velocity is function of the closest approach distance (au), inclination (deg) and eccentricity. Shallow encounters are much more frequent than the very close encounters that cause large variations in orbit elements. Thus, we want to consider them even if their individual contribution is not as significant.

The range of possible relative velocities in figure 2.2 depends on the planet in question, with increasing maximum relative velocity for the planet closest to the Sun. The relative velocity is defined by the heliocentric orbit of the asteroid, with an increasing range of possible values depending on the inclination and eccentricity of the orbit. Overall, after millions of years asteroids experience a variety of encounters that can be computed with different methods. With this purpose the list of generated flybys is used to decide the method to compute the post-encounter elements of flybys. In section 2.3 we compute the error of different close encounter evaluation methods referenced to numerical integration of the trajectories.

## 2.3 Methodology

This semi-analytical propagation tool consists in the following process. First, the orbit of the asteroid is propagated by an analytical secular solution. This perturbed motion is interrupted when an encounter is found with a nearby planet. Then, the trajectory during the planetary encounter is modeled using a numerical method. Next, the secular propagation is continued until the subsequent encounter.

The simplest way to find encounters is to track the distance between the asteroid and planets at all times. While the regions in which encounters are possible are determined by the geometry of the asteroid around the central body, searching at all times is the most generic approach. The state of the planets is obtained from the secular solution of the 8 main planets interacting with each other. The state of the small body is corrected given the secular dynamics model. Once we determine the initial conditions of the encounter, the change in orbit elements is computed through the proposed numerical procedure.

There are many methods to compute planetary encounters available in the literature. Analytical solutions for Keplerian elements before and after close encounters in Öpik's Theory [Öpik, 1976] were extended for multiple applications by Valsecchi et al. [2003, 2015]. However, these analytical expressions are constrained to encounters that are very close and small bodies that are not co-moving with the planet. Asteroid and planet are co-moving when they have a small inclination and at least one of the node crossings close to the planet orbit.

We name shallow encounters those with large close approach distance but non-negligible effects. Shallow encounters are more frequent and influence the long-term evolution of small bodies in the Solar System. In order to account for shallow encounters, semi-analytical methodologies can be used to map before and after encounter conditions [Alessi and Sánchez, 2015]. These methods are based on the quadrature of Lagrange Planetary Equations around the encounter. In this work we derive a quadrature of Lagrange Planetary Equations in Delaunay elements which is solved using a numerical integration scheme. In the case of extremely close or slow encounters we solve

the planetary close encounters using numerical integration.

Once the solution of most encounters is obtained satisfactorily we focus efforts in the computation of the perturbed motion of the asteroid in absence of encounters. We evaluate the solution of N-bodies interacting secularly to generate the orbits of the planets. Then, we obtain the perturbed motion of the asteroid including only the planets relevant to its secular influence. Taking into account the influence of only Jupiter is a valid generic approach to estimate the secular dynamics of NEOs [Vokrouhlický et al., 2012, Pokorný and Vokrouhlický, 2013, Fuentes-Munoz and Scheeres, 2020a]. In this work we use the Laplace-Lagrange secular model. The secular rates as obtained by the analytical theory are compared to numerical integration to validate the range of validity of the solution. This defines a range of applicability of the tool, as we discuss later.

In this section we compare the individual pieces of the semi-analytical propagation tool to numerical methods. Last, we compare the combined semi-analytical propagation tool with trajectories obtained through numerical integration and evaluate the computational efficiency of the method.

### 2.3.1 Analytical secular dynamics of multibody systems

The dynamical landscape of the Solar System is complex with gravitational interactions between all planets. This landscape leads to resonances and secular motion in asteroids in the system. Well inside the inner Solar System, the dynamics are dominantly secular. The secular solution of a planetary system formed by N-planets can be obtained analytically to first order in inclinations and eccentricities and in the absence of resonances. This section derives an implementation of the solution following the procedure in Chapter 7 of Murray and Dermott [2000]. The perturbing potential is written for the $N$ bodies considered. Then Lagrange Planetary Equations are used to compute the equations of motion of the elements of each particle, leading to a system of differential equations solved simultaneously.

The secular model is obtained as follows: (1) The perturbing potential is split in a direct part and an indirect part based on the dependency on fast angles, (2) then the perturbing potential is expanded in Keplerian Elements. (3) The important terms of the expansion are selected based on the averaging principle. (4) The terms are rewritten in semi-equinoctial elements to ease the solution of the global system of equations. (5) Take the necessary partials to solve the set of Lagrange Planetary Equations. The perturbing potential experienced by a mass $j$ by a second mass $k$ is:

$$R_{jk} = \frac{Gm_k}{a_k}\left(R_{jk_D} + R_{jk_I}\right) \tag{2.1}$$

Where $a_k$ is the semi-major axis of body the external body. The perturbing potential is separated in the direct $R_{jk_D}$ and indirect $R_{jk_I}$ parts:

$$R_{jk_D} = \frac{a_k}{|r_j - r_k|} \qquad R_{jk_I} = -\frac{a_k^2}{a_j}\frac{r_j \cdot r_k}{|r_k|^3} \tag{2.2}$$

The separation is convenient to expand in the ratio of semi-major axes $\alpha_{jk}$ as well as sines and cosines of $\{\varpi_j, \Omega_j, \lambda_j, \varpi_k, \Omega_k, \lambda_k, \}$. The ratio of semi-major axes is $\alpha_{jk} = a_j/a_k$ if the perturber is external, or $\alpha_{jk} = a_j/a_k$ if the perturber is internal. All the terms that depend on the longitudes $\{\lambda, \lambda_j\}$ are of short-period, so it can be argued that they do not contribute to the averaged potential $R_j$. The secular potential lowest order in eccentricities and inclinations is:

$$R_j = R_{0,j} + R_{1,j} = \sum_{k=1,k\neq j}^{N} Gm_k \frac{1}{2a_k} b_{1/2}^{(0)}\left(\alpha_{jk}\right) + R_{1,j} \tag{2.3}$$

$$R_{1,j} = n_j a_j^2 \left[\frac{1}{2}A_{jj}e_j^2 + \frac{1}{2}B_{jj}I_j^2 + \sum_{\substack{k=1\\k\neq j}}^{N} A_{jk}e_j e_k \cos\left(\varpi_j - \varpi_k\right) + B_{jk}I_j I_k \cos\left(\Omega_j - \Omega_k\right)\right] \tag{2.4}$$

Where $\bar{\alpha}_{jk} = a_j/a_k$ if the perturber is external, or $\bar{\alpha}_{jk} = 1$ if the perturber is internal. The coefficients $A_{jj}, A_{jk}, B_{jj}, B_{jk}$ are:

$$A_{jk} = -n_j \frac{1}{4} \frac{m_k}{m_c + m_j} \alpha_{jk} \bar{\alpha}_{jk} b^{(2)}_{3/2}(\alpha_{jk}) \tag{2.5}$$

$$B_{jk} = +n_j \frac{1}{4} \frac{m_k}{m_c + m_j} \alpha_{jk} \bar{\alpha}_{jk} b^{(1)}_{3/2}(\alpha_{jk}) \tag{2.6}$$

$$A_{jj} = +n_j \frac{1}{4} \sum_{k=1,k\neq j}^{N} \frac{m_k}{m_c + m_j} \alpha_{jk} \bar{\alpha}_{jk} b^{(1)}_{3/2}(\alpha_{jk}) = \sum_{k=1,k\neq j}^{N} B_{jk} \tag{2.7}$$

$$B_{jj} = -n_j \frac{1}{4} \sum_{k=1,k\neq j}^{N} \frac{m_k}{m_c + m_j} \alpha_{jk} \bar{\alpha}_{jk} b^{(1)}_{3/2}(\alpha_{jk}) = -\sum_{k=1,k\neq j}^{N} B_{jk} \tag{2.8}$$

where the coefficients $b^{(k)}_s$ are Laplace Coefficients. More details on their computation can be found in Appendix A. The coefficients $A_{jj}, A_{jk}, B_{jj}, B_{jk}$ form the matrices $A$ and $B$. We can rewrite the potential in semi-equinoctial elements,

$$\begin{aligned} h_j &= e_j \sin \varpi_j & p_j &= I_j \sin \Omega_j \\ k_j &= e_j \cos \varpi_j & q_j &= I_j \sin \Omega_j \end{aligned} \tag{2.9}$$

the potential becomes:

$$R_{1,j} = n_j a_j^2 \left[ \frac{1}{2} A_{jj}(h_j^2 + k_j^2) + \frac{1}{2} B_{jj}(p_j^2 + q_j^2) + \sum_{k=1,k\neq j}^{N} A_{jk}(h_j h_k + k_j k_k) + B_{jk}(p_j p_k + q_j q_k) \right] \tag{2.10}$$

Our complete set of states includes the mean anomaly at epoch $\sigma_j$ and $L_j = \sqrt{GMa_j}$. The equations of motion become:

$$\begin{aligned} \dot{p}_j &= \frac{1}{n_j a_j^2} \frac{\partial R_j}{\partial q_j} & \dot{h}_j &= \frac{1}{n_j a_j^2} \frac{\partial R_j}{\partial k_j} & \dot{L}_j &= \frac{\partial R_j}{\partial \sigma_j} \\ \dot{q}_j &= -\frac{1}{n_j a_j^2} \frac{\partial R_j}{\partial p_j} & \dot{k}_j &= -\frac{1}{n_j a_j^2} \frac{\partial R_j}{\partial h_j} & \dot{\sigma}_j &= -\frac{\partial R_j}{\partial L_j} \end{aligned} \tag{2.11}$$

The solution of $h_j, k_j, p_j, q_j$ only depends on $R_{1,j}$. For this reason the perturbing potential is often only expressed with those components. However, if we want the solution of the mean anomaly at epoch $\sigma_j$ it is necessary to take into account $R_{0,j}$. In the process of averaging the terms that

would effect the semi-major axis are removed, meaning that under this assumption that element remains constant. The solution of $h_j, k_j, p_j, q_j$ is:

$$\begin{aligned} h_j(t) &= \sum_{i=1}^{N} e_{ji} \sin(g_i t + \beta_i) & p_j(t) &= \sum_{i=1}^{N} I_{ji} \sin(f_i t + \gamma_i) \\ k_j(t) &= \sum_{i=1}^{N} e_{ji} \cos(g_i t + \beta_i) & q_j(t) &= \sum_{i=1}^{N} I_{ji} \cos(f_i t + \gamma_i) \end{aligned} \tag{2.12}$$

where two sets of eigenvalue problems are solved for $e_{ji}, I_{ji}, f_i, g_i$. The frequencies $g_i$ are the eigenvalues of $A$, and the frequencies $f_i$ are the eigenvalues of $B$. $e_{ji}$ and $I_{ji}$ are related to the eigenvectors of $A$ and $B$, but need to be solved with $\beta_i, \gamma_i$ given a set of initial conditions. In order to solve for $e_{ji}, I_{ji}, \beta_i, \gamma_i$ we proceed as follows. From the matrices of normalized eigenvectors $\bar{e}_{ji}, \bar{I}_{ji}$ and the initial conditions $h, k, p, q$ we form:

$$\begin{aligned} h &= \bar{e}_{ji} [S_i \sin \beta_i] & p &= \bar{I}_{ji} [T_i \sin \gamma_i] \\ k &= \bar{e}_{ji} [S_i \cos \beta_i] & q &= \bar{I}_{ji} [T_i \cos \gamma_i] \end{aligned} \tag{2.13}$$

These are four linear systems of equations, where $S_i, T_i$ are the scaling factors of each eigenvector. Solving for the combined factors $[S_i \sin \beta_i], [S_i \cos \beta_i], [T_i \sin \gamma_i]$ and $[T_i \cos \gamma_i]$ we can reconstruct the vectors $e_{ji}, I_{ji}$ and the phase angles $\beta_i, \gamma_i$.

Table 2.1 Initial conditions of the Solar System propagation in Figure 2.3, obtained from ephemeris DE431 at Epoch: $\text{JD}_0 = 2455562.5$ (2011 January 1) TDB

| Planet | $a$ (au) | $e$ | $i$ (deg) | $\Omega$ (deg) | $\omega$ (deg) | $M_0$ (deg) |
|---|---|---|---|---|---|---|
| Mercury | 0.39703 | 0.21337 | 6.936 | 48.264 | 31.991 | 52.745 |
| Venus | 0.73096 | 0.012687 | 3.378 | 76.799 | 45.020 | 16.566 |
| Earth | 1.0030 | 0.018402 | 0.001 | 154.979 | 296.322 | 8.654 |
| Mars | 1.5177 | 0.093083 | 1.852 | 49.461 | 288.507 | 322.879 |
| Jupiter | 5.1904 | 0.047388 | 1.305 | 100.514 | 273.897 | 353.761 |
| Saturn | 9.5499 | 0.05412 | 2.487 | 113.612 | 339.598 | 91.261 |
| Uranus | 19.207 | 0.04628 | 0.772 | 73.997 | 96.864 | 189.506 |
| Neptune | 30.109 | 0.0091006 | 1.770 | 131.780 | 265.440 | 291.693 |

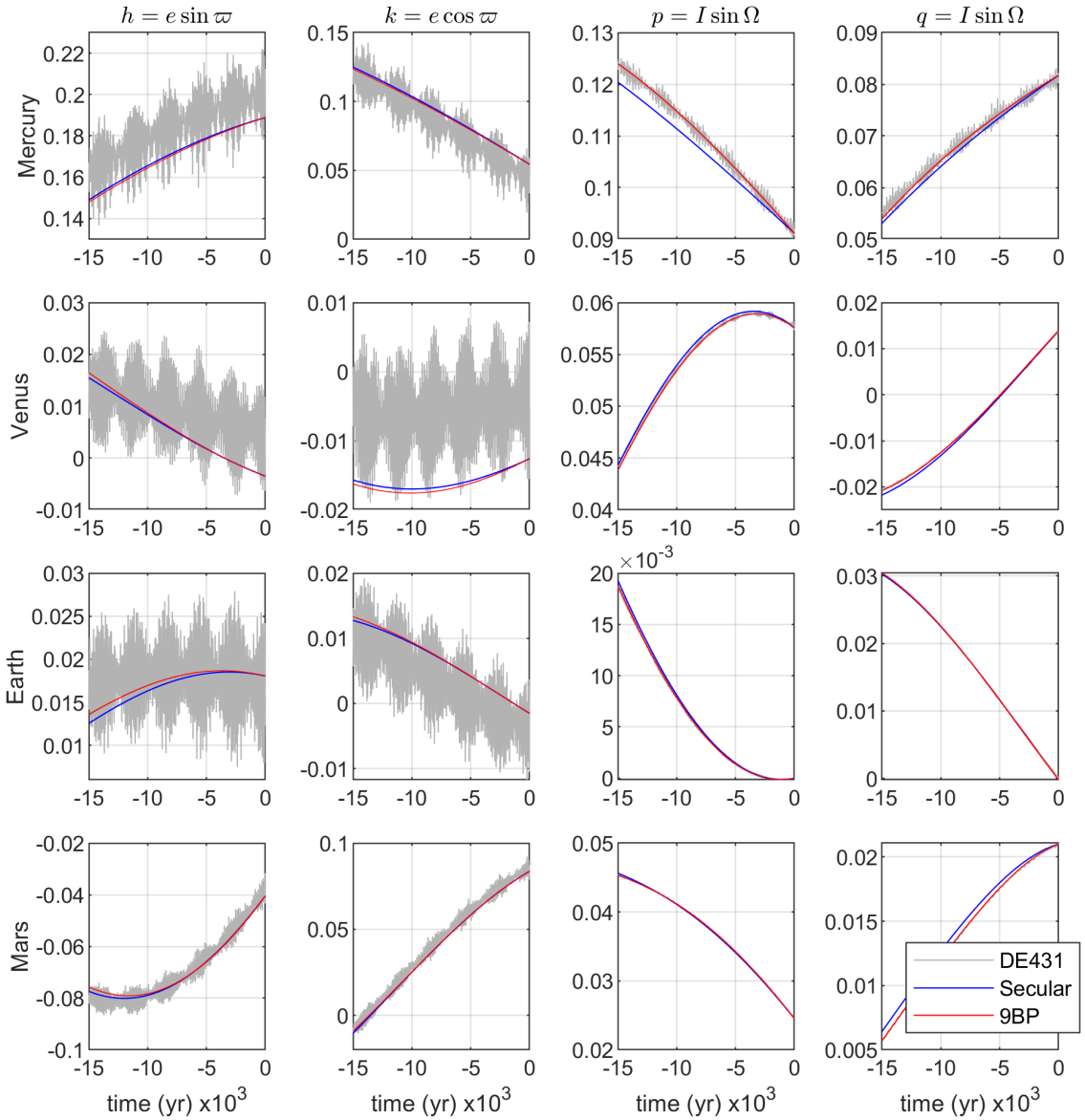


Figure 2.3 Semi-equinoctial elements of the inner Solar System planets obtained using three models.

Figure 2.3 shows the solution of eq. 2.12 for Mercury, Venus, Earth and Mars as perturbed mutually and from the rest of planets of the Solar System. This model is compared to two other models for 15,000 years into the past. The first one is a numerical integration of the N-body problem taking into account the main 8 planets of the Solar System and the Sun. Then, we also compare to the planetary ephemerides DE431 [Folkner et al., 2014]. While the complete ephemerides models show the short period effects, the secular component is modeled by the two simplified models.

The initial conditions of the 9BP integration and the secular theory are obtained by averaging the full ephemeris model for two orbit periods. As a result, the initial conditions visually appear to be off from the mean of the full ephemeris solution, but they are the actual time average.

The short-term components have a significant effect in the evolution of $h_j, k_j$. In the case of $p_j, q_j$, the secular component is the dominant effect of the evolution. Because of the assumptions of small eccentricities and inclinations, the predicted frequencies are not perfectly accurate, as observed in the drift between the 9BP solution and the analytical theory of figure 2.3, especially in $p_j, q_j$.

A similar agreement in these elements is found for the gas giants. However, only the inner Solar System planets are shown as they are the bodies that are encountered by near-Earth objects. Thus, these are the planets for which we want to guarantee an accurate model of their secular dynamics. The analytical propagation of Mercury drifts the most from the full ephemeris solution, although it is the least relevant inner planet. Close encounters with Mercury are unfrequent and have a small effect, as Mercury is the least massive planet and it is encountered with very high relative velocity.

As a result of the averaging of the perturbing potential, the semi-major axis of the bodies remains constant. The complete set of secular solutions includes the mean anomaly at epoch $\sigma_j$. Short term applications benefit from the improved characterization of the position of the bodies in their orbits. Solving for $\sigma_j$ is straightforward if we ignore the contribution of $R_{1,j}$, which has a small effect compared to $R_{0,j}$. The equation of motion for $\sigma_j$ becomes:

$$\dot{\sigma}_j = -\frac{\partial R_j}{\partial L_j} = -\frac{2}{n_j a_j}\frac{\partial R_{0,j}}{\partial a_j} \tag{2.14}$$

and the solution depends on whether the perturber is external or internal:

$$\dot{\sigma}_j = -\sum_{k=1,k\neq j}^{N} \frac{Gm_k}{n_j a_j^2}\bar{c}_{jk} Db_{1/2}^{(0)} \tag{2.15}$$

where $\bar{c}_{jk} = a_j/a_k^2$ in the case of an external perturber and $\bar{c}_{jk} = -1/a_j$ if the perturber is internal.

The solution of the equation is simply a constant drift given by the rate $\dot{\sigma}$. This element completes the set of elements of the secular model.

### 2.3.2 Analytical secular dynamics of near-Earth asteroids

The secular dynamics of asteroids can be modelled as a particular case of the secular dynamics of multibody systems described above. In the present work we apply this solution to the evolution of the asteroid under the external perturbation of Jupiter. The solutions of equation 2.13 simplify in the case of a system of 2 bodies with a massless internal body. We follow the same process to obtain the solution. Matrices $A_{jk}$ and $B_{jk}$ simplify to:

$$A_{jk} = \begin{pmatrix} B_{12} & A_{12} \\ 0 & 0 \end{pmatrix} \qquad B_{jk} = \begin{pmatrix} -B_{12} & B_{12} \\ 0 & 0 \end{pmatrix} \tag{2.16}$$

where the subindexes $1, 2$ correspond respectively to the massless particle and the external perturber. The coefficients of the matrices are found as in equations 2.5-2.8 above. The solution to the eigenvalue problem yields the secular frequencies of the secular propagation $g_1 = B_{12}$, $g_2 = 0$, $f_1 = -B_{12}$, $f_2 = 0$. As expected, the elements of the perturber $h_2, k_2, p_2, k_2$ remain constant. The eigenvectors are the columns of the matrices:

$$\bar{e}_{jk} = \begin{pmatrix} 1 & \kappa \\ 0 & 1 \end{pmatrix} \qquad \bar{i}_{jk} \begin{pmatrix} 1 & \frac{\sqrt{2}}{2} \\ 0 & \frac{\sqrt{2}}{2} \end{pmatrix} \tag{2.17}$$

where the constant $\kappa$ is found as the ratio between Laplace coefficients:

$$\kappa = \frac{A_{12}}{-B_{12}} = \frac{b_{3/2}^{(2)}}{b_{3/2}^{(1)}} \tag{2.18}$$

Note that the vector $(e_{12}, e_{22})$ is not normalized. This is not necessary because in the process of obtaining the integration constants from the initial conditions the scaling of the eigenvectors is found. The solution of the elements of the massless particle becomes:

$$\begin{aligned} h_1(t) &= S_1 \sin(g_1 t + \beta_1) + \kappa h_2 & p_1(t) &= T_1 \sin(f_1 t + \gamma_1) + p_2 \\ k_1(t) &= S_1 \cos(g_1 t + \beta_1) + \kappa k_2 & q_1(t) &= T_1 \cos(f_1 t + \gamma_1) + q_2 \end{aligned} \tag{2.19}$$

with constants of integration:

$$\begin{aligned} S_1^2 &= e_{1,0}^2 + \kappa^2 e_2^2 - 2\kappa e_{1,0} e_2 \cos(\varpi_{1,0} - \varpi_2) & \tan\beta_1 &= \frac{h_{1,0} - \kappa h_2}{k_{1,0} - \kappa k_2} \\ T_1^2 &= i_{1,0}^2 + i_2^2 - 2 i_{1,0} i_2 \cos(\Omega_{1,0} - \Omega_2) & \tan\gamma_1 &= \frac{p_{1,0} - p_2}{q_{1,0} - q_2} \end{aligned} \tag{2.20}$$

The time evolution of the Keplerian elements set can be obtained from the relationships with the semi-equinoctial set in equation 2.9. The solutions of $\varpi(t), \Omega(t)$ are the secular drift with frequencies $g_1, f_1$ that are equal with opposite signs. The solutions of $e(t), i(t)$ are oscillations with frequencies $g_1, f_1$ as obtained from the development of eccentricity $e_1(t) = \sqrt{h_1^2(t) + k_1^2(t)}$ and inclination $i_1(t) = \sqrt{p_1^2(t) + q_1^2(t)}$. The maximum and minimum values of eccentricity and inclination are:

$$\begin{aligned} e_{1,min}^2 &= S_1^2 + \kappa^2 e_2^2 - 2 S_1 \kappa e_2 & i_{1,min}^2 &= T_1^2 + i_2^2 - 2 T_1 i_2 \\ e_{1,max}^2 &= S_1^2 + \kappa^2 e_2^2 + 2 S_1 \kappa e_2 & i_{1,max}^2 &= T_1^2 + i_2^2 - 2 T_1 i_2 \end{aligned} \tag{2.21}$$

The secular model is computed for the fictitious asteroid of Case 1 of table B.1 with the perturbation of Jupiter given by the elements of table 2.1. These cases are used later to demonstrate the propagation tool. For a nominal eccentricity of 0.15 the minimum eccentricity is 0.14946 and maximum is 0.17466. For a nominal inclination of 10 degrees, the minimum inclination is 7.41823 degrees and maximum is 10.02508 degrees. The characteristic period of the secular motion $T_{sec}$ is 154,116 years.

This model assumes small eccentricities and inclinations. While these conditions are usually not fulfilled, it is important to remark that eccentricity and inclination are under frequent disturbance due to close encounters. Most importantly, the secular drift in $\Omega, \omega$ controls the evolution of the possible planetary encounters.

The assumptions on the heliocentric orbit of the asteroid for the analytical secular perturbation solution are not always fulfilled among the NEO population. In this section we show that the analytical theory represents the dynamics of the perturbation by Jupiter. For this reason, we integrated the orbits of 4462 NEOs with $e < 0.7$ and $i < 0.5$ rad for 50,000 years. Note that in the solution of equation 2.19 if the terms of the external perturber are small the solution tends to a linear drift of the angles $\Omega, \varpi$. In addition, given the relationship between the frequencies $g$ and $f$, the relationship between the arguments rates is $\dot{\omega} = -2\dot{\Omega}$.

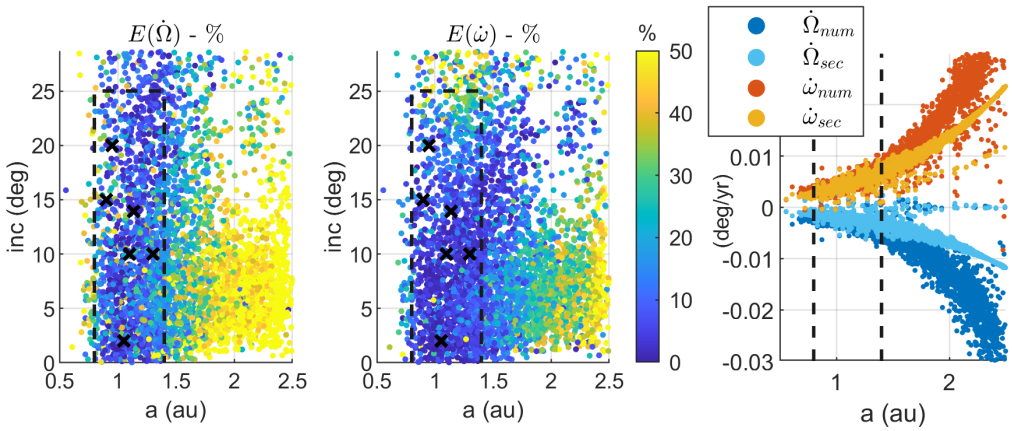


Figure 2.4 Error in the secular rates of near-Earth objects.

Figure 2.4 shows the secular rates computed from linear regression of the time histories of $\Omega$,$\omega$ using the Laplace-Lagrange secular theory and compared to numerical integration of the three-body problem in percent. The secular rates in ascending node (left) and argument of perihelion (center) are shown as function of the initial conditions semi-major axis and inclination. The secular rates are shown function of the initial semi-major axis (right) for the two methods. The dashed lines indicate the region in which we compute the average errors. This region includes the initial conditions used throughout the chapter, indicated as cross marks.

Note that from an initially larger list of NEOs, a significant fraction (12%) was discarded because either eccentricity or inclination were larger than 0.5. An additional 11% of the solutions were discarded because the error in the regression was too large or during the propagation close encounters with Jupiter moved the orbit of the NEO to a completely different location than the

initial conditions. While the linear regression secular rates are not equivalent to the frequencies of the analytical solution, they serve as a comparison between the two dynamical models. The error is computed in percent relative to the rate measured from the regression of the numerically integrated trajectories, given by:

$$E(\dot{\omega}) = 100 \left| \frac{\dot{\omega}_{sec} - \dot{\omega}_{3BP}}{\dot{\omega}_{3BP}} \right| \tag{2.22}$$

As observed in Figure 2.4 the rates obtained with the two methods agree towards the smaller end of semi-major axis. Since these are near-Earth objects, the condition of being in the vicinity of Earth means that eccentricity increases with semi-major axis. We can see that past 1.5-2 au the difference between the two models is increased, as well as the secular rates values themselves also increase. This difference is also appreciated in the rates as function of semi-major axis, in which we show the agreement in the NEO region. Using the current model we find secular rates for 60% of the population with an error less than 30% in both $\dot{\omega}$ and $\dot{\varpi}$. If we limit the application of the secular theory to semi-major axes between 0.8-1.4 au (dashed region in Figure 2.4) we find that this agreement improves to 88%. It is important to note that the examples chosen to demonstrate the semi-analytical propagation tool fall within this region. Outside of this region we can verify if the secular rates found are reliable by using numerical integration. This test integration must be long enough to observe the secular rates, but still orders of magnitude shorter than the time-scales that we can more efficiently study using the semi-analytical propagation.

At larger semi-major axes the effect of mean-motion resonances becomes important, and that Lidov-Kozai dynamics may better represent the dynamics for large eccentricities and inclinations [Michel et al., 1996b, Morbidelli et al., 2009]. The implementation of additional analytical long-term dynamics models to model any generic asteroid is left as future work.

### 2.3.3 Finding the subsequent encounter

The analytical propagation of particles is interrupted when an encounter with a planet is detected. In principle it is not necessary to track the distance to planets at all times, since the regions in which encounters are possible are determined by the geometry of the asteroid around the central body. If the inclination relative to the planet is high, then the encounters are only possible in the vicinity of the ascending and descending node. However, the most generic approach is to track the distance between the asteroid and the crossing planets at all times. Thus, the results in this work follow the latter approach to find encounters within a closest approach distance of 0.1 au. When the two bodies are close, the unperturbed closest approach distance is found using a bisection method where the function is the derivative of the distance as obtained by finite differences. This process results in less evaluations of the relative distance function based on the heliocentric elements of the bodies.

The elements of the planets and the asteroid are propagated using the secular solution at the date of start of the encounter, which is defined below. The transition between models consists in the conversion between the sets of elements, obtaining the necessary Keplerian elements in the process. These are semi-equinoctial elements for the analytical perturbed propagation as in equation 2.9 and Delaunay elements for the quadrature of the Lagrange planetary equations.

### 2.3.4 Evaluation of planetary encounters

Close encounters are commonly solved using the analytical Öpik theory [Öpik, 1976]. While this theory requires the least computational resources, its accuracy is limited to specific circumstances. The quadrature of Lagrange Planetary Equations can be used to solve close encounters [Alessi and Sánchez, 2015]. In this work we derive a solution using this method for generic close encounters using Delaunay elements. The two methods are compared to the integration of the three body problem from the same date and during the same period of time.

**Öpik theory of close encounters**

An analytical solution to the planetary close encounter problem was derived by Öpik [Öpik, 1976]. This solution was extended and studied in detail by Valsecchi et al. [2003, 2015]. The encounter solution uses a linearized mapping from orbital elements to a planetocentric Cartesian frame, that is later expressed in B-plane coordinates. Then, the encounter is assumed instantaneous and the incoming asymptote and B-plane both rotate. The new B-plane coordinates are mapped back to the orbit elements space.

The analytical solution is derived for a hyperbolic flyby around a point secondary mass. This mapping between B-plane coordinates and orbit elements is linearized in the impact parameter. Thus, the encounter must be close for the method to be reliable. Additionally, if the inclination is small the relative velocity coordinates become undefined. A possible way to avoid this is by using a method sometimes referred as pseudo-Öpik [Greenberg et al., 1988]. In this case the relative velocity vector is computed directly and defines the turn angle $\gamma$ at the time of closest approach:

$$\tan\frac{\gamma}{2} = \frac{m}{bU^2} \tag{2.23}$$

where $m$ is the mass of the planet in units of the mass of the Sun, $b$ is the impact parameter and $U^2$ is the relative velocity in units of the circular velocity of the planet. Here we use the unperturbed trajectory of the planet and asteroid to find these quantities. That is, the impact parameter and relative velocity are found as the planetocentric distance and velocity at closest approach.

In Chapter 6 we propose an extension of Öpik theory to account for the variation of the MOID between encounters in the computation of keyholes. Thus, we provide more details of the analytical solution of planetary close encounters.

**Lagrange Planetary Equations**

The proposed computation of the encounter effect is computed as follows. The variation in elements over the encounter event is obtained from a quadrature of the Lagrange Planetary Equations assuming the geometry of the unperturbed flyby. The elements used are obtained from

the secular propagation of the asteroid. The Lagrange Planetary Equations describe the evolution of orbit elements due to a perturbing potential. The derivation of Lagrange Planetary Equations can be found in some references for different sets of orbit elements [Brouwer and Clemence, 1961, Roy, 2004]. In general, they have the form of:

$$\dot{\boldsymbol{D}} = [L(\boldsymbol{D})] \frac{\partial R}{\partial \boldsymbol{D}}(\boldsymbol{D}, t) \tag{2.24}$$

where $\boldsymbol{D}$ is the set of elements of choice and $L(\boldsymbol{D})$ is a function of the elements that depends on the chosen elements. In this case the perturbing potential $R$ is the gravitational potential of the encountered planet. Note that without further simplifying assumptions the partials of the perturbing potential are function of the elements and function of time. For the elements of choice we take the partial derivatives that relate the set of elements to Keplerian elements $\boldsymbol{K} = [a, e, i, \Omega, \omega, \sigma]$ and Cartesian coordinates. From the orbital elements representations available to choose, the current implementation uses the Delaunay elements:

$$\begin{aligned} L &= \sqrt{\mu a} & l &= \sigma \\ G &= L\sqrt{1-e^2} & g &= \omega \\ H &= G\cos i & h &= \Omega \end{aligned} \tag{2.25}$$

The Lagrange Planetary Equations with the perturbing potential of Equation 2.1 with $j$ being the asteroid and $k$ the encountered planet can be written as:

$$\begin{aligned} \frac{\mathrm{d}L}{\mathrm{d}t} &= \frac{\partial R}{\partial r}\frac{\partial r}{\partial \boldsymbol{K}}\frac{\partial \boldsymbol{K}}{\partial l} & \frac{\mathrm{d}l}{\mathrm{d}t} &= -\frac{\partial R}{\partial r}\frac{\partial r}{\partial \boldsymbol{K}}\frac{\partial \boldsymbol{K}}{\partial L} \\ \frac{\mathrm{d}G}{\mathrm{d}t} &= \frac{\partial R}{\partial r}\frac{\partial r}{\partial \boldsymbol{K}}\frac{\partial \boldsymbol{K}}{\partial g} & \frac{\mathrm{d}g}{\mathrm{d}t} &= -\frac{\partial R}{\partial r}\frac{\partial r}{\partial \boldsymbol{K}}\frac{\partial \boldsymbol{K}}{\partial G} \\ \frac{\mathrm{d}H}{\mathrm{d}t} &= \frac{\partial R}{\partial r}\frac{\partial r}{\partial \boldsymbol{K}}\frac{\partial \boldsymbol{K}}{\partial h} & \frac{\mathrm{d}h}{\mathrm{d}t} &= -\frac{\partial R}{\partial r}\frac{\partial r}{\partial \boldsymbol{K}}\frac{\partial \boldsymbol{K}}{\partial H} \end{aligned} \tag{2.26}$$

The proposed solution is the integration of these differential equations around the encounter date $t_e$ and assuming the unperturbed geometry of the flyby. Hence, the asteroid coordinates are obtained from the heliocentric elements secularly propagated until the start of integration date $D_0$ and the quadrature is only a function of time:

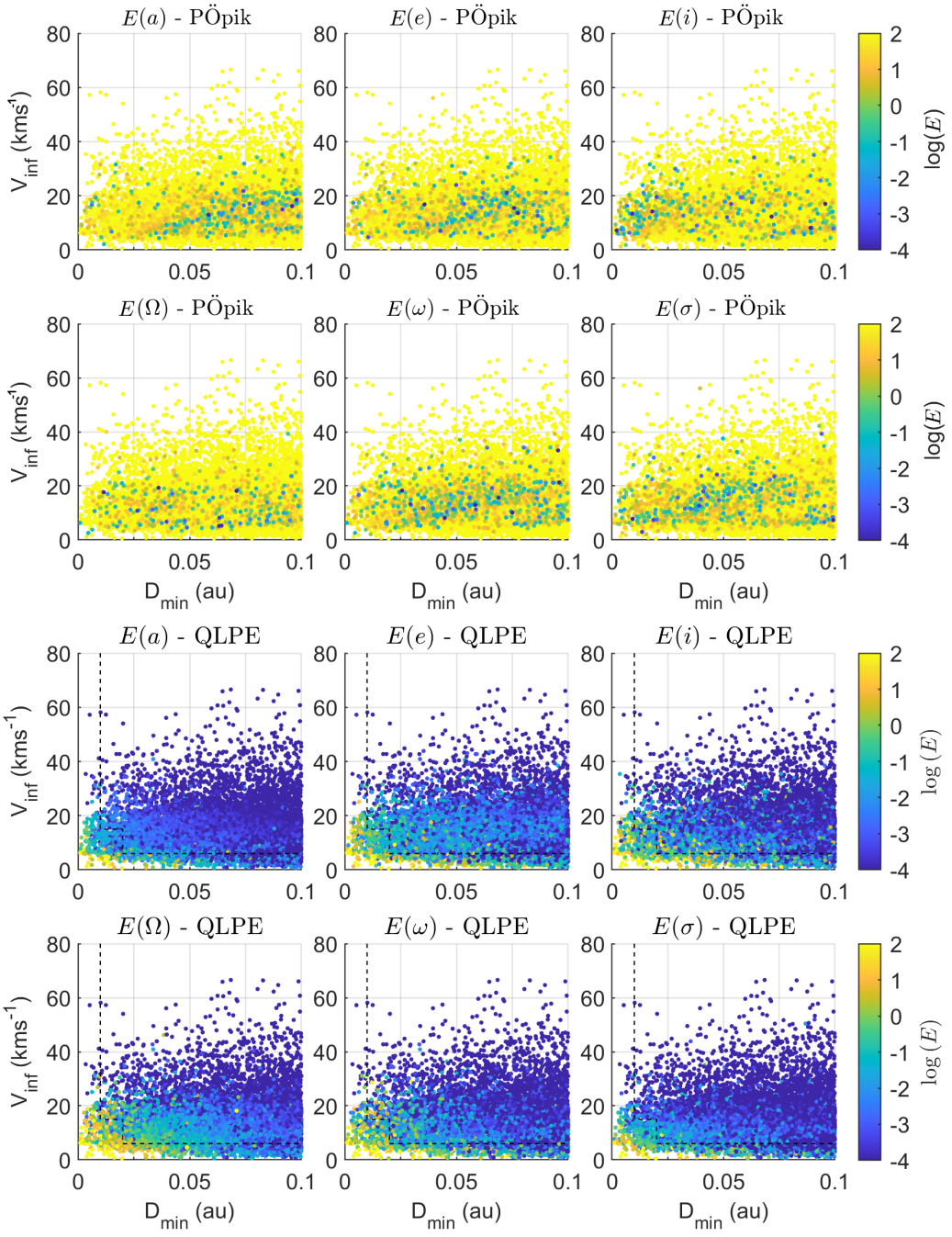


Figure 2.5 Logarithm of the errors in the computation of the final Keplerian elements during close encounters given by pseudo-Öpik theory (PÖpik) and the quadrature of LPE (QLPEs)

$$\Delta \boldsymbol{D} = \int_{t_e-\delta t}^{t_e+\delta t} \dot{\boldsymbol{D}}(\boldsymbol{D}_0, t)dt \tag{2.27}$$

The integration is conducted for a fraction of the orbit period around the closest approach distance. This fraction is a constant set large enough such that the effect of the encounter is captured completely. In this work we use a self-coded fast quadrature function based on the midpoint rule and a total integration time of 20% of the orbital period. This method avoids the frame transformation to the center of the planet, since it considers the planet as an external perturber of the asteroid motion around the Sun. For this reason, it is not possible to obtain a closed form solution of the integral. Nonetheless, this approach does not imply further assumptions that limit its range of applicability. Future work will be done in finding the optimal set for this application. This approach is accurate for the vast majority of encounters, but it is less accurate for the closest ones, as we explore in the following section.

Using the list of flybys generated in figure 2.2 we computed the errors of Öpik theory and the quadrature of LPE compared to the solution of the encounter using the three-body problem. The error $E(K)$ is relative to the variation and in percent, given by:

$$E(K) = 100\frac{\Delta K_{QLPE} - \Delta K_{3BP}}{\Delta K_{3BP}} \tag{2.28}$$

The results of this evaluation are described in figure 2.5. The list of flybys used is shown in figure 2.2 and generated as previously described. The flybys are represented in the plane of relative velocity at closest approach $V_{inf}$ (km $s^{-1}$) and distance of closest approach (au).

Using pseudo-Öpik theory there is a region in the space of relative velocity and closest approach distance in which flybys can be computed accurately. However, this region is not constant for all Keplerian elements. In addition, most flybys in our range of interest are not computed correctly using this method. Slow flybys break the assumption in Öpik theory that the behavior during the flyby is modeled by the two-body hyperbolic interaction. Many of the faster flybys occur with Venus and Mercury. The two-body hyperbolic flyby model fails to characterize the effect of

flybys with Mercury even if the planetary close encounters are faster.

Using the quadrature of the Lagrange Planetary Equations 99% of the flybys list are computed with less than 3% of error, and more than 88% with less than 0.1% error. The flybys that are not computed accurately with this method are very close and with a slow relative velocity. These flybys can break the assumption of the unperturbed geometry of the flyby. Given that these encounters also cause significant variations in the elements, these infrequent encounters are solved using a three-body problem integration in Cartesian coordinates. The criteria to solve these encounters using the alternative method is by defining three threshold regions in the encounter parameters: with very small $V_\infty$, very small closest approach distance, and a combination of both close to zero. This process simplifies the detection of collisions with the planets during the numerical integration in Cartesian space in the heliocentric frame.

### 2.3.5 Semi-analytical propagation vs. numerical integration

In the previous sections we validated the individual pieces of the semi-analytical propagation tool. Once combined, we want to compare the resulting trajectories to trajectories obtained using numerical integration. With this purpose we generate a fictitious NEO population and propagate their orbits using both methods.

The fictitious NEO population we define consists in normal distributions for the perihelion distance, eccentricity, inclination. The distributions are centered respectively around 0.8 au, $0.2, 10$ deg and with standard deviations of 0.05 au, $0.05, 3$ deg. Arguments of the node, perihelion and initial mean anomalies are defined as uniform distributions in the $[0, 360]$ degrees range. We sample 1000 particles from these distributions as our test set for the comparison between the two methodologies. We setup the numerical integration of the asteroid orbits considering the planets as third body perturbers. The model we use for the orbits of the planets is the secular theory developed in section 2.3.1.

Figure 2.6 shows the results of the propagation for 200,000 years using both methods as well as the distributions that defined the initial conditions. The analytical probability density function of the initial conditions is shown as a continuous red line. In addition, the mean number of encounters found is shown as function of the closest approach distance for both methods.

We find that the cumulative distribution of the mean number of encounters versus closest approach distance is matched very closely. After 200,000 years, the presence of planetary encounters causes a dispersion of the initial distributions. The distribution obtained through semi-analytical propagation is able to track this drift.

The main difference between the results using the two methods is that the numerically integrated distribution shows a small drift in the center of the distribution, but very similar dispersions. In terms of the longitude of the perihelion, the resulting distributions after 200,000 years remain uniform using either of the two propagation methods. The other significant difference between the two methods is in the required the computational time, which is discussed next.

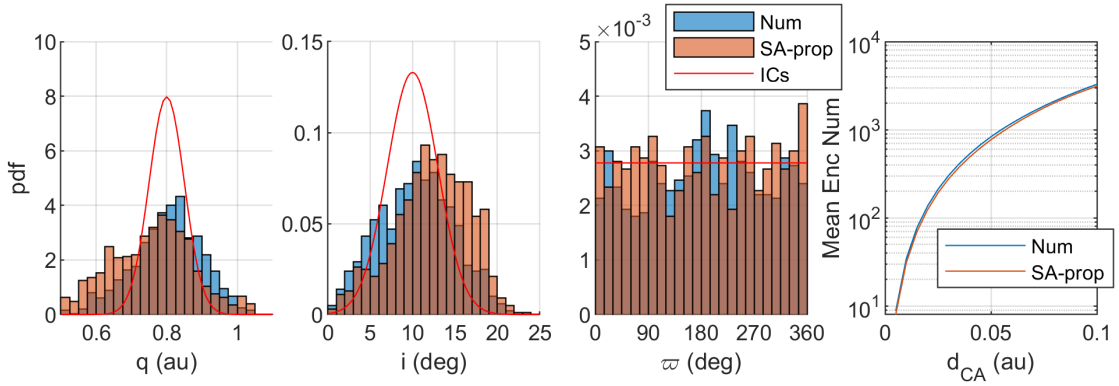


Figure 2.6 Comparison between the 1000 trajectories obtained using numerical integration and semi-analytical propagation.

### 2.3.6 Computational time of the semi-analytical propagation tool

The semi-analytical propagation of near-Earth asteroids reduces the computational time required to obtain long-term trajectories. The use of numerical techniques is limited almost exclusively to the computation of planetary encounters, a small fraction of the simulated time.

In order to estimate the speedup of the propagation we generate a fictitious population of NEOs and propagate them for 100,000 years with the semi-analytical propagation tool and with numerical integration. The semi-analytical propagation tool uses the secular solution of the Solar System to compute the orbits of the planets over long periods of time. Then, planetary encounters can occur with any planet. The secular propagation of the asteroid is derived as described in the text accounting only for Jupiter, which accurately represents the asteroid motion in the absence of resonances. The semi-analytical propagation of 100,000 years with this setup is computed in around 5 seconds. In order to account for these effects in numerical integrations we use the N-Body problem integrator IAS15 [Rein and Spiegel, 2014] with all the planets and the asteroid.

The simulation is set up using high-level programming code that runs libraries in more efficient low-level code. This is the case for both numerical integrations and semi-analytical propagation, running in the same 2.5GHz Intel Core i7 processor. The result is a speed-up of x500-x1000 of the semi-analytical propagation tool as compared to the numerical integration. The current implementation allows room for significant speed-up that is left for future work. The perturbed long-term propagation could be extended to use other suitable models of interest. The computational cost is not expected to increase while we use analytical solutions of these long-term perturbations.

## 2.4 Semi-analytical propagation results

In this section we demonstrate the semi-analytical propagation tool in a variety of scenarios. First, we want to compare the semi-analytical model with trajectories obtained through numerical integration. Matching very accurately trajectories obtained with more complex models is outside the scope of the comparison. Even if the models were identical, trajectories under encounters are very sensitive to the initial conditions and under small perturbations they diverge into different paths. This effect was visualized in figure 2.1 using only numerical integration. For this reason, long term simulations may focus on the statistical analysis of the dynamical evolution rather than individual trajectories. Throughout the section, the simulations include Jupiter as the only planet secularly perturbing the asteroids. All the inner Solar System bodies are considered to evaluate

planetary encounters. These are secularly evolving due to mutual perturbations and the perturbations of the outer Solar System planets, as described in section 3.a..

### 2.4.1 Short-term propagation of near-Earth objects using different models

The asteroid chosen for the tool demonstrations is the binary (35107) 1991 VH. The first reference trajectory is obtained from the HORIZONS system of JPL [Giorgini and JPL Solar System Dynamics, 2021]. The second model is the numerical integration of the asteroid motion under the influence of the Sun, Earth and Jupiter. Jupiter is the main driver of the secular motion, which is observed as a linear drift in the argument of perihelion and argument of the ascending node. Given the current orbit of (35107) 1991 VH, it only experiences planetary encounters with Earth in the next few centuries. In Figure 2.7, we compare these two models from numerical integration with the present semi-analytical propagation tool.

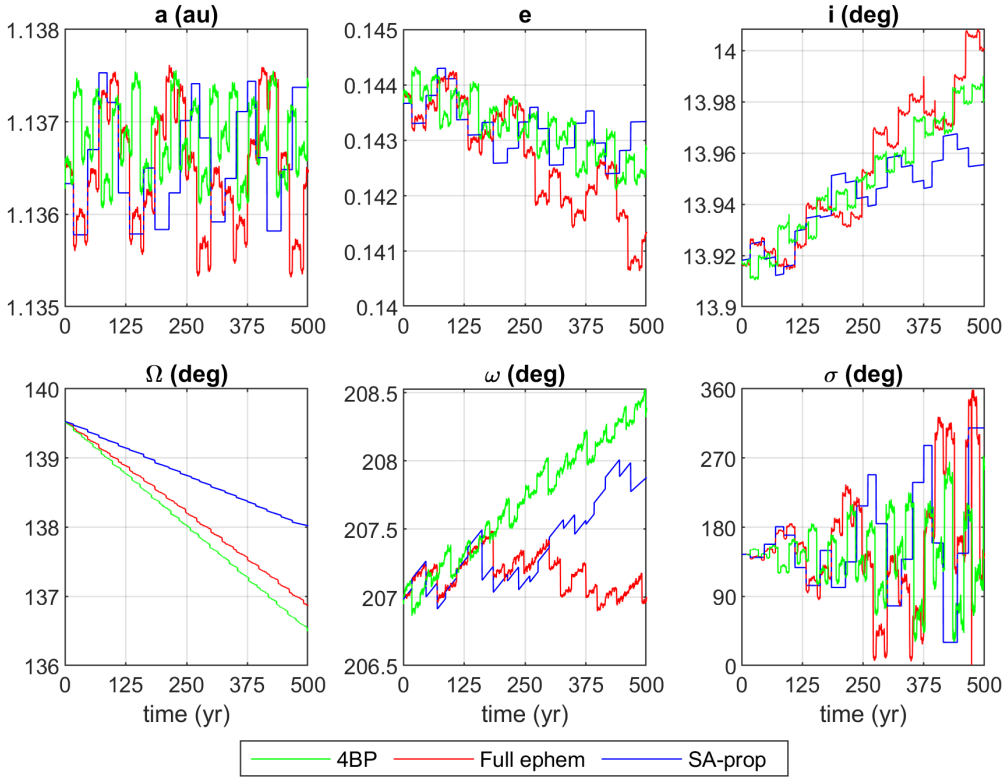


Figure 2.7 Trajectories of a particle that mirrors the binary asteroid (35107) 1991 VH for 500 years.

In the three trajectories we observe similar behavior, although it manifests differently in every element. First, there is a close agreement in the encounter dates of the Sun-Earth-Jupiter integration and the encounters found by the propagation tool that shows in all elements. The encounter dates can be distinguished as the discontinuities in the trajectories, especially in the semi-analytical propagation trajectory. The variation of the semi-major axis is characterized by a random walk from the planetary encounters. In both eccentricity and inclination there is a relevant role of the encounters with an additional secular component that the secular model is able to model.

The dynamics of the argument of the ascending node are dominated by the secular drift. There is not a significant effect that can be perceived by the planetary encounters and this is expected when the encounters occur with a unique planet and close to the node. What we observe is that the secular dynamics including the complete effects of Earth and Jupiter are very similar, and the analytical secular drift is off by about a degree after the 500 years of the propagation. The secular drift rate in the argument of perihelion is not as trivial to compare since it must be observed between encounters, although good agreement is found too. Last, the mean anomaly at epoch evolves over time with an increasing amplitude present in all three models.

### 2.4.2 Long-term propagation and the MOID

The minimum orbit intersection distance (MOID) indicates what the minimum distance between any two points of the two heliocentric Keplerian orbits is. In this case we focus on the orbit of Earth and the orbit of the asteroid. The MOID is also used as one of the criteria to define an asteroid as a potentially hazardous asteroid. There are many algorithms available in the literature to compute the MOID [Gronchi, 2005, Wiśniowski and Rickman, 2013, Armellin et al., 2010]. In this chapter we use the tool derived in Hedo et al. [2018, 2020] based on an asymptotic approach.

The MOID constrains the minimum distance of a possible close encounter. In other words, the periods with a large MOID are absent of close encounters. Three examples are used to visualize time histories of close encounters and the evolution of the MOID for 100,000 years. These are

obtained for high and low eccentricities and inclinations, with initial conditions in table B.1.

The distributions of closest approach distances are shown in figure 2.8 and the unperturbed relative velocity $V_\infty$ at those encounters is found in figure 2.9, with initial conditions given in table B.1. We show the closest approach distance $d_{CA}$ (au) of the encounters and MOID with the planets. The dots indicate close encounters, solid lines indicate the MOID. The color code indicates the planets: (Green) Venus, (Blue) Earth, (Red) Mars.

Case 1 is an example of a NEO with relatively low eccentricity and inclination. In these conditions, close encounters are only possible with Earth and at a low relative velocity. The MOID oscillates secularly with long periods of low MOID. Case 2 is an example of an opposite scenario in which both eccentricity and inclination are large. In the secular evolution of the MOID this translates in short periods of low MOID and long periods absent from encounters. This is a scenario in which the semi-analytical propagation of the asteroid allows a rapid propagation until

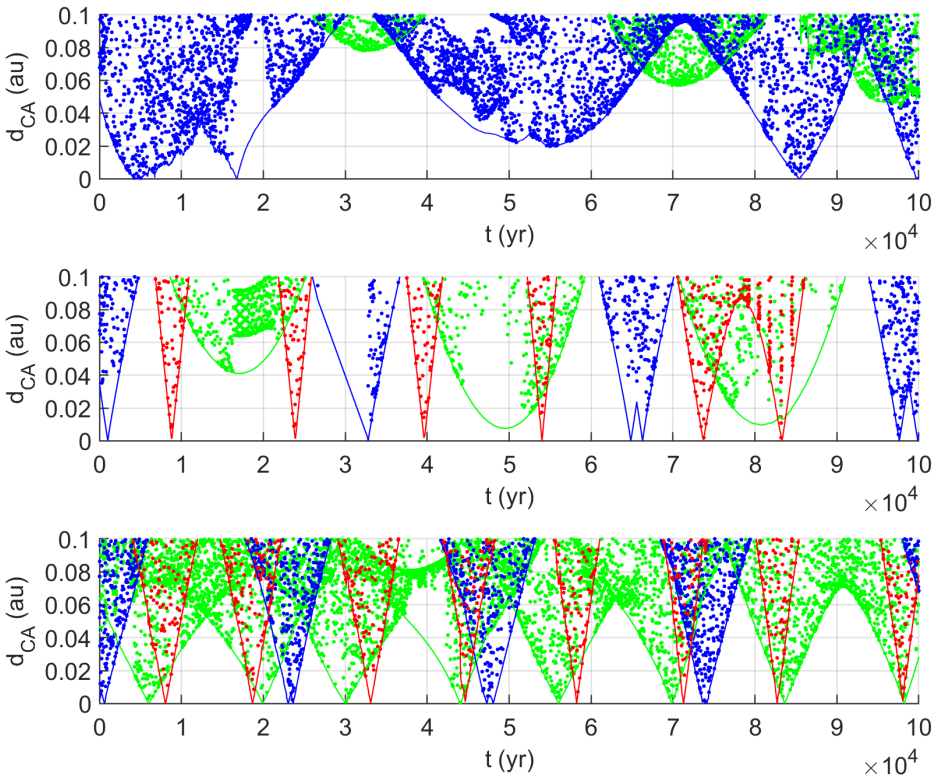


Figure 2.8 Distance of closest approach of close encounters in the semi-analytical propagation of the fictitious NEOs Cases 1-3.

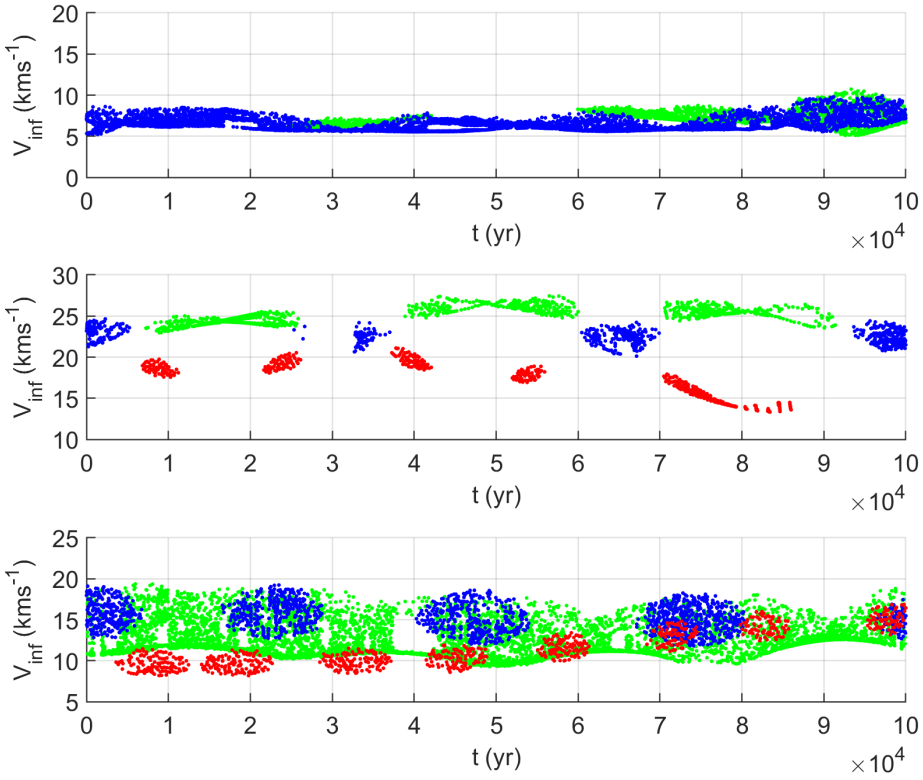


Figure 2.9 $V_\infty$ at closest approach of close encounters in the semi-analytical propagation of the fictitious NEO Cases 1-3.

the next period of frequent encounters. Case 2 faces fast close encounters with Venus, Earth and Mars.

Case 3 is an example of a NEO with high eccentricity and low inclination. This combination of factors leads to a large frequency of close encounters with the inner planets. In this case, encounters are very frequent with Venus, Earth and Mars. The close encounters experienced by Case 3 are with a relative velocity smaller than in Case 2 given the reduced inclination. Even under the elevated frequency of close encounters, the secular signature of the MOID is maintained. The structure persists until the event of an energetic close encounter. The occurrence of such encounters is just a matter of probability of having the right timing during the low-MOID intervals of the secular propagation.

### 2.4.3 Statistics of long-term propagation

The chaotic nature of the dynamics implies that the study of the orbital evolution over long timescales should be done statistically. Given the uncertainty in the orbit solution of an asteroid, we can sample a large number of particles and study the dynamical paths that the different particles take. Because of the sensitivity to initial conditions in planetary encounters, very well determined distributions diverge in a few centuries to widely different paths. After demonstration of these dynamics and its relationship to the number of planetary close encounters found, we propose statistical models for the growth in uncertainty.

**Monte Carlo long-term propagations**

We demonstrate the growth in orbital uncertainty by Monte Carlo propagation of 500 particles that sample uncertainty distributions around a nominal trajectory for 500,000 years. We inspected 7 examples: first, in detail, orbit solution of (35107) 1991 VH; then, the orbit solution of (175706) 1996 FG3; last, the previous Cases 1-5 of table B.1 with artificial orbit uncertainties as described in appendix B.

Figure 2.10 shows the time histories of the individual runs of the cloud of points originally neighboring (35107) 1991 VH. Initial conditions are given in table B.1 as obtained from HORIZONS [Giorgini and JPL Solar System Dynamics, 2021] and uncertainties in the distribution are obtained from JPL's Small-Body Database as described in appendix B.[1] Elements shown are perihelion, eccentricity, inclination, argument of the ascending node, argument of perihelion and minimum orbit intersection distance (MOID). Grey lines show individual simulations, black lines are the median of the 500 simulations of each parameter shown.

The results in Figure 2.10 show that the cloud of particles distributes over a wide region of near-Earth space. On the order of hundreds of thousand years, the dispersion is accomplished by the less frequent very close encounters. Eccentricity and inclination show the secular component

[1] As extracted from JPL's Small-body Database Lookup (Date accessed: 2021-04-25) - Available for query at: ssd.jpl.nasa.gov/tools/sbdb_lookup.html

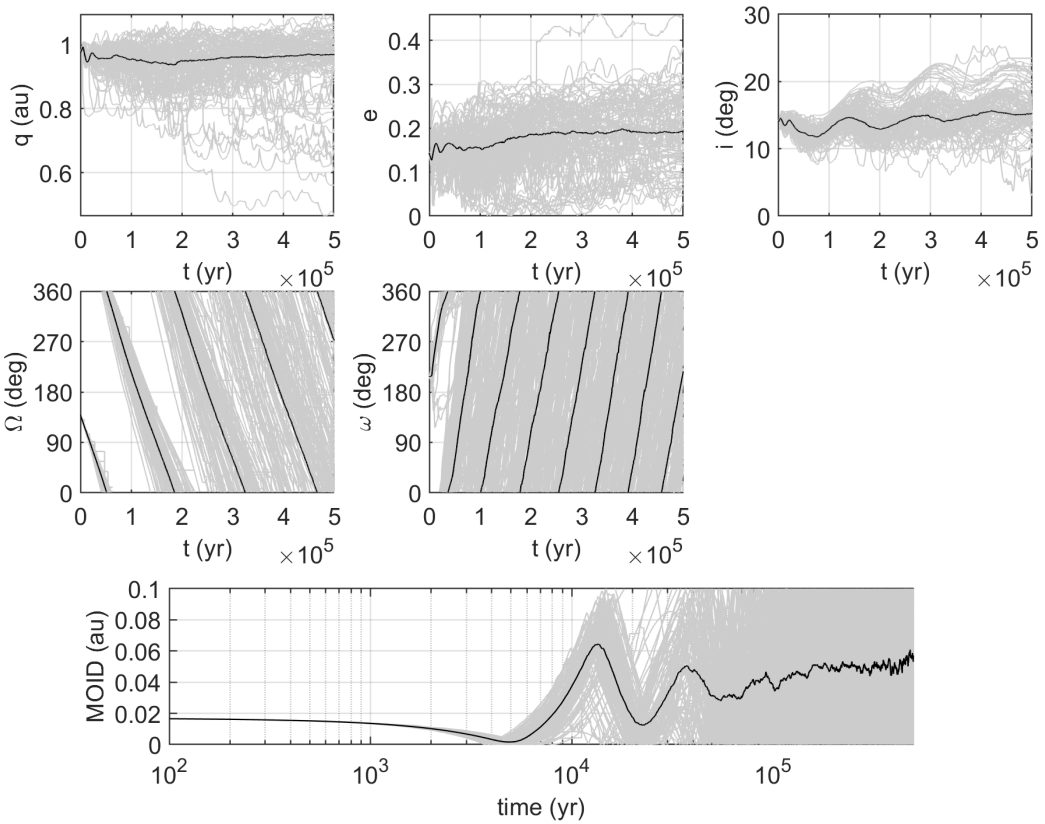


Figure 2.10 500,000 year Monte Carlo semi-analytical propagation of asteroid (35107) 1991 VH.

but are dispersed by the presence of encounters. The dynamics of argument of ascending node and argument of perihelion remain mainly secular with a degree of dispersion because of the presence of encounters. Note that the initial uncertainty on the orbit of (35107) 1991 VH is very small as shown while demonstrating the chaotic dynamics nature in Figure 2.1 of the background section. As it was observed in the detailed analysis of a shorter simulation in figure 2.7, the mean anomaly at epoch changes completely with small changes in the semi-major axis. This fact reflects in the long-term simulations as a complete uniformization after just a few centuries.

The binary (35107) 1991 VH currently presents a MOID that is decreasing. This means that after a few millenia the probability of experiencing very close encounters increases. In the statistical analysis, this probability shows in that a fraction of the fictitious asteroids experience such encounters. We observe that towards the end of the simulation there is a large dispersion in inclination and perihelion distance. By the end of the simulation, the angles $\Omega - \omega$ are dispersed

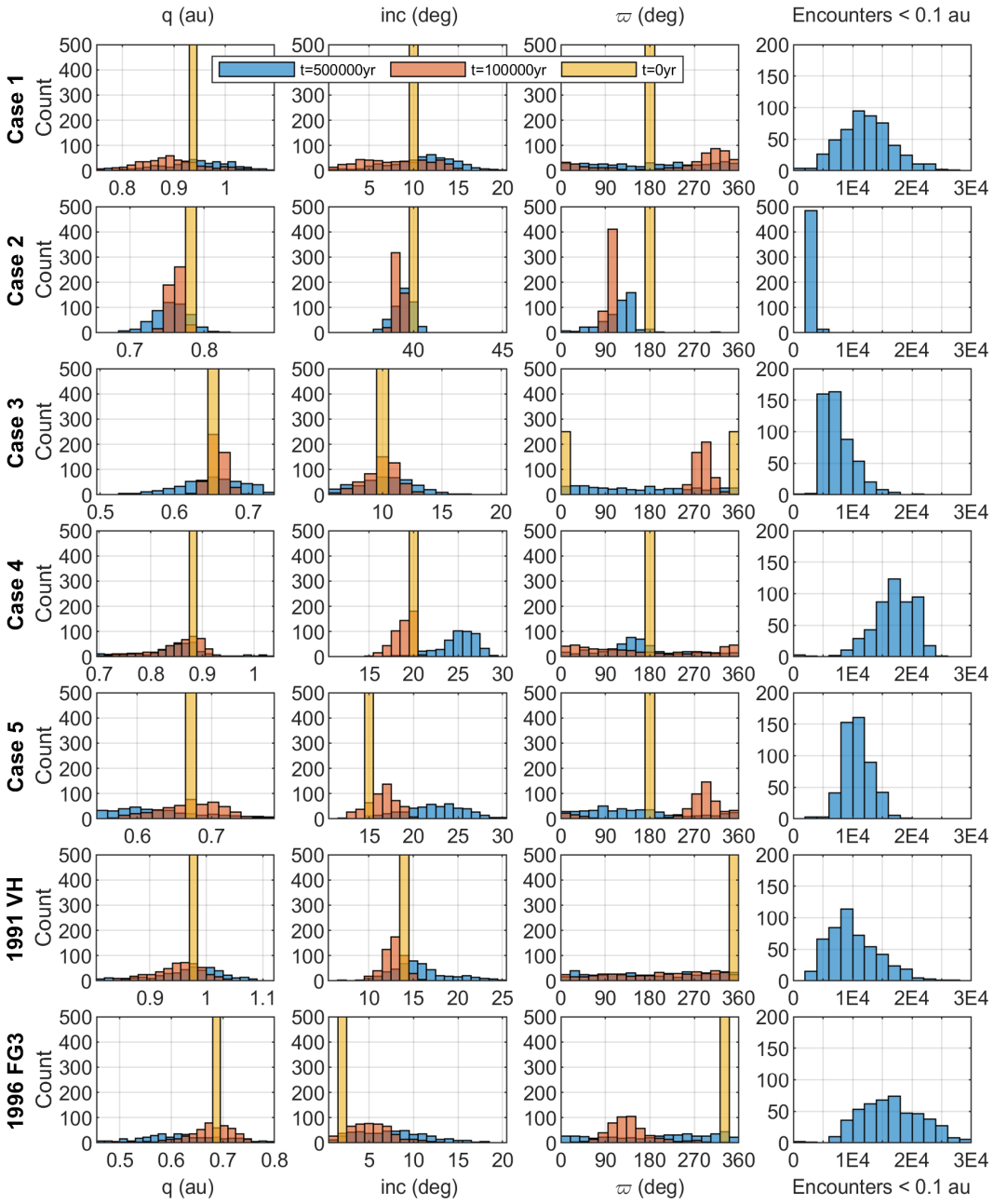


Figure 2.11 Semi-analytical propagation of asteroid Cases 1-5, (35107) 1991 VH, (175706) 1996 FG3 for 500,000 years.

along a linear drift as caused by numerous close encounters that not only change these angles, but modify the secular dynamic frequencies.

The long-term dynamics of 6 more examples are integrated for 500,000 years. These are the Cases that we used to illustrate the long-term dynamics with initial conditions in Table B.1. The case of the binary (175706) 1996 FG3 is also added to the discussion, as it is the other target of exploration of the Janus mission [Scheeres et al., 2020]. The uncertainties of (175706) 1996 FG3 and (35107) 1991 VH are sampled based on their publicly available orbit solutions. In the case of the fictitious asteroids we used an arbitrary distribution. Both approaches are explained in detail in the appendix B.

The statistical distributions after 100,000 and 500,000 years are shown in Figure 2.11 as histograms. The distributions in semi-major axis-eccentricity and semi-major axis-inclination are shown at the initial times, after 50,000 yr and 500,000 yr in Figure 2.12. The 500 virtual asteroids that are generated at the initial time per case are in the same bar of the histogram. The effect of repeated encounters causes the distributions to spread along near-Earth space. This dispersion is clearly shown in the perihelion distance in all cases, with a general trend of a decrease in the distance. Figure 2.12 additionally shows this spread of all the cases together.

The presence of mean motion resonances in the inner Solar System can protect asteroids from close encounters Milani et al. [1989]. In the semi-analytical propagation of near-Earth asteroids the orbits may drift to these regions, as observed in Figure 2.12. The resonance regions are found for semi-major axes larger than $a = 1$ au. In these cases encounters with the Earth stop occurring for a period of time. However, this clustering of particles is not found in numerically integrated populations or in the discovered population of near-Earth asteroids.

The process of obtaining the secular long-term perturbation eliminates the short-period perturbations. The latter perturbations cause an oscillation in the orbit elements of non-negligible amplitude. In order to measure the influence of this effect, we included an analytical oscillation in the semi-major axis with the frequency of the orbital period and an amplitude of the order of 0.01 au. This extension completely eliminates the artificial mean motion resonance regions. The

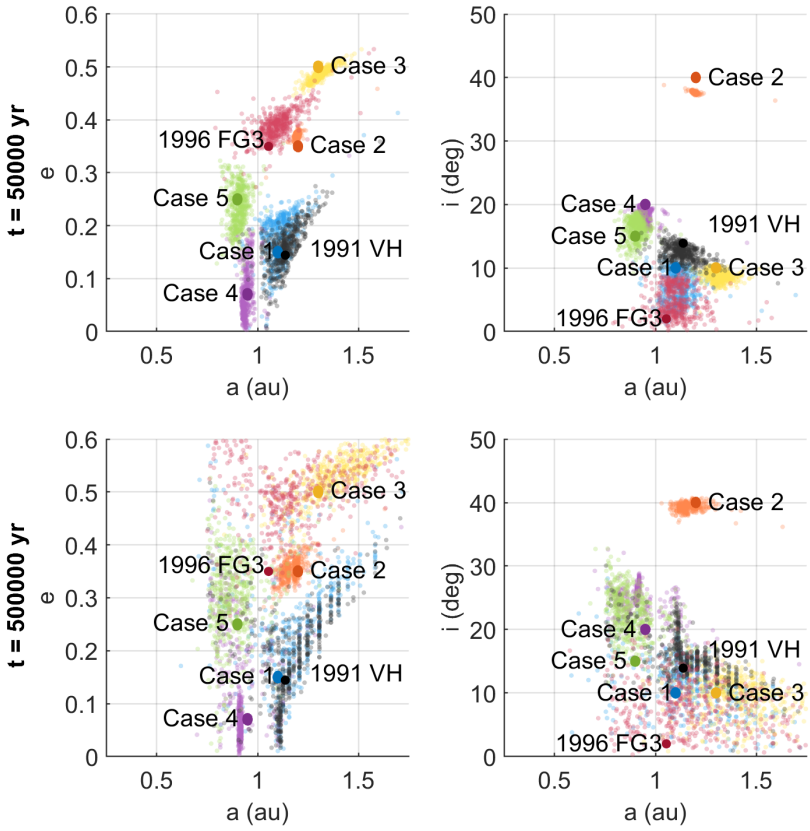


Figure 2.12 Dispersion in the distributions of the asteroids in table B.1.

analytical characterization of the short-period perturbation is left as future work, as its contribution must be considered for the complete set of orbital elements and is not expected to significantly modify the obtained distributions.

### Statistical Models for the Long-term dynamics

The recorded number of encounters are shown in Figure 2.13 as the mean and standard deviation of 500 particles. More details on the statistical distributions over time are shown in Figure 2.14. We show the standard deviation of semi-major axis, eccentricity, inclination as function of the number of encounters and square root of time. In addition, we show the variation of the mean semi-major axis, eccentricity and inclinations over time. Using this information we describe the dynamical evolution of these test cases.

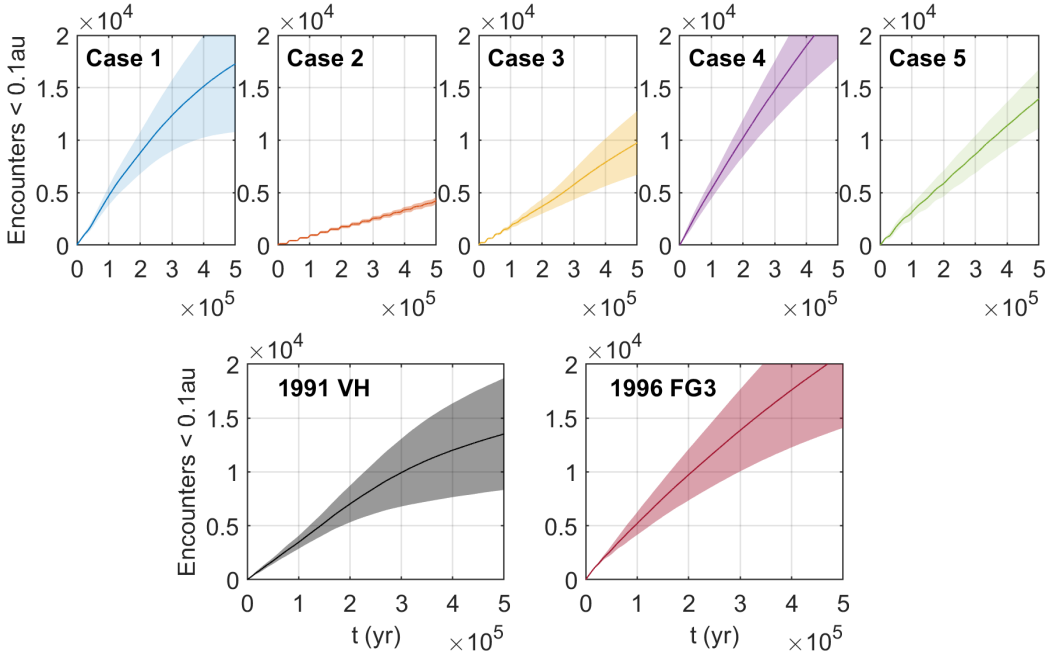


Figure 2.13 Number of encounters experienced by the test cases in table B.1.

In general, we observe that asteroids encountering the planets more frequently disperse their distributions faster. This is the case for the Janus targets and Case 1, that present the largest standard deviations increase in the simulation time (Fig. 2.14). This dispersion is not only shown in the elements, but also in the number of encounters (Fig. 2.13).

The evolution of the distribution as caused by encounters could be modelled as a random walk. If this hypothesis is true, then the standard deviation in the population increases linearly with the square root of time. Figure 2.14 tests graphically this hypothesis for semi-major axis, eccentricity and inclination. Initially in all cases there is a fast increase in the standard deviations. After the few first millennia, some of the distributions follow the hypothesis of the linear relationship $\sigma \propto \sqrt{t}$, especially in the semi-major axis.

In eccentricity and inclination, we observe that there is a secular component in the evolution of the distribution. The secular component is observed in both the evolution of the standard deviation and the mean of the variations (Fig. 2.14). These are shown with respect to the initial values to have a common reference in the comparison of cases.

The dispersion in semi-major axis modifies the secular rates of the drift in argument if perihelion and argument of the node. This effect combined with the direct variation of the angles during planetary encounters leads to the uniformization of the distribution in $\omega, \Omega$. In the duration of our simulations of 500,000 most cases approach this uniformization as we showed in figure 2.11.

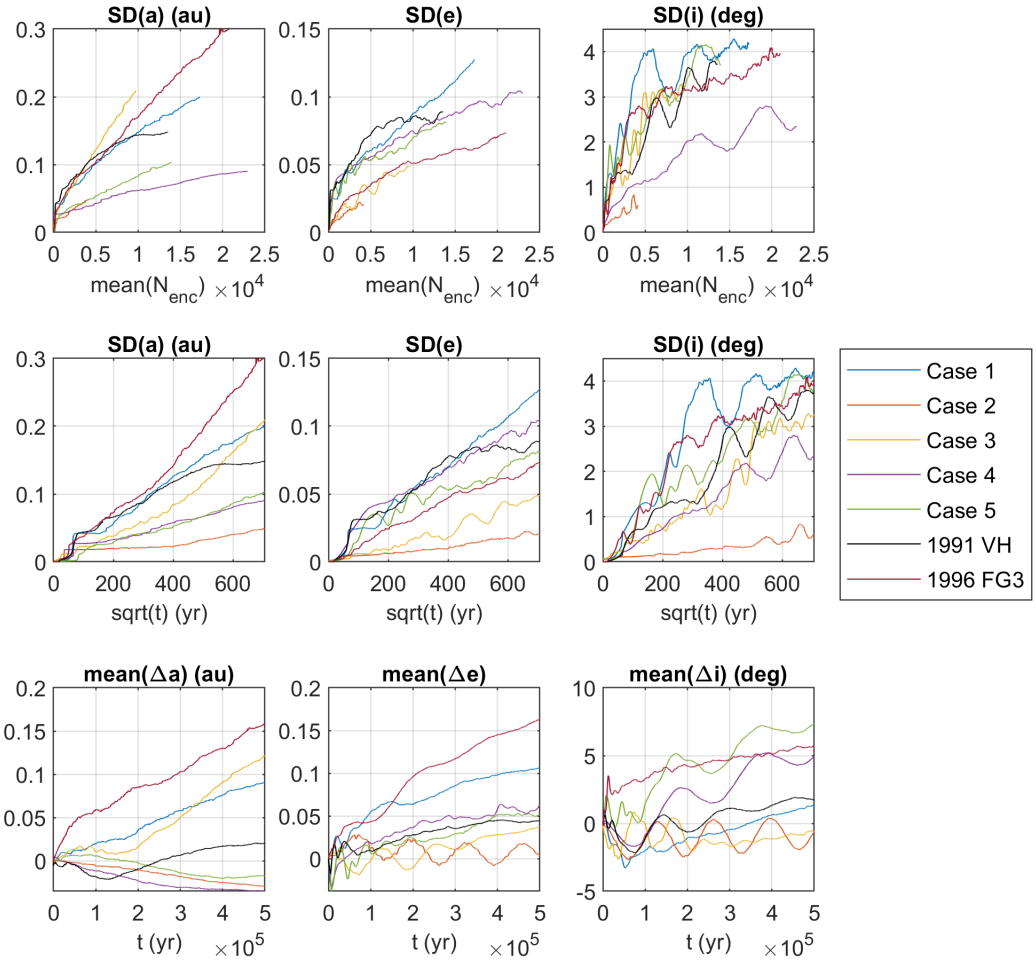


Figure 2.14 Statistical evolution of the distributions of the test cases in table B.1.

We can compute more rigorously whether the distributions can be considered uniform by conducting the chi-squared test on the longitude of perihelion $\varpi = \omega + \Omega$. Figure 2.15 shows the result of the chi-squared test of a uniform distribution over the simulation time for all cases. If the p-value is larger than our threshold of $p = 0.05$, we can consider that our null hypothesis of the uniform distribution of $\varpi$ is true. Cases 1, 3, 4, (175706) 1996 FG3 and (35107) 1991 VH reach this threshold, while Cases 2 and 5 do not approach the significance by the end of the simulation time.

It is interesting to show the evolution of the p-value compared to the mean number of encounters. In figure 2.15 we show how the distribution of Case 3 tends to the uniformization in $\varpi$ with less encounters than other cases that achieve this distribution earlier in the simulation time. This is expected since this case experiences more frequent encounters with the most massive planets and with a slower relative velocity, which means that the impact of these encounters in the dispersion of their distributions is larger.

From the general trends that we observed, the only case that is very different is Case 2, that experiences much fewer encounters. As we illustrate in Figure 2.8, Case 2 experiences close encounters much less frequently than the other cases. The relative velocity is also larger in this case, which means that the effects of the encounters are not as strong. The case of (175706) 1996 FG3 is more difficult to fit in the general description of the dynamics, as the close encounters do not cause such a fast dispersion of the distribution. This binary asteroid is studied in more detail in section 3.2.

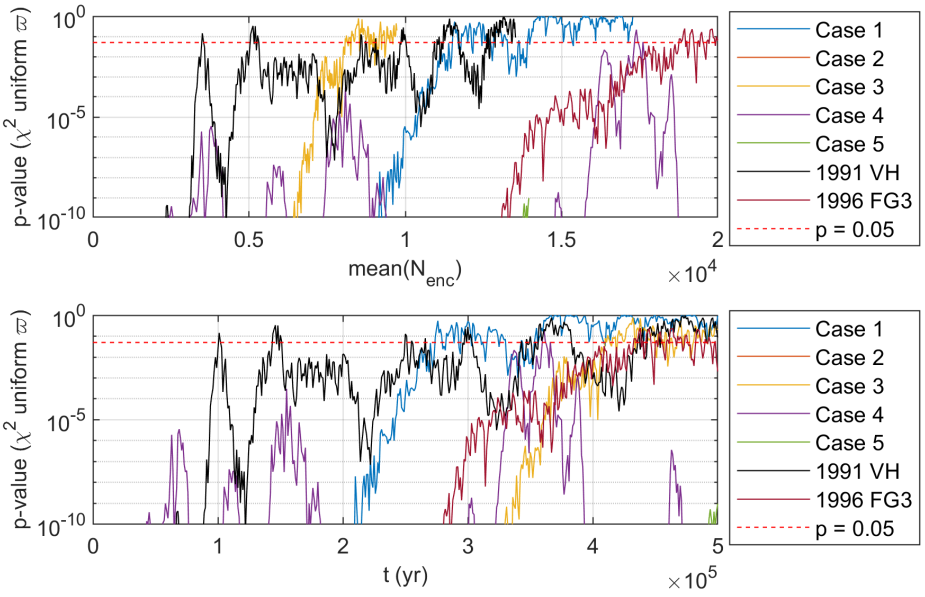


Figure 2.15 P-value of the chi-squared test of the uniform distribution of the longitude of perihelion $\varpi = \omega + \Omega$ for the 5 test cases given in table B.1.

## 2.5 Discussion

The semi-analytical propagation tool shows the main dynamical effects observed in long-term numerical integration of the inner Solar System. The secular drifts caused by Jupiter move the asteroids between the vicinities of the different planets of the inner Solar System. This effect causes a seasonal presence of strong close encounters that can disturb both the orbit of the asteroid and its physical properties. While the time-scales of these events is of millions of years [Fang and Margot, 2012], if we sample a large enough number of particles we can measure the probabilities of collisions or the potential disruption of other physical properties of asteroids. The measurement of the collision probabilities was outside the scope of this chapter, but in this work a few collisions were detected in the uncertainty sampling of the asteroids.

The analytical modelling of the dynamics far from the planets was done using the Laplace-Lagrange theory, which works well in a large fraction of the NEO population. For this reason we defined a region in near-Earth space in which the secular model works best, as shown in Figure 2.4. However, we could extend the modelling in the regions of large eccentricity and inclination. In the previous section we describe the low frequency of encounters that is characteristic of asteroids with high inclination, specifically with Case 2. An asteroid of these characteristics would be likely to be dominated by the Lidov-Kozai effect, in which there is an exchange between high inclination-low eccentricity periods and low inclination-high excentricity periods. This would mean that Case 2 evolves to become a case closer to Case 3, in which encounters are more frequent. The use of analytical models of the Lidov-Kozai model [Kinoshita and Nakai, 2007] for the perturbed propagation is left for future work.

Using the semi-analytical propagation tool we observe the stochastic nature of the dynamics. However, the effect is different on each of the elements. While in semi-major axis we observe what could be described as a random-walk process, the angles $\Omega$ and $\omega$ become uniformly distributed. Eccentricity and inclination show a mixed effect between a random-walk that adds dispersion to the distribution and the oscillations driven by the secular theory.

## 2.6 Conclusions

In this chapter we present a rapid semi-analytical propagation tool for asteroids in the inner Solar System. The tool combines an analytical solution for the secular dynamics and the evaluation of planetary encounters. The derived solution of planetary encounters proves to accurately model the effect of the majority of flybys that asteroids experience in the inner Solar System.

The long-term effect of the perturbation by Jupiter is captured by the analytical secular solutions in a large fraction of the NEO population. The combination with detection and evaluation of close encounters recreates the full dynamics as we demonstrate for the case of (35107) 1991 VH.

The description of the orbits of NEOs in long-term timescales must be done statistically. We showed how the different elements can be represented by different distributions, and how the time it takes for the elements to become statistical depends on the frequency of close encounters. Through the sampling of different NEO cases we inspect the stochastic models that represent the long-term evolution of the orbital elements. The use of a fast semi-analytical propagation tool allows an efficient study of the dynamics of asteroids.

# Chapter 3

# Binary Asteroids Excitation during Close Encounters

## 3.1 Introduction

The semi-analytical propagation allows us to track the encounters experienced by asteroids in the inner Solar System, which can perturb the physical properties of asteroids. The orbits of binary asteroids can be disrupted by a very close encounter [Meyer and Scheeres, 2021]. In this Chapter we study the orbital history of the targets of the exploration mission Janus [Scheeres et al., 2020]: the two binaries (35107) 1991 VH and (175706) 1996 FG3. The stochastic long-term dynamics in the last million years are modeled in section 3.2 by sampling a large number of particles from their current orbit uncertainties described in section B. We model the evolution of these statistical distributions by a random walk in semi-major axis, eccentricity and inclination and a uniform distribution in longitude of perihelion in section 3.2.1. Then, in section 3.2.2 we compute the probability that (35107) 1991 VH and (175706) 1996 FG3 could have been potentially disrupted by a close encounter in this period of a million years. We repeat this analysis for the target of the NASA/APL mission DART target: the Didymos system in section 3.3.

## 3.2 Orbit histories of the Janus mission targets

The orbit time histories of (35107) 1991 VH and (175706) 1996 FG3 are shown respectively in figure 3.1 and figure 3.2. We show the perihelion distance, eccentricity, inclination and argument of the ascending nodes. For clarity, we show only a subset of the runs and the median of the full distribution of 1000 runs. The minimum orbit intersection distance (MOID) is shown for the inner

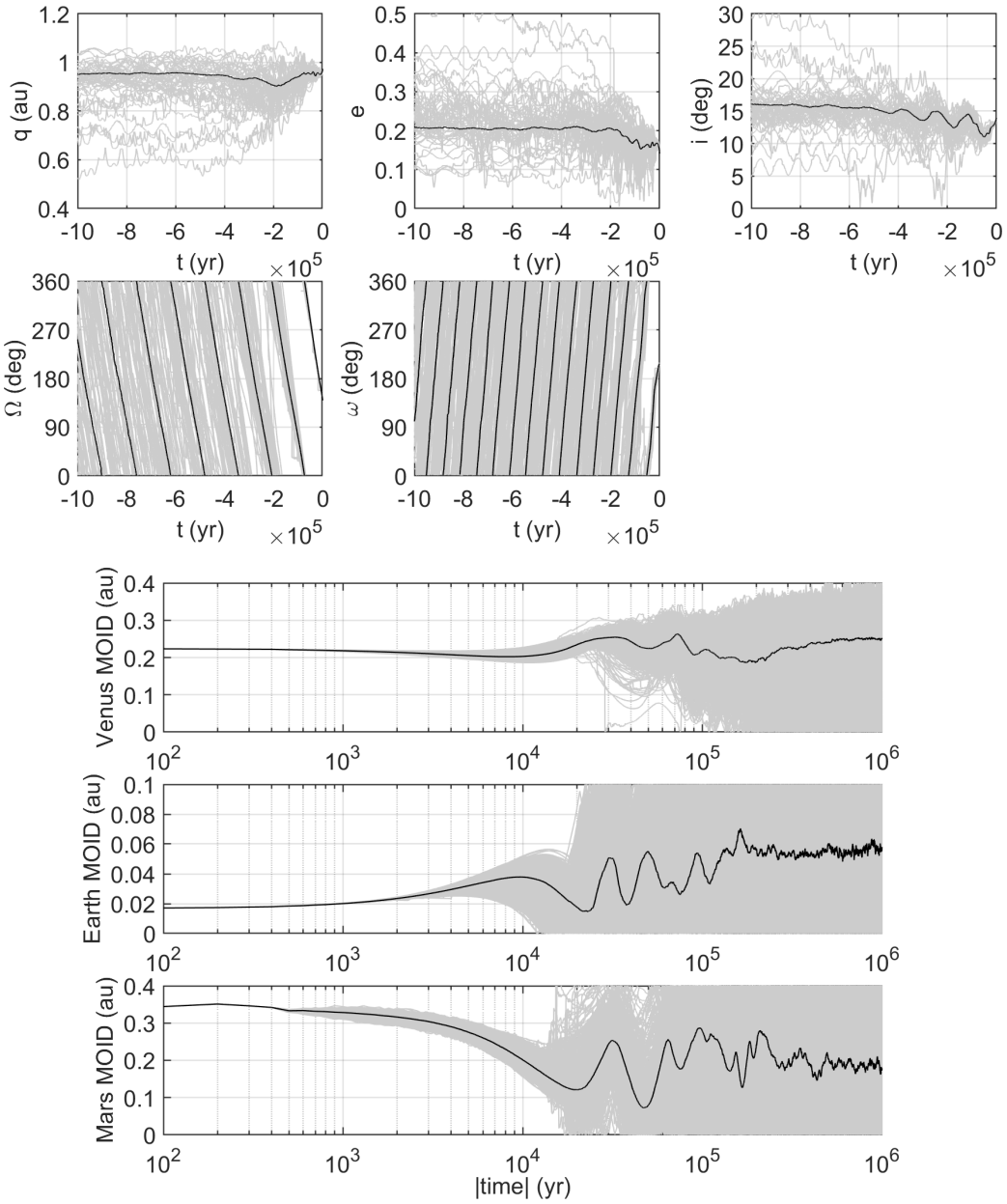


Figure 3.1 Orbit history of (35107) 1991 VH in the last million years.

Solar System planets Venus, Earth and Mars. These metrics show when close encounters with these planets are possible. The presence of frequent close encounters causes the dispersion of the orbit histories. This feature manifests in the orbit history of (175706) 1996 FG3, in which the period of very low Venus MOID corresponds with a dispersion in the overall statistical representation of the orbit.

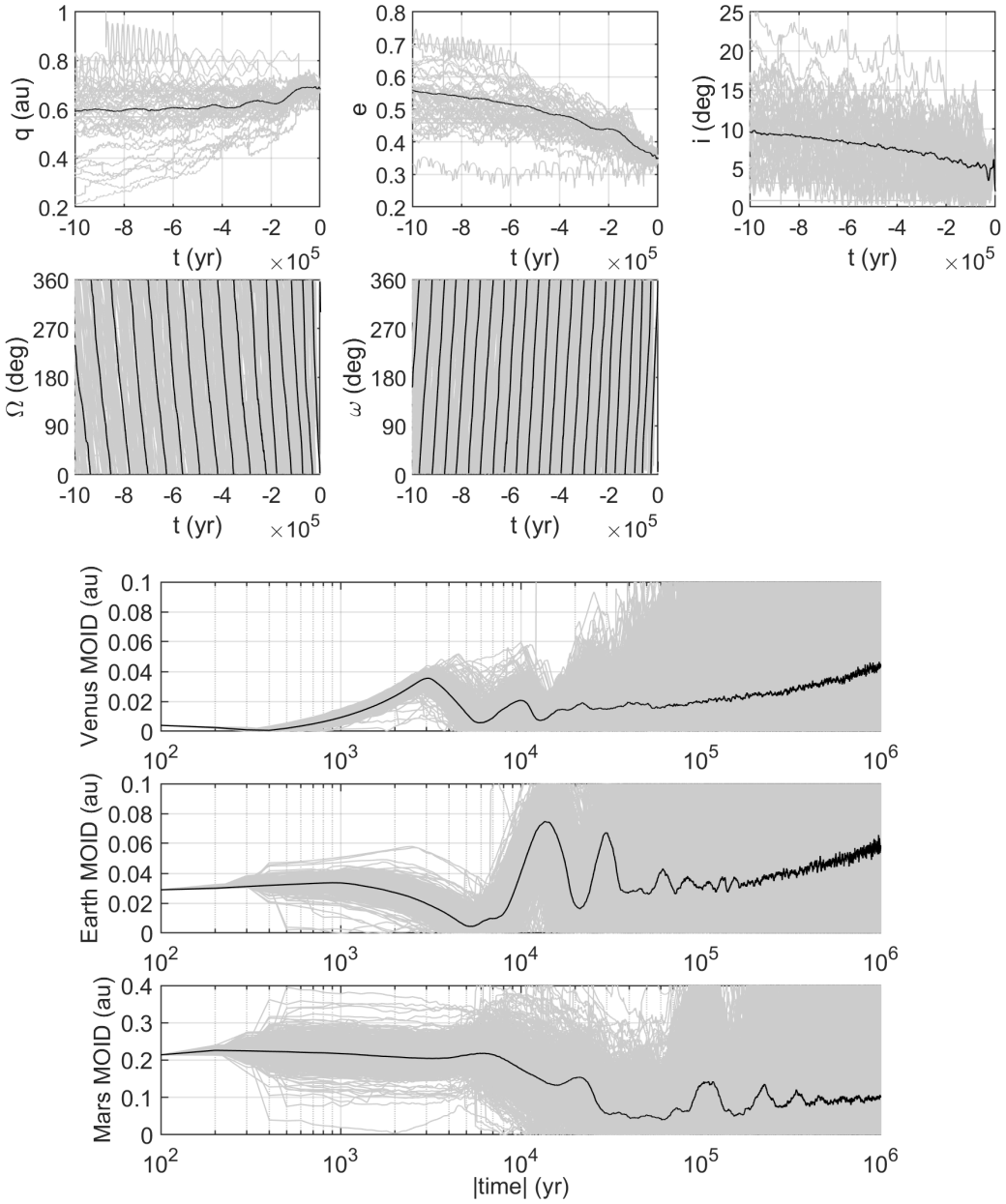


Figure 3.2 Orbit history of (175706) 1996 FG3 in the last million years.

Similarly to the long-term dynamics into the future studied in section 2.4, the initially very close distribution becomes a wide statistical distribution when propagated far into the past. In Figure 3.3 we show histograms of the orbit elements and the number of encounters recorded below a closest approach distance threshold of 0.1 au. The orbit evolution of (35107) 1991 VH is mostly a spread around the initial conditions. However, (175706) 1996 FG3 is in a particular initial orbit

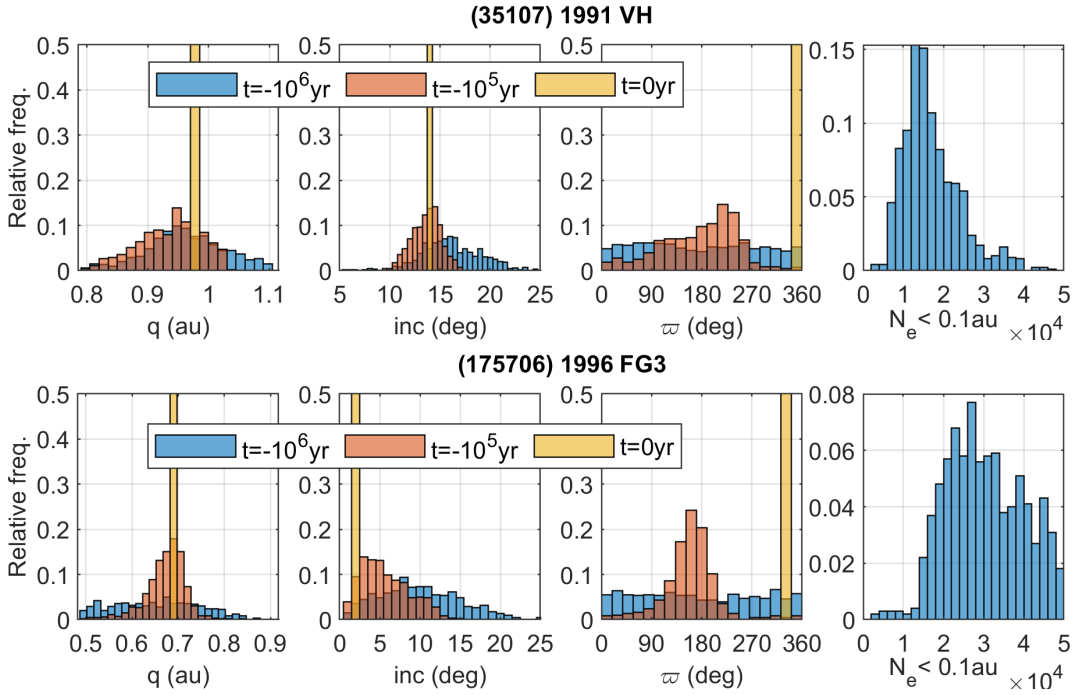


Figure 3.3 Histograms of the orbit history of (35107) 1991 VH and (175706) 1996 FG3 at the initial time, 100,000 years ago and 1 Myr ago.

with low inclination. On average, the very low inclination and high eccentricities drift toward a smaller eccentricity and higher inclination that are more frequent in the secular cycle. In both cases, the longitude of the perihelion becomes uniformly distributed. In the next section we characterize this uniformization process.

Table 3.1 Stochastic modelling of the long-term dynamics of the Janus targets

| Target Name | $k_a$ (au/$\sqrt{yr}$) | $k_e$ (1/$\sqrt{yr}$) | $k_i$ (deg/$\sqrt{yr}$) | $t$ ($yr \cdot 10^3$) | $N_e < 0.1$ au |
|---|---|---|---|---|---|
| (35107) 1991 VH | $0.2661 \cdot 10^{-3}$ | $0.1799 \cdot 10^{-3}$ | $6.0055 \cdot 10^{-3}$ | -434 | 11800 |
| (175706) 1996 FG3 | $0.3688 \cdot 10^{-3}$ | $0.0944 \cdot 10^{-3}$ | $11.598 \cdot 10^{-3}$ | -797 | 29800 |

### 3.2.1 Stochastic modelling of the long-term dynamics

In section 2.4 we show that we can model the long-term dynamics with a random walk in semi-major axis, eccentricity and inclination. In addition, the latter two present also the influence of the oscillations of the secular theory. We also want to study the uniformization in the longitude of the perihelion, as this process occurs with time but also with a repeated number of close encounters.

The random-walk model can be characterized by a linear increase in standard deviation with the square root of time. Figure 3.4 shows the standard deviation of the 1000 Monte Carlo experiment that we conducted into the past of the two Janus targets (35107) 1991 VH and (175706) 1996 FG3. We fit a linear model to the standard deviation evolution, and measure the slopes to compare the evolution of the two targets. In the case of (35107) 1991 VH we avoid the use of the full simulation time, as the standard deviation bends from the initial linear increase. The slower increase after this period occurs when the distribution migrates from a configuration with low velocity encounters. The opposite case occurs with inclinations, in which the rapid increase of (175706) 1996 FG3 from the low-inclination initial regime slows down after the initial growth.

The measured slopes are reported in table 3.1, showing that the random walk of (175706) 1996 FG3 is faster in semi-major axis and inclination. However, because of the bends in the progression after a few hundred thousand years, the final standard deviations are not substantially larger than the ones of (35107) 1991 VH after the million years into the past in eccentricity and inclination.

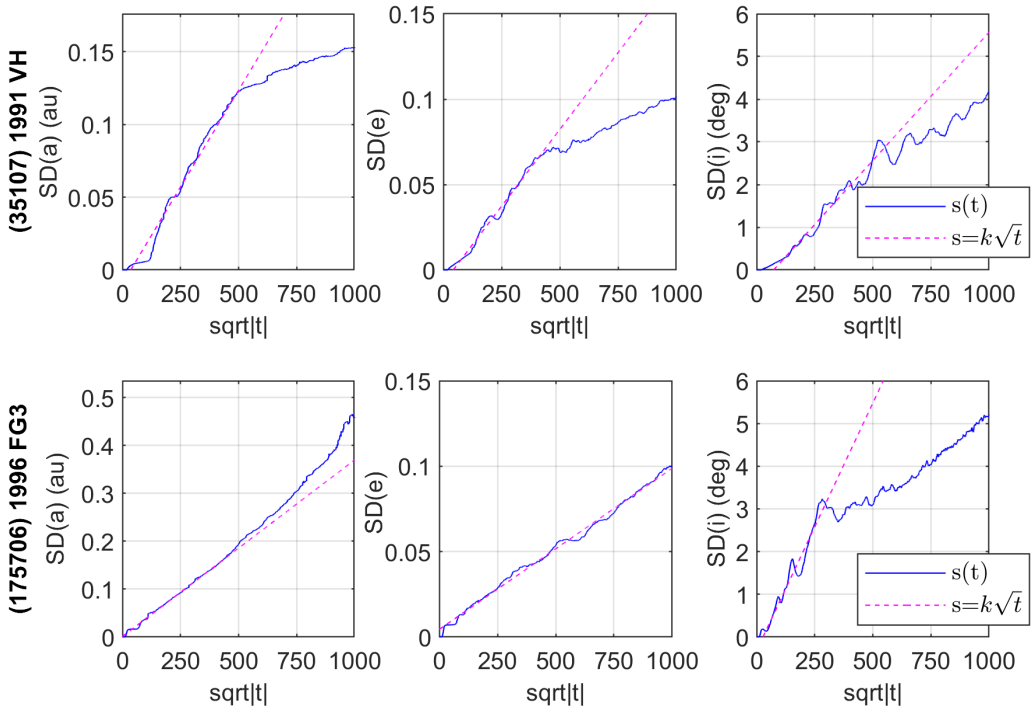


Figure 3.4 Random walk statistical modelling of the evolution of semi-major axis, eccentricity, inclination of (35107) 1991 VH and (175706) 1996 FG3.

The process of uniformization of the longitude of perihelion is shown in figure 3.5. We conduct the chi-squared test of the uniform distribution over the 1 Myr simulation, to find when the hypothesis of the uniform distribution is significant. In table 3.1 we show the first time in which this criterion is satisfied, both in time and mean number of encounters: -434,000 years and a mean of 11800 encounters for (35107) 1991 VH, and -797,000 years and a mean of 29800 encounters for (175706) 1996 FG3.

The uniformization of (35107) 1991 VH is faster than the uniformization of (35107) 1991 VH in both time and mean number of encounters. It is remarkable that (35107) 1991 VH takes a much lower mean number of encounters. This is explained by the faster relative velocities of the encounters of (175706) 1996 FG3 and a larger fraction occuring with Mars, a less massive planet. The relative velocities of a few of the recorded flybys are shown in figures 3.6 and 3.7 in the context of studying the probability that a close encounter could potentially disrupt the binaries.

The comparison between the two binary systems highlights how the effect of the encounters depends on the relative velocities and the mass of the planets. In general, slow encounters and with larger planets are more efficient at causing the distributions to become uniform. However, depending on the heliocentric orbit these encounters may be more or less frequent. Thus, leveraging both effects is required to obtain a stochastic representation of the long-term dynamics of NEOs under frequent encounters.

### 3.2.2 Potentially disruptive planetary encounters

The two binary targets of the Janus mission present different relative orbits as observed by radar and photometry [Pravec et al., 2016, Meyer et al., 2021], showing that (175706) 1996 FG3 is in a stable orbital state and (35107) 1991 VH is in a chaotic state. The perturbed state of (35107) 1991 VH could be explained by a recent very close encounter with the inner Solar System planets [Heggie and Rasio, 1996]. Thus, it is of interest to characterize the frequency of such encounters in the orbital history of asteroid binaries.

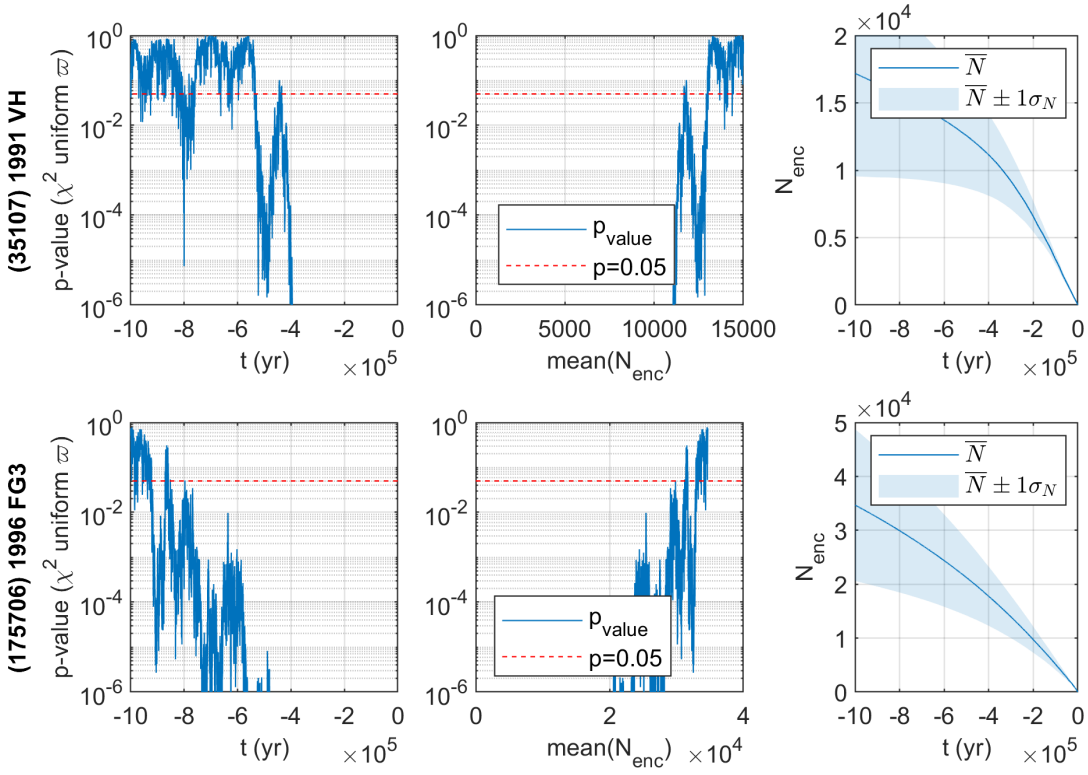


Figure 3.5 P-value of the chi-squared test of the uniform distribution of the longitude of perihelion $\varpi = \omega + \Omega$ of (35107) 1991 VH and (175706) 1996 FG3.

Using the semi-analytical propagation tool we obtain the history of flybys over a long time period of time. The perturbation in the orbit of a binary system during a planetary close encounter is studied in detail as described in [Meyer and Scheeres, 2021]. In this section we combine both results to predict the frequency of a disrupting flyby.

The effect of the close encounter on the binary can be modelled as an impulsive variation in the binary Keplerian elements. In Meyer and Scheeres [2021] the effect of close encounters to singly synchronous binary asteroids is studied. The variation in semi-major axis, eccentricity, and inclination obtained with numerical methods was compared to analytical expressions for the impulsive variation in binary Keplerian elements [Fang and Margot, 2012]. We used these analytical expressions as they provide an estimate of the variation as function of the relative velocity and distance of closest approach.

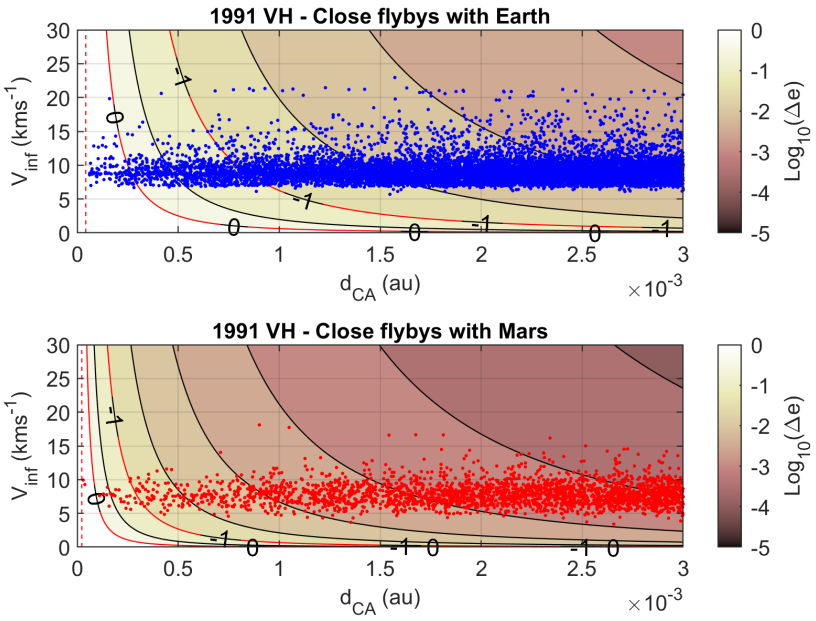


Figure 3.6 Potentially disruptive encounters recorded in the history of (35107) 1991 VH ($N_{MC} = 1000$)

For every binary and encountered planet we can generate contours of the variation of the eccentricity. In Figures 3.6 and 3.7 we show these contours respectively for (35107) 1991 VH and (175706) 1996 FG3. In every figure we highlight two levels, a variation of 0.1 in eccentricity, and a variation of 1, which would mean that the binary is completely separated. The probability of disruption in the binary orbit increases as the relative velocity and closest approach distance are reduced. For reference, the radius of the planet is shown as a dashed line.

Using the semi-analytical propagation tool we track the close encounters below the threshold of 0.003 au, above which the variation in the binary Keplerian elements becomes negligible. For each binary we generate 1000 trajectories for a million years into the past. All the encounters that are found in this threshold are plotted in figures 3.6 and 3.7 and separated by encountered planet.

The encounters potentially disruptive recorded for (35107) 1991 VH with Earth and Mars are shown in figure 3.6. Less than 1% of the recorded encounters are with Venus so the map with this planet is not included. The relative velocities of the flybys are mostly found between 5 and 15 km $s^{-1}$. In the case of (175706) 1996 FG3 this range of possible relative velocities is larger in all

the planets. In addition, many encounters are found with quite slower $V_\infty$, which means that even if they are not as close, they can still potentially cause a disruption.

As we observed in figure 2.13, (175706) 1996 FG3 experiences more frequent encounters. However, the regions in which the encounters are potentially disruptive depend on the current orbital configurations of the binaries. In this case, (175706) 1996 FG3 requires closer and slower encounters to obtain the same mean variation in binary elements.

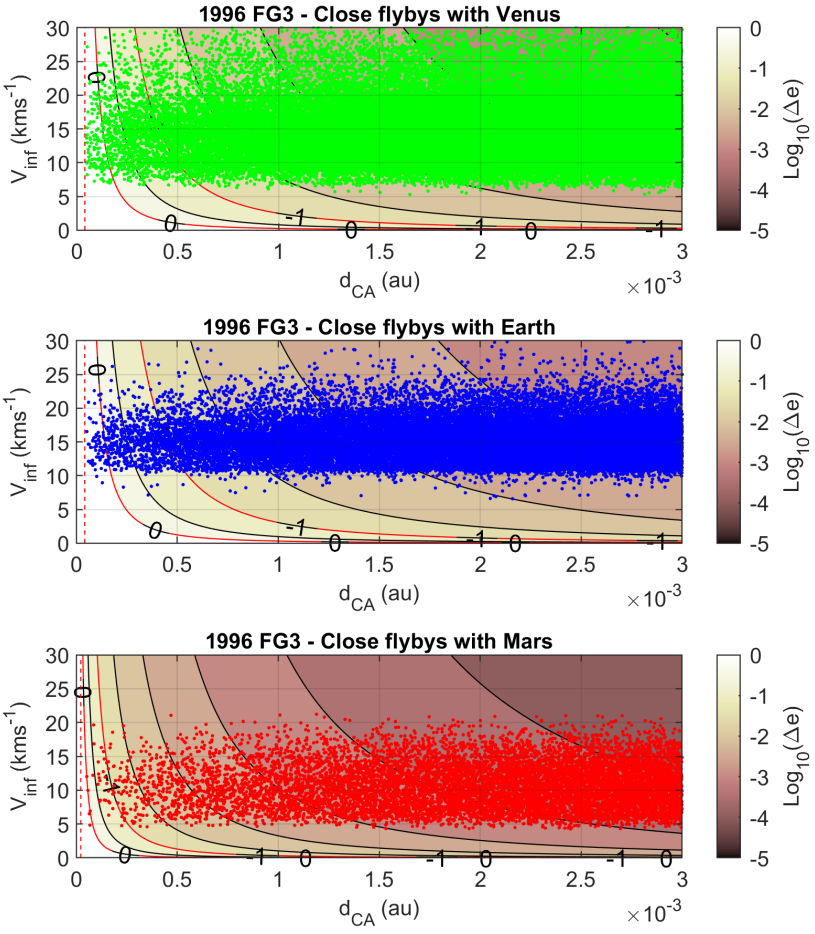


Figure 3.7 Potentially disruptive encounters recorded in the history of (175706) 1996 FG3 ($N_{MC} = 1000$)

Considering the orbit history in a million years, a non-negligible probability exists that both binaries have been potentially disrupted at some point. However, it is possible that the signature of these potential disruptions vanishes if there is energy dissipation in the system. Thus it is relevant to study the probability that the binary orbits have potentially been disrupted recently in the orbit histories. We can study the first fraction of the long-term secular periods, in which the particles still have not mixed.

Figure 3.8 shows the history of potentially disruptive encounters in the recent periods of frequent encounters. The close encounters below the line of mean variation in binary eccentricity of 0.1 are highlighted with a black circle and the dashed line marks the radius of Earth. The probability of disruption is based on the number of encounters found below thresholds of mean $\Delta e = 0.1$ for low disruption and $\Delta e = 1$ for high disruption, with their corresponding confidence intervals shown in dashed lines.

The last period of possible very close encounters that we find for (35107) 1991 VH starts before the last 10,000 years. As determined by a mean variation in binary eccentricity of 0.1, we find that 61 of the 1000 test runs experience a potential disruption in the period of time up until the last 30,000 years. When we incorporate the next period of close encounters, the probability of a potential disruption increases to 131 out of 1000 runs in the last 60,000 years.

Given the current orbit state of (175706) 1996 FG3, we find very close encounters with Venus in the last millennia. Because of the more restrictive closest approach distance for a potential disruption to happen, only 10 out of the 1000 test runs experienced this potential disruption in this period of frequent encounters. If we consider the last 10,000 years, then the probability increases to 54 cases in which at least one potentially disruptive encounter was found.

If we keep increasing the time in which we consider all the potentially disruptive encounters, we can estimate the probability that a potentially disruptive encounter occurs. These probabilities are shown in figure 3.8 with the corresponding 95% confidence intervals. The probability of suffering a disruptive encounter of (175706) 1996 FG3 increases faster than the probability of (35107) 1991 VH. This is explained by the significantly higher number of recorded close encounters.

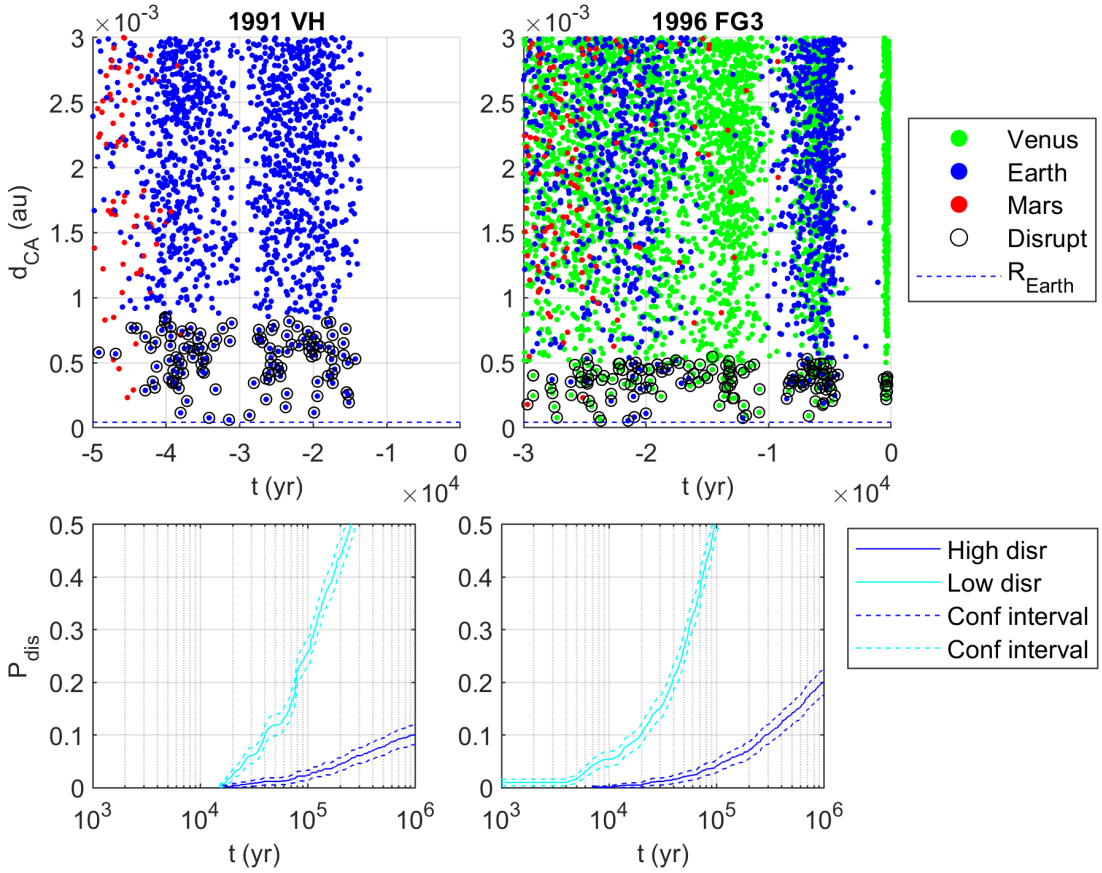


Figure 3.8 Recent potentially disruptive encounters and probability of disruption for the NASA Janus targets.

Thus, it is not possible to explain the chaotic state of (35107) 1991 VH only from the long-term probability of experiencing such encounters. However, a low probability in recent times combined with the incapability to dissipate the perturbation in a long time could explain the chaotic state of (35107) 1991 VH. Thus, future work will be done in the lines of characterizing the timescales of the dissipation of perturbations due to close encounters.

## 3.3 Potentially disruptive encounters of the DART target

On September 26, 2022 the DART spacecraft impacted Dimorphos, the secondary of the 65803 Didymos binary asteroid system. The result was a reduction of the orbital period of Dimorphos by $33.0 \pm 1.0$ minutes [Thomas et al., 2023]. Before the arrival of DART to the Didymos system we explored whether or not planetary close encounters could explain any perturbations in the orbit

of Dimorphos, as reported in Richardson et al. [2022]. Conversely, this analysis also shows if the orbit of the Didymos system is exposed to frequent planetary close encounters that could perturb the system.

We propagate 1000 virtual particles from the orbit solution of Didymos for 500,000 years into the past. In order to verify that the secular rates are captured accurately we propagated the orbit of Didymos for a shorter period of time using numerical integration. The initial conditions are in table B.1, and the uncertainty covariance in table B.4. Note that we extracted the 6x6 subset from the 7x7 matrix including the uncertainty in the non-gravitational acceleration A2.

With the pre-impact binary system model, we generate the same contours of the required closest approach distance-relative velocity for significant excitation of the binary system. In Figure 3.9 we show these contours, together with all the close-slow flybys recorded in this period. In this case, we show the Earth flybys in blue and Mars flybys in Red. We compute the probability of excitation based in these thresholds as function of time. We find that there is less than a very small probability that Didymos was excited by a flyby in the last 100,000 yr.

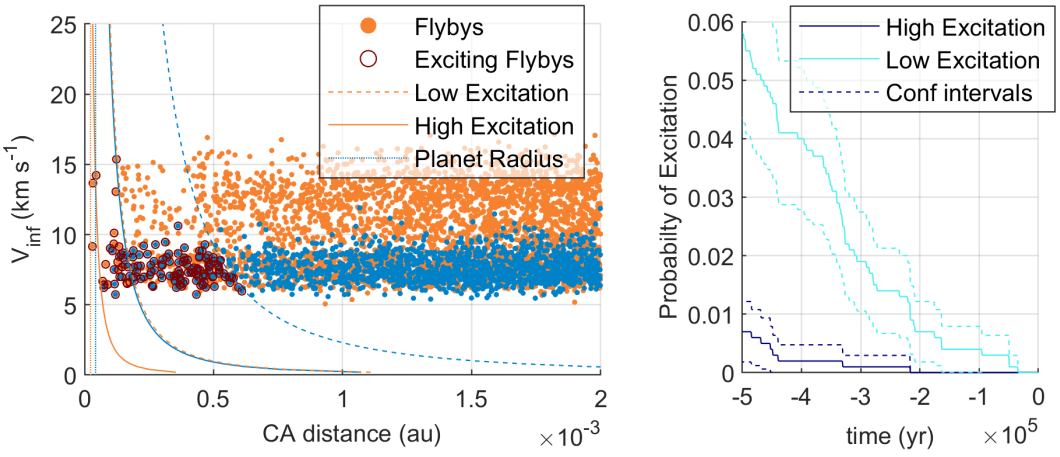


Figure 3.9 Recent potentially disruptive encounters and probability of disruption Didymos, the NASA/APL DART target.

## 3.4 Conclusions

We studied in detail the orbital histories of the Janus mission targets: (35107) 1991 VH and (175706) 1996 FG3. We characterized the encounters that can cause a potentially disruption of the binary orbits and computed the frequency of such encounters for the Janus targets as well as for the DART target. Additional modeling of the effects of close encounters to other physical properties of asteroids will allow the study of the frequency of disruptive events. These are just a few potential examples of the benefits of a fast propagation tool for Solar System studies in the fashion of the presented tool.

# Chapter 4

# Obliquity Evolution of NEAs

## 4.1 Introduction

The spin poles of asteroids evolve under thermal torques or YORP effect (Yarkovsky – O'Keefe – Radzievskii – Paddack) [Vokrouhlický et al., 2015]. Analytical theories predict that the obliquity, the angle between the orbit plane of the asteroid and the spin pole (See Figure 4.1), evolves to equilibrium configurations of 0, 90 or 180 deg [Golubov et al., 2021]. However, in the inner solar system only sometimes we find asteroids near these equilibria. In this chapter we leverage the evolution of the heliocentric orbit in contrast to torques that drive the obliquity to these equilibria.

The observed spin poles in near-Earth relate to the sources of asteroids in the inner solar system, with the Yarkovsky acceleration is considered to be one of the most important effects[Morbidelli and Vokrouhlickỳ, 2003]. When obliquity $> 90$ deg, the resulting acceleration causes a decrease in semi-major axis bringing the asteroids closer in turn to the $\nu_6$ resonance and then to the orbit of the Earth [Vokrouhlický et al., 2015]. Thus, in the inner Solar System we expect more asteroids with retrograde rotation than posigrade rotation.

NEA population models predicted the ratio between retrograde and prograde rotators to be $2 \pm 0.2$ [Bottke et al., 2002], which was first measured by La Spina et al. [2004] to be $2^{+1}_{-0.7}$. The measured Yarkovsky accelerations constrain the obliquities in agreement with the predicted ratio [Tardioli et al., 2017]. Additional spin poles have been produced since and made available in the Light-curve database [Warner et al., 2021] as shown in Figure 4.2. We then cross-matched the information of the spin poles with the orbit elements as obtained from JPL's Small-body Database,[1]

showing a ratio of $2.1 \pm 0.9$. We find that there are 65 uniquely defined spin axes of NEOs. For the rest, we show both solutions of the spin pole. Even if the error is significant, the databases show consistency with the results in the literature.

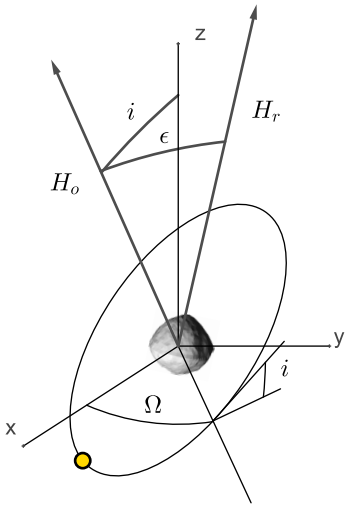


Figure 4.1 Obliquity ($\epsilon$) is the angle between the orbit normal plane ($H_o$) and rotational angular momentum ($H_r$). Orbit normal plane is function of inclination ($i$) and ascending node ($\Omega$).

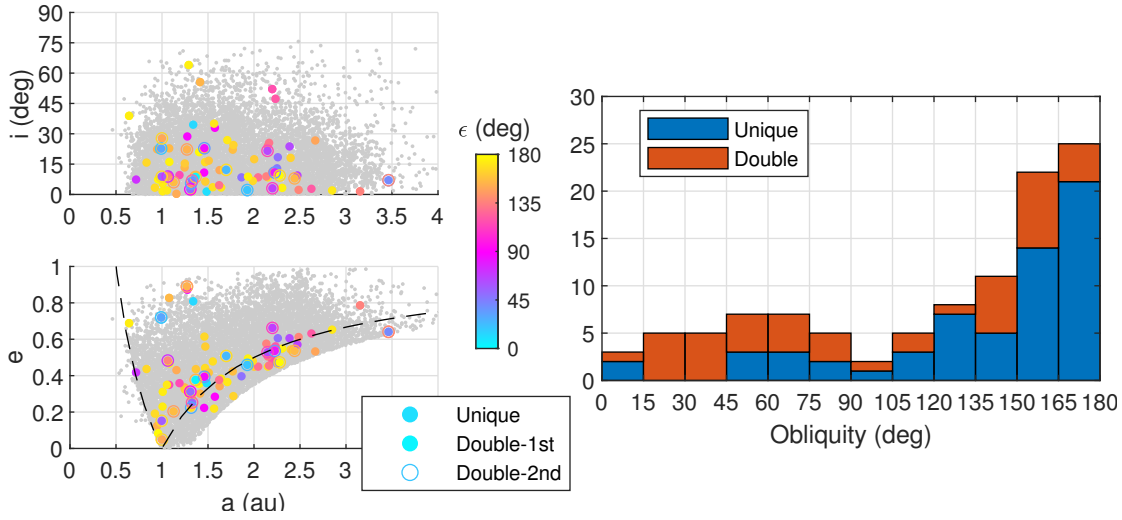


Figure 4.2 Obliquities of 85 near-Earth asteroids with spin pole solutions.

[1] As extracted from JPL's Small-body Database (Date accessed: 2023-05-05) - Available for query at: `ssd.jpl.nasa.gov/tools/sbdb_query.html`

Considering the evolution of the spin states to be uncoupled from the orbital dynamics, the YORP effect drives the obliquities of asteroids to equilibrium states of 0, 90 or 180 degrees [Golubov and Scheeres, 2019, Golubov et al., 2021]. The thermal torque caused by large-scale asymmetry of the asteroid is referred as normal YORP. In addition, boulders in the surface of the asteroid with thermal conductivity can cause a significant contribution called tangential YORP [Golubov et al., 2014].

In chapter 2 we model the evolution of the heliocentric orbit of asteroids in the inner solar system. In particular, the secular perturbation of Jupiter causes the ascending node $\Omega$ to drift secularly and oscillations in the inclination $i$, which define the orbital plane. In addition, close encounters cause the orbit to become stochastic in time scales comparable to the time scales of the evolution under YORP. For this reason predicted obliquities far into the past or the future are also stochastic. These effects have not been previously combined to model the long-term dynamics of the obliquity. Vokrouhlickỳ et al. [2005] included spin-orbit resonances for the secular drift of the orbit, but did not include YORP torques. Vokrouhlický et al. [2007] proposed a secular drift with YORP torques. However, the heliocentric orbits were assumed constant, hence the orbit plane as well as the intensity of the solar flux.

This chapter is structured as follows. In section 4.2 we keep the spin state constant, and explore two models for the heliocentric orbit: a secular drift in section 4.2.1 and the stochastic evolution with close encounters in section 4.2.2. These two scenarios show the timescales of the orbit evolution and how that translates into the evolution of the obliquity. Then, in section 4.3 we include torques on the spin pole to investigate how the obliquity components of the torque can affect the overall evolution of obliquity of near-Earth asteroids.

## 4.2 Obliquity Evolution: Stationary Spin State

In this section we study the evolution of the obliquity if we keep the spin state of the asteroid constant. First, as the underlying secular evolution from the perturbation of Jupiter. Then, considering the stochastic orbit evolution under the presence of planetary close encounters.

### 4.2.1 Obliquity Evolution due Secular Orbit Drift

In section 2.3.2 we describe the secular model for the long-term dynamics assuming the perturbation of Jupiter. Figure 4.3 shows how the secular drifts manifests into obliquity over time for an asteroid of initial inclination $i = 15$ deg. We propagate the obliquity for the same heliocentric orbit and 3 semi-major axes. The black vector corresponds to the initial $\hat{H}_o$, which traces the black line with the secular drift. We sample 5 different spin poles, shown in inertial space. From an initial obliquity of 0, the spin poles are generated by shift the spin pole $\Delta$ of $\pm 5$ deg and $\pm 10$ deg. Given the precession of the orbit normal pole around the vertical axis, the shifts increasing the latitude ($\Delta = +5, +10$ deg) reduce the amplitude of the obliquity oscillations. On the other hand, we find that reducing the latitude below the orbit angular momentum ($\Delta = -5, -10$ deg) creates an offset of the oscillations while roughly maintaining an amplitude of $2i$. The right panels show how different semi-major axis changes the fundamental frequency of the secular drift.

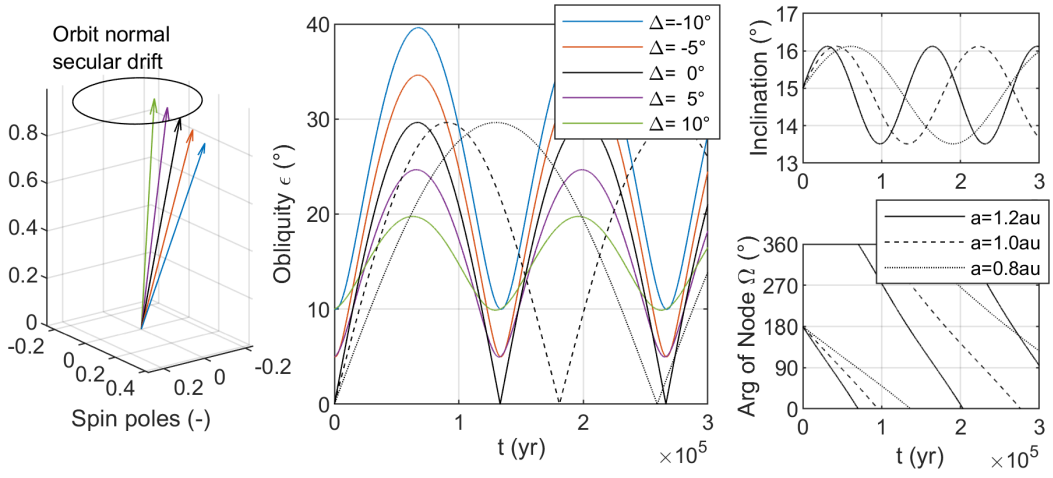


Figure 4.3 Evolution of obliquity as the orbit normal drifts secularly while the spin pole is kept constant.

The orbits of NEOs span a wide range of semi-major axes, eccentricities and inclinations, as shown in Figure 4.2. Asteroids of high eccentricities and/or inclinations can be under the Lidov-Kozai effect, in which periods of high eccentricity exchange periods of high inclination [P. and Thomas, 1996]. The third-body perturbing potential of Jupiter can be expanded in orbit elements to analytically find the secular frequencies of the drift in ascending node and argument of perihelion [Kinoshita and Nakai, 1999, 2007]. These frequencies are very similar to the secular frequencies of the Lagrange-Laplace cycle. If the asteroid is in this regime, then we would expect higher amplitude of the oscillations of inclination, which would imply a larger amplitude of the oscillations of obliquity. The oscillations in eccentricity can change the intensity of the YORP effect, although the time average does not differ substantially from the original intensity.

### 4.2.2 Stochastic evolution under close encounters

The model used for the propagation of the orbit in the presence of close encounters is the semi-analytical propagation tool developed in chapter 2. Figure 4.4 shows an example of a Monte Carlo simulation of a fictitious near-Earth asteroid (Initial conditions: $a = 1.4$ au, $e = 0.3$, $i$=15 deg, $\Omega$=90 deg, $\varpi$=180 deg, $\sigma$=90 deg). A small uncertainty of $10^{-6}$ is chosen for semi-major axis (au), eccentricity; inclination, argument of the node, argument of perihelion, and mean anomaly at epoch in radians. Figure 4.4 shows how the presence of encounters causes a rapid increase in the uncertainty of the distribution. In chapter 2 we show how this dispersion can be modeled as a random walk in $a$-$e$-$i$ [Froeschle et al., 1995]. The parameter $\bar{r} = a(1 - e^2)^{1/4}$ is a typical scaling factor for the magnitude of thermal forces and torques, usually with $\propto \bar{r}^{-2}$. We can see how this factor also becomes stochastic after a few thousands of years.

Considering the stochastic evolution of the heliocentric orbit we find significant variations in asteroid obliquity. In the example of Figure 4.4 we can see how the range of possible obliquities is between 165 and 180 degrees in timescales of $10^4 - 10^5$ years. Not only there is a significant growth in the uncertainty of the predictions, but also each individual run experiences oscillations in obliquity.

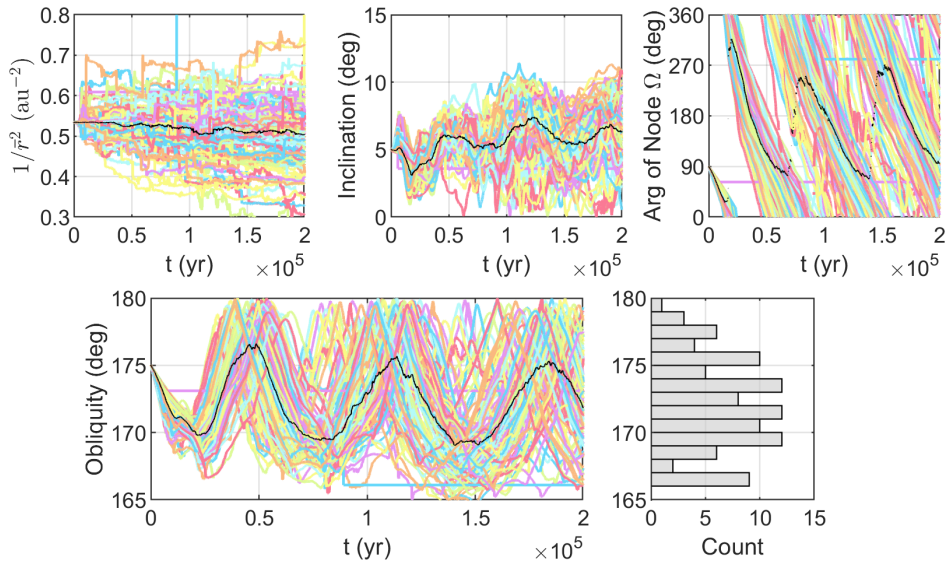


Figure 4.4 Evolution of obliquity after semi-analytical propagation of the asteroid orbit and constant spin state.

## 4.3 Obliquity Evolution: Torques and Orbit evolution

The rotational and orbital dynamics of NEOs are coupled through multiple effects. Obliquity is one of the parameters that defines the Yarkovsky acceleration, which influences the orbit evolution. However, in long time-scales this effect is shadowed by the growth in uncertainty due to the presence of planetary close encounters, as discussed in Section 2.2.1. In this chapter we will assume that this acceleration is negligible and proceed to compute the orbit evolution as decoupled form the rotational dynamics. On the other hand, we will consider the effect of the position of the NEO in the torques applied to the spin state.

Modeling YORP torques is challenging due to the dependency on the morphology of the surface of the asteroid. Large boulders in the surface all the way to the regolith can make a significant contribution to the spin rates [Golubov and Lipatova, 2022]. The limiting behaviors are believed to be certain equilibrium spin rates at the equilibrium obliquities of 0, 90 or 180 deg. In this study we focus on the obliquities of NEOs. Thus, in order to reduce the complexity of the analysis, we will only consider the obliquity components of the torques: the ones that modify the spin pole of the asteroid but not the spin rate.

We consider YORP-like torques with the same dependencies on the orbit but only the obliquity component torque. Thermal torques are scaled with the orbit, proportional to $\bar{r}^{-2}$. The torque applied on the asteorid will depend on a time-varying obliquity, which is function of the orbit normal.

In this section we describe the model for implicit dependency of the external torques on the orbit. The methodology for the propagation of the obliquity consists in two steps: after precomputing the orbit history, we use it as the parameters that drive the external torques acting on the asteroid. Then, we propagate the angular momentum under these torques. This includes the mentioned assumption that the orbit propagation is uncoupled from the obliquity because of neglecting the Yarkovsky acceleration.

### 4.3.1 Rotational Dynamics under Obliquity Component Torques

The main assumption of this model is that the asteroid is in principal axis rotation about the short axis. Thus, the angular momentum can be expressed as $\boldsymbol{H}_r = I_z \omega \hat{\omega}$, so that the direction of the rotational angular momentum $\hat{H}_r$ and spin pole $\hat{\omega}$ are always parallel. Even though in some occasions asteroids experience tumbling, it is found that tumbling may not weaken the YORP effect [Vokrouhlický et al., 2015].

We model the change in angular momentum under the only external torque of an obliquity-YORP-like and conservation of rotational angular momentum $\frac{d\boldsymbol{H}_r}{dt} = \boldsymbol{T}$, the inertial derivative of $\boldsymbol{H}_r$ integrated in inertial J2000 Ecliptic Frame. We use analytical models of the magnitude of the normal YORP that depend on the obliquity $\epsilon$ and the intensity of the solar flux. Both parameters can be computed over time from the instantaneous orbit elements, which are obtained from the orbit propagation described in section 4.2.2. The YORP torque can be split into a component in the direction of the spin pole $T_z$ and an obliquity component $T_\epsilon$:

$$T_z = \boldsymbol{T} \cdot \hat{\omega} \tag{4.1}$$

$$T_\epsilon = \boldsymbol{T} \cdot \hat{\omega}_{\perp 1} \tag{4.2}$$

where $\boldsymbol{T}$ is the torque, we assume $T_z = 0$, and $\hat{\omega}_{\perp 1}$ is the component of the spin vector in the obliquity direction. This direction is defined as:

$$\hat{\omega}_{\perp 1} = \frac{\hat{\omega}\cos\epsilon - \hat{H}_o}{\sin\epsilon} \tag{4.3}$$

where the orbital plane normal vector $\hat{H}_o$ can be directly computed from the osculating orbit elements. The rotational dynamics become:

$$\frac{d\boldsymbol{H}_r}{dt} = T_z\hat{\omega} + T_\epsilon\hat{\omega}_{\perp 1} = T_\epsilon\hat{\omega}_{\perp 1} \tag{4.4}$$

Under normal YORP the dependency of the obliquity torque can be modeled as a function of the coefficient $C_\epsilon$:

$$T_\epsilon = \frac{\Phi R^3}{c} C_\epsilon \sin 2\epsilon \tag{4.5}$$

The scaling factor $\frac{\Phi R^3}{c}$ is function of the solar energy flux $\Phi$, the asteroid's mean radius $R$, and the speed of light $c$. The solar energy flux is scaled by a radius squared law obtained when averaging the torques, $\bar{r}$, derived in detail in Scheeres et al. [2007]. This model of the obliquity dependence holds the correct symmetry properties and is a valid general approximation [Rubincam, 2000, Vokrouhlický and Čapek, 2002, Golubov and Scheeres, 2019]

The YORP coefficients $\{C_\epsilon, C_z, \beta\}$ are dimensionless parameters that depend on the asteroid shape. These coefficients result from the computation of the torques as the integral along the surface of the asteroid. Golubov and Scheeres [2019] include an appendix with the Taylor expansion of the torque elements that leads to the relationship between the spin rate and obliquity component $\alpha = C_\epsilon/C_z = 2/3$ and $\beta = 1/3$. Under these torques the obliquities tend to a few asymptotic or equilibrium values. For $C_z, C_\epsilon > 0$, the equilibrium obliquity is 90 deg. If $C_z, C_\epsilon < 0$, the equilibrium obliquity is either 0 or 180 deg.

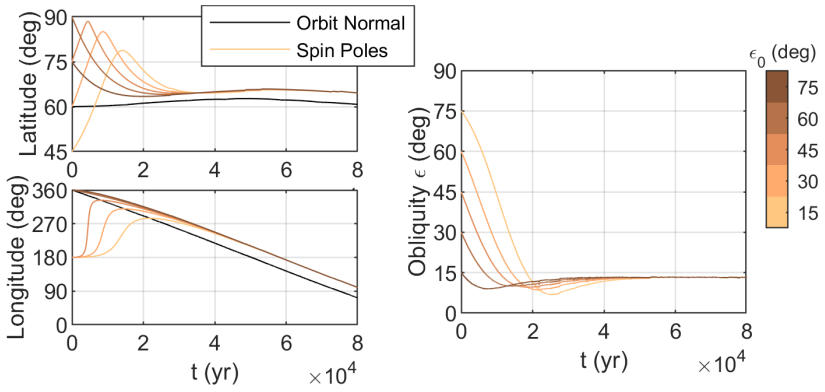


Figure 4.5 Latitude and longitude of spin poles and orbit normal under secular orbit and obliquity component torque.

Figure 4.5 shows an example of the propagation of the obliquity using the secular model of section 2.3.2 for the evolution of the orbit plane. In order to understand the effect of the torques we show the spin poles and orbit plane normal in latitude and longitude. We generate 5 different initial obliquities and propagate them for 80,000 years. We choose a significantly inclined orbit to illustrate the typical dynamical effects. The initial conditions are set as in Figure 4.4, except for $i$=30 deg and the physical parameters are $D$ =300 m, density $\rho$ =1,200 kg/m$^3$, and the YORP parameter was set as $C_\epsilon = -0.005$.

The orbit plane is roughly tracing a cone by drifting in longitude and small variations in latitude, which is consistent with the effects on $\Omega, i$. The spin poles are torqued into inside this cone, as shown by a latitude larger than that of the orbit plane. Then, it follows the orbit normal, as shown by the very similar rate of longitude. Regardless of the initial obliquity, we find the same terminal behavior: an offset from the 0 obliquity. Once we include planetary close encounters in the orbit propagation there will be stochastic changes in the orbit normal. All the physical parameters play a role in the offset from equilibrium, which we explore in the next section.

### 4.3.2 Obliquity Propagation

The physical parameters of the asteroid can be grouped in the following way. Equation 4.5 shows the $\propto R^3$ dependency of the torque. We can re-write our dynamics using equations 4.5 and

4.4:

$$I_z \omega \frac{d}{dt}(\hat{\omega}) = \left( \frac{\Phi R^3}{c} C_\epsilon \sin 2\epsilon \right) \hat{\omega}_{\perp 1} \tag{4.6}$$

If we take the norm of equation 4.6 we can rearrange the parameters of the problem into the rate of change of the spin pole $\dot{\hat{\omega}} = \| \frac{d}{dt}(\hat{\omega}) \|$:

$$\dot{\hat{\omega}} = \frac{\Phi R^3}{c I_z \omega} |C_\epsilon| \sin 2\epsilon \tag{4.7}$$

The dependency on the asteroid size can be more explicitly shown by expanding on the inertia. Assuming a spherical asteroid of a given radius and constant density:

$$I_z = \frac{2}{5} M R^2 = \rho \frac{8}{15} \pi R^5 \tag{4.8}$$

In addition, we compute the spin pole rate at $\sin 2\epsilon = 1$ such that it becomes:

$$\dot{\hat{\omega}} = \frac{15}{8\pi} \frac{\Phi}{c \rho R^2 \omega} |C_\epsilon| \tag{4.9}$$

which groups all the relevant parameters of the problem. The rate of change of the spin pole is larger the closer to the sun, less dense and/or smaller the asteroid, slower the rotation period, and more asymmetric. More importantly for the discussion, one can obtain the same dynamical behavior from a combination of these factors.

In Figure 4.6 we show the behavior of obliquity for $\dot{\hat{\omega}}$ of 3 different orders of magnitude and 2 different orbits and spin poles. We initially set the obliquity quite offset from the equilibrium of 0 degrees. The two orbits are initially set to $\Omega$=90 deg, $\varpi$=180 deg, $\sigma$=90 deg, and $a - e - i$ as in Table 4.1. We generate a Monte Carlo propagation of 100 samples using an uncertainty in $10^{-6}$ in all orbit elements in au, (-), radians.

Table 4.1 Initial conditions of the orbit histories for obliquity propagation

| Case | $a(au)$ | $e$ | $i$ (deg) |
|---|---|---|---|
| 1 | 1.1 | 0.15 | 15 |
| 2 | 1.4 | 0.30 | 5 |

Because of the stochastic variations in the orbit, we find that the obliquities become a statistical distribution. This distribution seems to converge to a distribution offset from 0 with a certain amplitude. The two orbit cases have similar initial obliquities far from equilibrium, but the time it takes to reach the terminal or steady state distributions changes significantly between the two examples. Given the same spin pole rate, this must be due to the difference in the orbits. The faster orbit normal (larger semi-major axis) causes a slower drift into the final offset distribution. The lower torque case also shows the oscillations that are predicted by the secular theory. Even if slowly drifted into a final distribution.

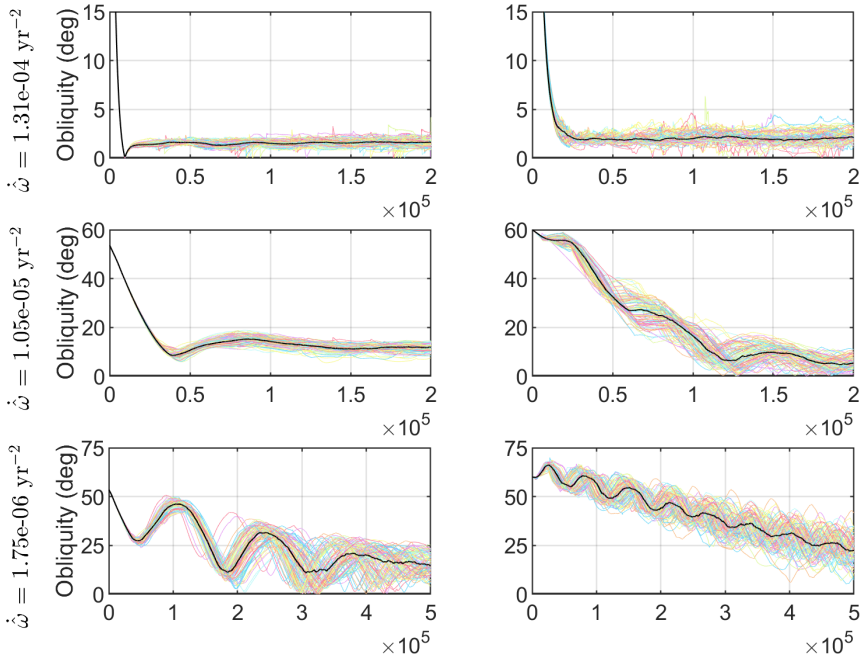


Figure 4.6 Obliquity propagation under different spin pole rates for two stochastic orbit Monte Carlo propagations. Left column shows Case 1, Right column shows Case 2.

## 4.4 Discussion

In order to better understand the dependency of the obliquity dynamics with these torques, we explore the influence of the spin pole rate parameter. In Figure 4.7 we sweep over $\dot{\hat{\omega}}$ for the same orbit elements cases of table 4.1. For each value of $\dot{\hat{\omega}}$ we propagate the obliquity for 20 randomly picked trajectories out of the N=100 particle Monte Carlo experiments. The reference time-scale for this analysis is 100,000 years, which is the same order of magnitude as the secular periods of the orbits. We run simulations between $\dot{\hat{\omega}} = 1 \cdot 10^{-3}$ yr$^{-2}$, which causes all the distribution to quickly converge to almost the equilibrium obliquity; to $\dot{\hat{\omega}} = 1 \cdot 10^{-7}$ yr$^{-2}$, which differs very little from the distributions without torques.

We show two different snapshots of the distributions, after 100,000 and 500,000 yr. For very small or very large $\dot{\hat{\omega}}$, the offsets from equilibrium are similar between the two snapshots. In the case of small $\dot{\hat{\omega}}$, there is a small movement of the mean of the distribution and a significant increase in the width. This increase is maintained at intermediate values of $\dot{\hat{\omega}}$, but there is a large change in the mean obliquity. This means that the timescales to equilibrium between $1 \cdot 10^{-5}$ and $1 \cdot 10^{-6}$ yr$^{-2}$ correspond to the simulation timescales of $\sim$100,000 years. In the case of larger $\dot{\hat{\omega}}$, the timescales are much faster, and by the 100,000 yr mark the distributions are already at the steady state offset, as the mean obliquity value does not change after 500,000 yr. The difference between snapshots is only an increase in the width in the distribution in the order of degrees. Here we also find a difference in the offsets from 0 between the two orbit simulations. Case 1, with a higher inclination, shows a larger offset from 0. The very large $\dot{\hat{\omega}}$ implies that the obliquity distribution collapses to 0. This is the extreme case for a general trend that the width of the distributions decreases significantly with $\dot{\hat{\omega}}$.

Note that for $C_\epsilon < 0$, the same analysis could be done around 180 deg. For the clarification of this discussion we chose initial obliquities closer to the equilibrium point of 0 obliquity. However, as shown in section 4.1, among the NEO population it is more common to find obliquities near 180 deg.

To put the magnitudes of $\dot{\hat{\omega}}$ in perspective, we can compare to these expected values for a few asteroids. If we include the results for 433 Eros, the computed $\dot{\hat{\omega}} = 5 \cdot 10^{-9}$ yr$^{-2}$. As expected, a tens of km-sized NEO is not expected to be under significant thermal torques. On the other hand, if we take the physical properties of 101955 Bennu, we compute $\dot{\hat{\omega}}$ somewhere between $3 \cdot 10^{-6} - 1 \cdot 10^{-5}$ yr$^{-2}$ for $C_\epsilon = 0.001 - 0.005$, which are typical values of this YORP coefficient [Golubov and Scheeres, 2019]. 101955 Bennu's current obliquity is of 177.6 deg, a typical offset form the neighboring obliquity configuration of 180 deg. This result is consistent with its lifetime of 1.75 million years according to the cratering history [Ballouz et al., 2020]. The physical properties of these comparisons are retrieved from NASA JPL's SBDB Lookup platform, $C_\epsilon$ from Golubov and Scheeres [2019].

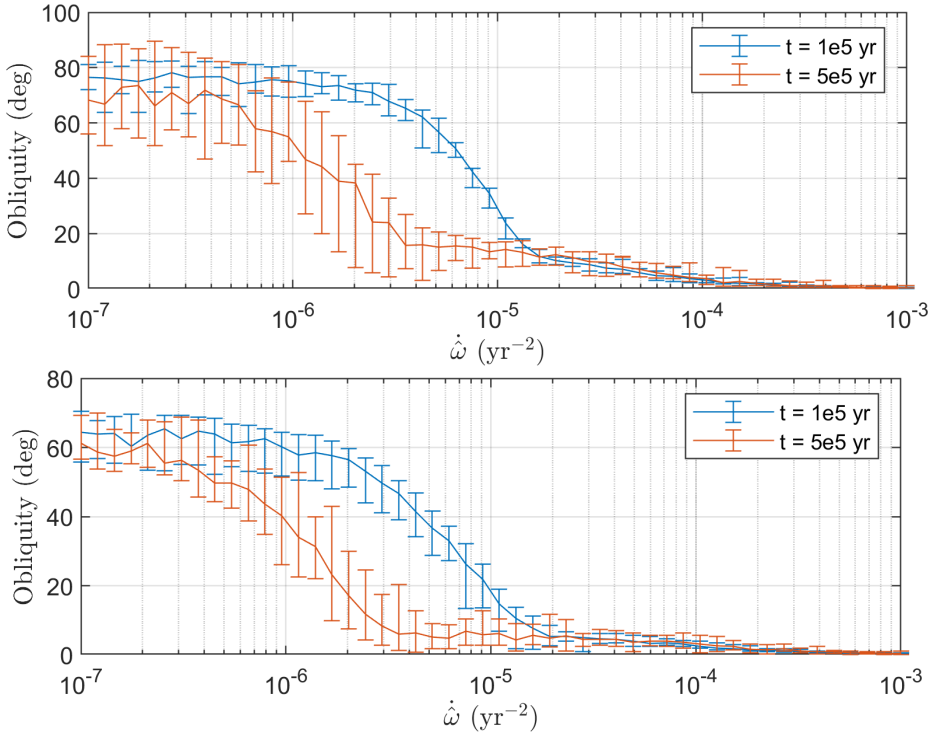


Figure 4.7 Distributions of obliquities at $t = 1 \cdot 10^5$ yr and $t = 5 \cdot 10^5$ yr as function of the spin pole rate $\dot{\hat{\omega}}$ for the two orbits. Top row shows Case 1, Bottom row shows Case 2.

The spin poles observed for near-Earth asteroids have a preference for the equilibrium obliquities predicted by YORP theory, but are not strongly clustered around these values. Full thermal and rotational modeling of the asteroid dynamics requires a large amount of measurements. We investigated the contribution of the evolution of the heliocentric orbit and show how in many cases it is not possible to maintain the equilibrium obliquities due to the oscillations of the orbital plane, due to secular effects and in the presence of planetary close encounters. In the observed population shown in Figure 4.2 there are bins around 60 and 120 deg of obliquity that could be explained by these oscillations in obliquity that increase the timescales to reach equilibrium.

# Chapter 5

# Hazard characterization by MOID propagation

## 5.1 Introduction

Asteroid impacts are one of the few natural disasters that can be prevented through human action. The main planetary defense efforts consist of observations, orbit determination and impact hazard assessment, and deflection/in-situ characterization. The near-Earth asteroid catalog is being completed by current and proposed surveys, providing new candidates of a future collision to study in more detail. In this chapter and chapter 6 we model the evolution of the MOID for impact hazard assessment, as a small MOID is required for a potential impact.

In 1998 the congress of the US requested NASA to detect and catalog 90% of the km-sized NEO population.[1] As of 2023-02-08, the catalog is around 95% complete, with an estimated population of $962^{+52}_{-56}$ [Granvik et al., 2018]. Impact monitoring systems estimate the orbits of newly discovered objects and compute any impact probabilities in future close encounters. Using the observational data available for a given object, the orbit is statistically estimated within an uncertainty region. This uncertainty region is efficiently sampled using various techniques to assess impact probabilities.

The first generation impact monitoring system relied on the Line of Variations technique [Milani et al., 2005], sampling a suitably chosen direction of the uncertainty region. More recently, Roa et al. [2021] describe a different approach that samples the full N-dimensional uncertainty

[1] More details on the historical efforts of the U.S. Government to track and mitigate asteroids were given in two parts of a hearing before the Committee on Science, Space and Technology of Congress in March 19, 2013 and April 10, 2013. Full hearing statements accessible at https://www.govinfo.gov/content/pkg/CHRG-113hhrg80552/pdf/CHRG-113hhrg80552.pdf

region and identifies virtual impactors by using the impact condition as an observable. This latter approach is used by JPL's Sentry-II system.[2]

In this chapter we investigate the potential impact risk over an order of magnitude larger timescales, in the next thousand years. To do this we review the two conditions required for an impact to occur [Valsecchi et al., 2003], and how the growth in orbit uncertainty affects them. The first one is that the Minimum Orbit Intersection Distance (MOID) has to be smaller than the combined radii of the two bodies, taking into account the gravitational focusing factor. This condition motivates the orbit condition for the definition of a Potentially Hazardous Asteroid (PHA): having an Earth MOID $< 0.05$ au [Bowell and Muinonen, 1994]. Similarly, the MOID can be used to rule out NEOs for further potential impact analysis. The MOID is found as a function of the orbit elements of the Earth and those of the NEO, but does not directly depend on the position along the orbit [Gronchi, 2005]. The uncertainty in these elements does not grow as fast as in mean anomaly, which allows us to propagate it confidently in longer timescales. Previous works studied the models required to propagate the MOID [Gronchi and Tardioli, 2013], including the applicability of the 3-body problem. In the presence of planetary encounters and complex long-term secular interactions, we must use numerical integration to propagate the orbits.

The second condition is on the timing of the flyby: the two bodies must be at the same time in the region in which their relative distance allows for a collision [Valsecchi et al., 2003]. Uncertainty in the asteroids position grows faster in the direction of motion, limiting the assessment of future impacts. After a few centuries the uncertainty in mean anomaly can cover the whole orbit. This phenomenon is used as an assumption of analytical theories of impact rates in timescales of millions of years [Öpik, 1951, Wetherill, 1967]. In this work we keep track of the uncertainty in mean anomaly and use this assumption when the MOID condition is met. Previous works combine these assumptions in hundreds of thousands of years timescales [Vokrouhlický et al., 2012, Pokorný and Vokrouhlický, 2013], using analytical models of the long-term dynamics. In these much longer timescales the uncertainty in NEO orbits grows large enough that lower fidelity models of the long-

[2] https://cneos.jpl.nasa.gov/sentry/

term dynamics provide good estimates of the frequency of close encounters, such as the methods in chapter 2. Thus, in the thousands of years timescales considered in this chapter, we propose the combination of the two conditions although we propagate the orbits of the NEOs numerically.

In this chapter we investigate the long-term MOID dynamics as a tool for long-term hazard characterization. In section 5.2 we provide insight of the orbital dynamics for km-sized NEOs. We propose an estimation of the probability of a deep encounter in section 5.2.3. Then, we inspect the km-sized population of NEOs. First, identifying the km-sized NEOs that are frequently in the neighborhood of Earth in section 5.3.1. Then, in section 5.3.2 we keep track of the uncertainty in mean anomalies during those low-MOID periods. The proposed metric allows us to rank the km-sized NEO population, highlighting a few km-sized NEOs for further detailed analysis in section 5.4. In section 5.5 we inspect the PHA population and highlight the evolution of the MOID for this population that already has a small MOID. We conclude with the main findings for these two populations of NEOs.

## 5.2 Long-term NEO Hazard characterization

In this section we describe the tools and methods used to analyze the long-term dynamics of the km-sized NEO population and the estimation of their potential impact hazard. The MOID time histories are obtained following the propagation of the orbit. Hence, we first describe the orbit propagator as motivated by the NEO long-term dynamics and then the MOID algorithm and dynamics. Last, we introduce the long-term collision hazard metric that is used to rank the selected group of near-Earth objects.

### 5.2.1 Orbit propagation

The orbits of the NEOs are propagated using the JPL small-body integrator which is based on an N-body model that includes Sun, planets, Pluto, Moon and small-body perturbers [Farnocchia et al., 2015]. When the Yarkovsky effect was detected from astrometric data [Farnocchia et al., 2013b], we added it to the force model. The ephemeris models used in the integration are DE441

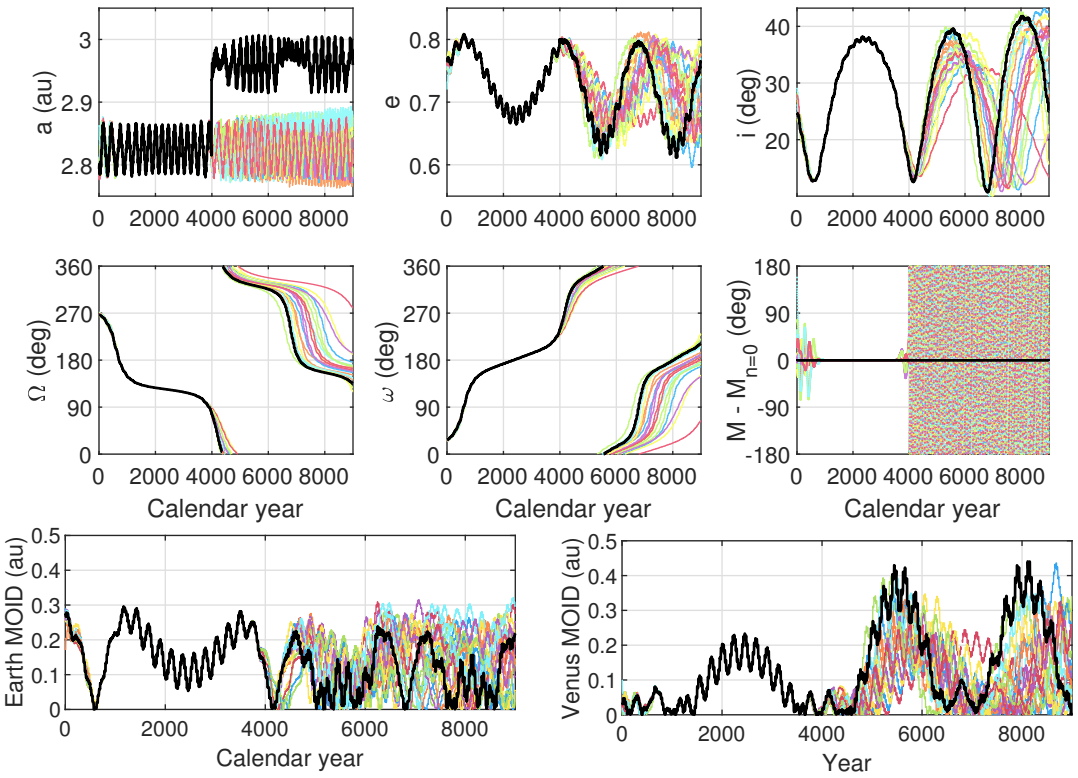


Figure 5.1 Numerical propagation of the orbit of 2015 FP332, a km-sized NEO.

[Park et al., 2021] for the planets and SB441-N16 for the largest main-belt bodies.[3]

Figure 5.1 shows the propagation of the orbit of 2015 FP332, which reveals the relevant dynamical effects to the long-term dynamics of near-Earth objects. The trajectories are shown using the Keplerian elements semi-major axis, eccentricity, inclination, longitude of the ascending node, argument of perihelion and mean anomaly with respect to the nominal propagation. Individual Monte-Carlo runs (N=21) are shown in colors, the nominal trajectory is shown in a black line. The bottom rows show the propagation of Earth and Venus MOID. 2015 FP332 is in a Lidov-Kozai cycle [Lidov, 1962, Kozai, 1962], in which periods of high eccentricity are exchanged with periods of high inclination. In this case, both longitude of the node and argument of perihelion drift secularly.

[3] Available at: `ftp://ssd.jpl.nasa.gov/pub//eph/small_bodies/asteroids_de441/SB441_IOM392R-21-005_perturbers.pdf`

Planetary encounters can cause the exponential growth of the distance between initially neighboring trajectories, a necessary condition for chaos [Tancredi, 1998]. Neighboring trajectories of near-Earth asteroids can diverge in timescales ranging from decades, such as 99942 Apophis [Farnocchia et al., 2013a]; to hundreds of years, such as 29075 (1950 DA) [Farnocchia and Chesley, 2014]; to tens of thousands of years, such as 433 Eros [Michel et al., 1996a]. In this process the linear approximation of the state uncertainty can quickly become inaccurate.

Figure 5.1 shows the propagation of the multiple samples or virtual asteroids of the orbit of 2015 FP332. In this example, the nominal trajectory of 2015 FP332 experiences a very close Venus encounter that causes the rapid increase in semi-major axis. Once each initially neighboring virtual asteroid diverges to a different trajectory it experiences a unique sequence of close encounters. This effect motivates the use of the MOID to estimate long-term probabilities of collision. The resulting dynamics under these encounters are very nonlinear, and the orbits of near-Earth objects in these timescales become stochastic. For this reason, we sample the uncertainty in the orbits of NEOs and propagate them in a Monte Carlo simulation. The detection of potential impactors of small probabilities is out of the scope of this work, in which the main metric of interest is the MOID. For this reason we run a limited number of Monte Carlo samples (N=21), which allows us to distinguish the main dynamical effects as well as the uncertainty in mean anomaly.

The presence of close encounters is expected if the near-Earth object has a small MOID with any of the planets. Thus, tracking the evolution of the MOID is not only relevant for the evaluation of the probability of collision with Earth but to understand when the dynamics are subject to nonlinear stochastic variations. The evolution of the orbit of 2015 FP332 in Figure 5.1 shows the effect of a low-MOID period in the long-term prediction. A Venus low-MOID enables close approaches that cause the rapid expansion of the distribution of orbits and mean anomaly to become unknown.

### 5.2.2 MOID algorithm and dynamics

The MOID is the result of the optimization of the relative distance between two bodies over their respective fast angles. There are multiple algorithms to compute the MOID in the literature, including analytical methods [Gronchi, 2005] and numerical methods such as Wiśniowski and Rickman [2013] or Hedo et al. [2018], which is used in this work. The MOID, a function of the osculating orbit elements, is then computed when post-processing the numerically integrated trajectory.

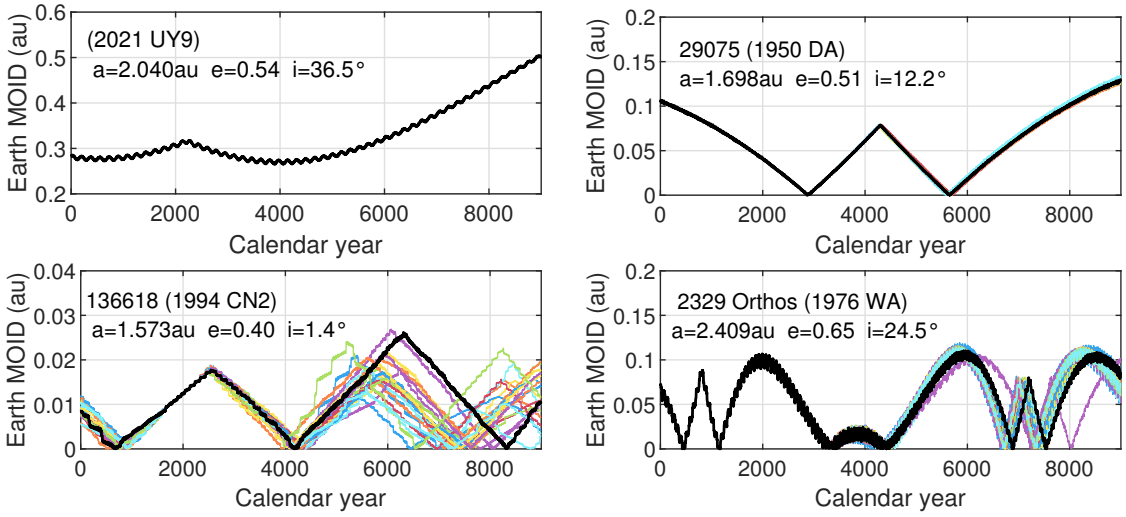


Figure 5.2 Propagation of the Earth MOID of a few selected examples of km-sized near-Earth objects.

Depending on the dynamical effects on the asteroid described in the previous section we find a variety of MOID long-term dynamics trajectories. Figure 5.2 shows a few examples of the dynamics of the propagation of the MOID for four km-sized NEOs, the 21 Monte Carlo simulations in colors and the nominal in black, continuous lines. 2021 UY9 represents the simplest case, in which the MOID does not become small throughout the simulation time therefore making Earth impacts impossible. The uncertainty in the orbit of 2021 UY9 remains small throughout the propagation. The case of 29075 (1950 DA) is the very common case for NEOs, in which the MOID drifts secularly until a future zero crossing that lasts a short period of time, of about a century. The example of 136618 (1994 CN2) is similar to the case of 2015 FP332 in Figure 5.1, in which the date in which

the MOID becomes small for the first time is uncertain. After a low-MOID period the trajectory becomes more uncertain. The last example, 2329 Orthos (1976 WA), illustrates the scenario of an extended period of time with a low Earth MOID. This is caused by the combination of two effects, a large amplitude of short-period oscillations and a favorable phasing of the secular cycle.

The examples of Figure 5.2 are also representative of the growth in uncertainty of the MOID. In the two top cases the uncertainty remains small for thousands of years. The km-sized NEA population have well defined orbits and their Earth MOIDs remain well known for hundreds of years. Previous works focus on mapping the orbit covariance into a confidence region of the MOID [Gronchi and Tommei, 2007]. However, the uncertainty in the orbit can become far from Gaussian in long-term orbit propagations. Thus, we use statistics of the Monte Carlo propagation as indicators of the spread of the distribution as well as the confidence in our predictions.

### 5.2.3 Long-term impact probability estimation

The complexity in long-term MOID dynamics that we showed in the previous section motivates the development of a systematic method to quantify the long-term Earth impact hazard of NEOs. We propose a novel metric to characterize the potential impact hazard that consists in an estimated probability of collision between a planet and a NEO. The probability of collision is a problem primarily studied in two major timescales. The fundamental problem of impact hazard assumes the position of the asteroid within its orbit is reasonably well determined and it is possible to precisely determine the geometry of the subsequent close encounters. In the case of potentially hazardous asteroids, this analysis can typically be completed for one or two centuries [Chamberlin et al., 2001, Roa et al., 2021]. In these timescales the uncertainty in the orbit of many NEOs starts to grow large enough that the position within the orbit can become unknown. This effect motivates the statistical assumption of a uniformly distributed mean anomaly.

Traditional impact probability theories assume that the orbit elements of the two objects involved are constant and have one intersection point [Öpik, 1951, Wetherill, 1967]. Then, the probability depends on the timing of the orbits, which is when the mean anomalies are assumed

uniformly distributed. This timing probability, here $P_{MA}$, is the probability that both bodies are in the right time at the right place, i.e., the range of mean anomalies that corresponds to a collision or flyby within a small distance.

There are a few options for the timing probability in the literature. In the most simplified case, we can assume the planet's orbit to be circular with Öpik's formula [Öpik, 1951], in which the probability is function of the Keplerian elements of the asteroid a-e-i. Wetherill [1967] then derived an expression for an elliptic orbit of the planet, with the problem of being singular at zero inclination. In this work we use this expression as re-derived recently in JeongAhn and Malhotra [2017] for regular non-tangential encounters. In particular, we use the extended expression for the case in which the two objects do not exactly intersect. That means that the MOID is a positive value between 0 and the distance threshold for the close encounters of interest $d$. Thus, the probability that two objects have a close encounter with closest approach distance smaller than $d$ is:

$$P_{MA} = \frac{2Ud}{T_p T_{NEO} |\mathbf{v_p} \times \mathbf{v_{NEO}}|} \sqrt{1 - \frac{MOID^2}{d^2}} \tag{5.1}$$

where $\mathbf{v_p}$ and $\mathbf{v_{NEO}}$ are the velocities of the planet and the asteroid at the point that defines the MOID, $U$ is the relative velocity at the same point, and $T_p, T_{NEO}$ are the respective orbit periods. The square root term of equation 5.1 adjusts the probability for a non-zero MOID. If MOID $> d$, the probability is assumed to be zero. This expression can be averaged for a MOID uniformly distributed between 0 and $d$. However, in this work we do not need to make this assumption as we keep track of the MOID throughout our long-term propagation and the distribution can be far from uniform in the range 0 <MOID$\leq d$.

Once we allow the orbit of the NEO to be time-varying, we can obtain the probability of collision as the combination of two terms: the probability that there is an intersection between the planet and near-Earth object and $P_{MA}$. If we investigate a potential Earth collision, the condition is that the Earth MOID is smaller than the combined radii of the two bodies considering gravitational focusing as required. The gravitational focusing factor virtually extends the radius of the planet to

account for trajectories that lead to a collision due to the planet's gravity, and is a function of the incoming velocity of the asteroid $V_\infty$ and the mass and radius of the planet $M_p, R_p$:

$$\gamma = \sqrt{1 + \frac{2GM_p}{R_p V_\infty^2}} \tag{5.2}$$

This approach has been used in the past to obtain the probability of collision for asteroids under the Lidov-Kozai cycle [Vokrouhlický et al., 2012, Pokorný and Vokrouhlický, 2013]. In that case, the generalized probability of collision is obtained as the sum over all the crossing configurations (noted with *) of the fraction of time that the NEO spends withing the distance threshold times the timing probability:

$$P = \sum_{*} \left( \frac{\Delta t_{MOID<d}}{T_{sec}} \right)^{*} P_{MA}(d, K_p^*, K_{NEO}^*) \tag{5.3}$$

where $K_P, K_{NEO}$ are the Keplerian elements of the planet and the NEO and $\Delta t_{MOID<d}$ is the amount of time that the NEO spends within the distance threshold $d$. Vokrouhlický et al. [2012] and [Pokorný and Vokrouhlický, 2013] model the long-term asteroid dynamics with an analytical solution of the Lidov-Kozai cycle of the Jupiter perturbation, which defines the secular period $T_{sec}$ as the Lidov-Kozai period. As a result, the fraction $\Delta t$ and intersection configurations are computed analytically. As we show in the previous section, defining the times in which the MOID is small can be a complex problem under a wide range of dynamical contributions. In this work we propagate the orbit numerically to find the low-MOID periods. Because there is not a small discrete number of crossings along the long-term dynamics of the NEO, we estimate the probability as the average throughout the propagation time $T$ using equation 5.4.

$$P = \frac{1}{T} \int_T \kappa P_{MA}(d, K_p, K_{NEO}) dt \tag{5.4}$$

This integral is computed numerically using the numerically integrated trajectories. The factor $\kappa$ is introduced so we can null the contribution of the trajectory in which the position of the object is deterministic within its orbit, i.e., when the uncertainty in mean anomaly is small. $\kappa$ is

set to 0 before the first date in which we find that the standard deviation in mean anomalies is larger than 10 degrees, and set to 1 elsewhere. This distinction allows us to rule out the associated risk of objects that currently have a very low MOID but their position is properly constrained for the duration of their visit to the planet's vicinity. In addition, we check the close encounters that were recorded in the propagation before we can use the analytical expression for $P_{MA}$ in equation 5.1.

## 5.3 KM-sized NEO population long-term characterization

We analyze the potential impact hazard of the km-sized NEO population in the next millennium. Using the very low-MOID necessary condition for a potential collision, we can rule out the collision hazard when this condition is not met. Then, considering the statistical evolution of the mean anomalies, we rank this group of NEOs depending on their long-term implicit impact hazard.

### 5.3.1 NEOs frequently in Low-MOID regions

The orbits of the known km-sized NEO population are propagated starting from their orbit solutions in JPL's Small-body Database as of 2022-09-15.[4] For each NEO we find the first date at which a low-MOID period is found between all of the Monte Carlo samples, with a threshold defined as MOID $< 0.01$ au (235 Earth Radii or 3.89 Lunar Distances). At this threshold, the incoming velocity $V_\infty$ required for a collision is of 0.05 km s$^{-1}$ or less, from solving equation 5.2. From a statistical point of view, this relative velocity is extremely unlikely[Farnocchia and Chodas, 2021, Harris and Chodas, 2021].

The first question we answer is how many km-sized NEOs currently have a MOID $< 0.01$ au, and how will this number evolve in the next 1000 years. As of the time in which the JPL's SBDB was queried, there are 40 NEOs that fulfill this condition. The evolution of this estimated number of NEOs is shown in Figure 5.3. The minimum number of NEOs is estimated by NEOs in which there was an agreement between all Monte Carlo runs. The maximum number of NEOs is

[4] Small-body Database available for query at: `ssd.jpl.nasa.gov/tools/sbdb_query.html`

estimated by at least one Monte Carlo run fulfilling the low-MOID condition. As the uncertainty in the orbits of the NEOs grows into the future, only some of the MC samples may have MOID $< 0.01$ au. This phenomenon is shown in more detail in Figure 5.4, which shows the estimated range of km-sized NEOs with MOID $< 0.01$ au based in the Monte Carlo samples. The uncertainty remains very small ($\pm 1$ body) throughout the next 500 years. By the end of the millennium, this number is in the range of 26-72 km-sized NEOs. As mentioned earlier, none of these objects pose a collision threat to Earth in the next 100 years.

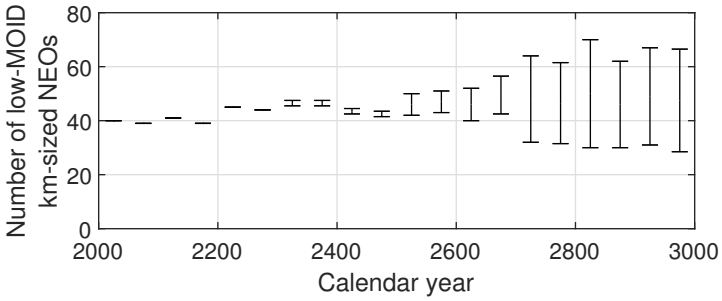


Figure 5.3 Number of km-sized NEOs that present an Earth MOID <0.01 au throughout the next 1000 years.

Individual results of the MOID propagation are shown in Figure 5.4. We sorted the km-sized NEOs by the date in which they meet the MOID $< 0.01$ au condition. The color code indicates the number of Monte-Carlo samples that show a MOID $< 0.01$ au at the given date. Black means an agreement between all Monte Carlo runs to show a low-MOID. The NEOs are sorted by the first date in which they meet the MOID $< 0.01$ au condition. As defined by the length of their low-MOID periods, we show NEOs that are expected to be continuously in the vicinity of Earth as opposite to the ones that are for a brief period of time. We observe that even if the number of NEOs will never exceed an average value of 40-45 NEOs, the total number of unique low-MOID NEOs in the next 1000 years is of almost 150.

We list the km-sized NEOs that frequently experience MOID $< 0.01$ au in Table 5.3.1 based in the fraction of the next 1000 years that they meet the condition. The time fraction indicates the average fraction of time with MOID $< 0.01$ au among the Monte Carlo experiments. The first date of standard deviation in Mean Anomaly $> 10^\circ$ is shown with initial orbit elements at the ephemeris


Figure 5.4 Km-sized NEOs that meet the MOID $< 0.01$ au condition in the next 1000 years.

retrieval date, 2022-09-15. $V_\infty$ is the relative velocity at the first time that MOID $< 1$ LD of the nominal solution. Their implicit probability of collision is assessed in the next section. There are 4 objects whose MOID remains lower than 0.01 au throughout this millennium: 7482 (1994 PC1), 68950 (2002 QF15), 164121 (2003 YT1), 144332 (2004 DV24). In the second and third case, the mean anomaly remains well defined throughout the millennium.

The propagation of the MOID of a few of the top-ranked NEOs is shown in Figure 5.5, as shown in Table 5.3.1. Individual Monte-Carlo runs are shown in colors, black continuous line shows the nominal trajectory. The dashed red line indicates the first date in which the standard deviation

in mean anomaly was found greater than 10 degrees, which does not happen for 68950 (2002 QF15). Most remarkably, we can see how low the MOID of 7482 (1994 PC1) persists throughout the next 1000 years. In 68950 (2002 QF15) and 164121 (2003 YT1) we observe a secular drift in the MOID. In the case of 68950 (2002 QF15), this secular drift predicts a near-zero MOID around year 2500. In the case of 164121 (2003 YT1), the MOID is increasing at a relatively slow rate. The last example, 143651 (2003 QO104), shows a large amplitude of the MOID around zero, which motivates additional analysis of the long-term hazard.

Table 5.1 10 km-sized NEOs with the largest fraction of time with low MOID over the next 1000.

| NEO | $\Delta t/T$ | $T_{S>10^\circ}$ | a (au) | e | i (deg) | $V_\infty$ (km s$^{-1}$) |
|---|---|---|---|---|---|---|
| 7482 (1994 PC1) | 1.000 | 2541 | 1.349 | 0.330 | 33.47 | 19.68 |
| 68950 (2002 QF15) | 1.000 | 3288 | 1.057 | 0.344 | 25.15 | 16.06 |
| 144332 (2004 DV24) | 1.000 | 3285 | 1.423 | 0.290 | 55.90 | 29.83 |
| 164121 (2003 YT1) | 1.000 | 2341 | 1.110 | 0.292 | 44.06 | 23.71 |
| 143651 (2003 QO104) | 0.945 | 2297 | 2.136 | 0.524 | 11.61 | 9.72 |
| 4179 Toutatis (1989 AC) | 0.927 | 2516 | 2.545 | 0.625 | 0.45 | 12.19 |
| 314082 Dryope (2005 CZ36) | 0.750 | 2352 | 2.238 | 0.575 | 16.14 | 14.05 |
| 86819 (2000 GK137) | 0.744 | 2565 | 1.996 | 0.506 | 10.06 | 10.07 |
| 385343 (2002 LV) | 0.740 | 2960 | 2.315 | 0.605 | 29.53 | 20.14 |
| 177614 (2004 HK33) | 0.702 | 3507 | 1.888 | 0.521 | 5.44 | 11.37 |

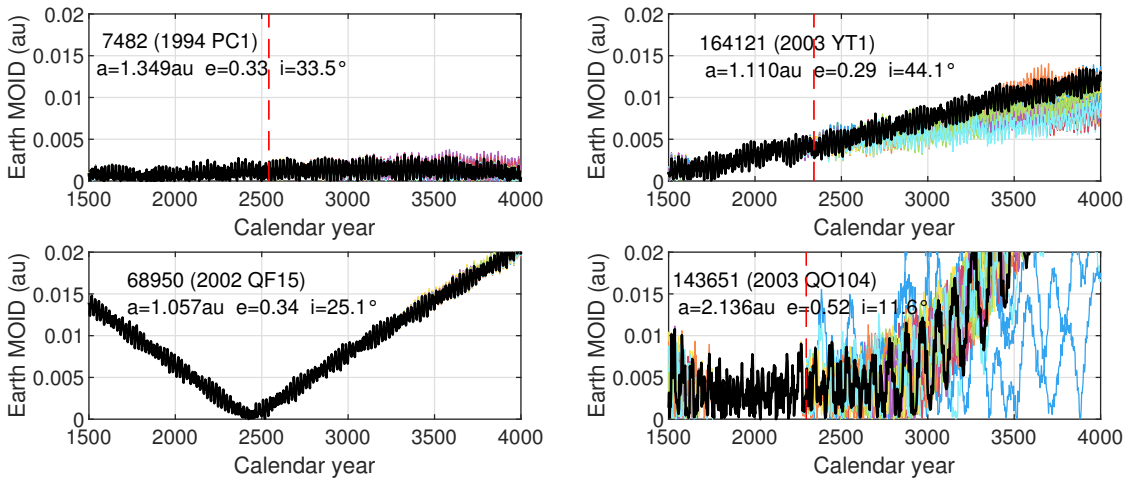


Figure 5.5 Propagation of the Earth MOID of km-sized NEOs with a low-MOID for a large fraction of the next 1000 years.

### 5.3.2 Upcoming hazardous km-sized NEOs

In the previous section we inspected the necessary condition for very close encounters to occur: a MOID $< 0.01$ au. The next step is to estimate the collision probability by making assumptions on their mean anomalies. The method to compute this timing probability once the MOID is low was described in section 5.2.3. To study the potential impact hazard we set a smaller close approach threshold (1 LD) and take into account the deterministic parts of the NEO position during the orbit propagation. In addition, we study the list of close approaches generated in the Monte Carlo experiment to validate our predictions.

The analytical expressions for the probability of collision assume uniformly distributed mean anomalies of the bodies. The initial conditions of the propagation start from a well defined mean anomaly of the NEOs. Thus, we need to track the evolution of the uncertainty in mean anomaly to know when we can start using the analytical estimates. Using our Monte Carlo experiments we compute the standard deviation in mean anomaly separation from the nominal trajectory.

We propagate the orbits of the km-sized NEO population for 1000 years and study when the MOID is smaller than a Lunar Distance (1 LD). When the standard deviation in mean anomaly is large, we estimate the probability of close encounters. In Figure 5.6 we list the km-sized NEOs showing the dates in which we found a low-MOID and sorted by their estimated probability of close encounters. The low-MOID regions are color coded with the standard deviation in mean anomaly S(MA), shown only in dates in which MOID $< 0.01$ au. The combination of this information highlights the future periods of time in which the position of the NEOs is unknown.

Among the 40 km-sized NEOs currently with an Earth MOID $< 0.01$ au, we find that their mean anomalies remain well defined typically for at least 200 years, and in some cases for thousands of years. On the other hand, there are a few examples of growth in mean anomaly uncertainty after 2200, such as 35396 (1997 XF11). Because the MOID becomes greater than 1 LD by the time the uncertainty in mean anomaly is large, the estimated probability for this NEO is zero.

The objects with the highest estimated probability are shown in Figure 5.6 and listed in Table

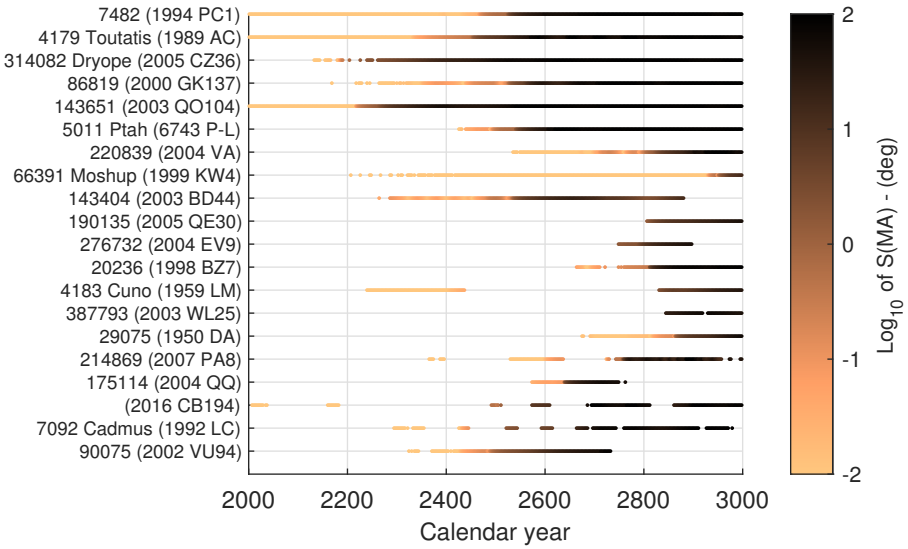


Figure 5.6 Km-sized NEOs with non-zero estimated probability of encounters closer than 1 LD.

5.3.2. In this table the time fraction indicates the average fraction of time with MOID $<$ 1 LD among the Monte Carlo experiments, and $V_\infty$ is the relative velocity at the first time that MOID $<$ 1 LD of the nominal solution. The asteroid with the largest estimated probability of a deep close encounter is 7482 (1994 PC1). This result is to be expected, as in section 5.3.1 and Figure 5.5 we show that 7482 (1991 PC1) has a continuous low MOID. In this analysis we find that 7482 spends about 98% of this millennium with an Earth MOID <1 LD. During this unusually lasting MOID <1 LD period the position is well determined until approximately year 2500.

The propagation of the MOID for the other km-sized NEOs on top of the list is shown in Figure 5.7. Close encounters are indicated with circles in colors and close encounters of the nominal trajectory are shown as vertical black nodes. The encounters of closest approach distance $< 1LD$ (0.0026 au) are highlighted with a larger red circle. We find that either the Earth MOID of these bodies is secularly drifting to zero, or that the current low-MOID oscillates around zero for a longer period of time. The latter case was observed for 7482 (1994 PC1), but additionally 4179 Toutatis (1989 AC) and 314082 Dryope (2005 CZ36) are in similar situations. Figure 5.7 shows that deep encounters are expected for these bodies, both in a low-MOID format and as the result of the Monte Carlo experiment.

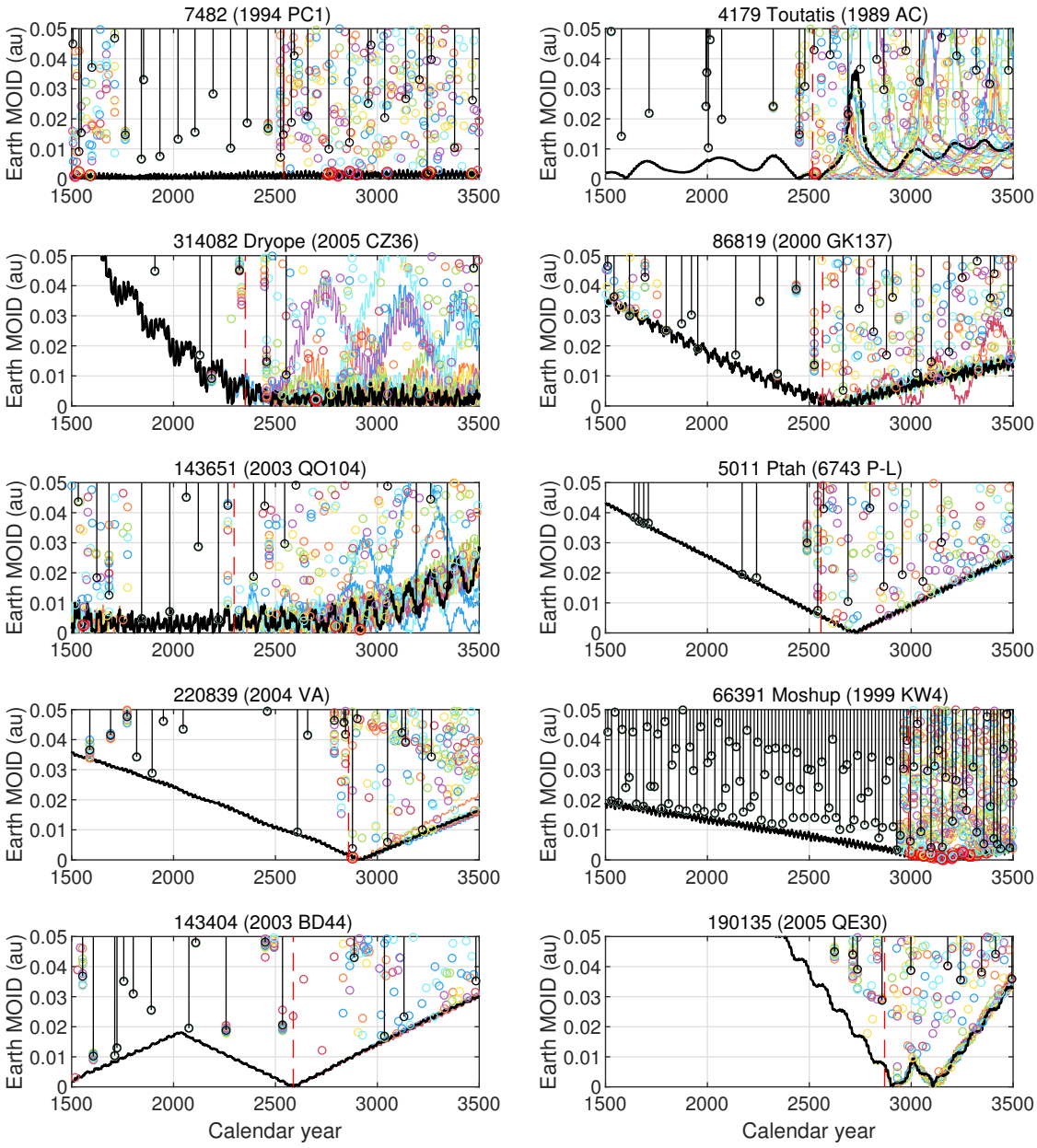


Figure 5.7 Propagation of the Earth MOID of km-sized NEOs with a non-zero probability of having an encounter closer than 1 LD by year 3000.

Table 5.2 28 km-sized NEOs with non-zero estimated probability of a deep encounter ($d_{CA}$ <1 LD) in the next 1000 years.

| NEO | P($yr^{-1}$) | $\Delta t/T$ | $t_{S>10^\circ}$ | a (au) | e | i (deg) | $V_\infty$ ($kms^{-1}$) |
|---|---|---|---|---|---|---|---|
| 7482 (1994 PC1) | 1.51e-04 | 0.978 | 2541 | 1.349 | 0.330 | 33.47 | 19.68 |
| 4179 Toutatis | 5.19e-05 | 0.336 | 2516 | 2.545 | 0.625 | 0.45 | 12.19 |
| 314082 Dryope | 4.88e-05 | 0.312 | 2371 | 2.238 | 0.575 | 16.14 | 14.05 |
| 86819 (2000 GK137) | 4.44e-05 | 0.229 | 2563 | 1.996 | 0.506 | 10.06 | 10.07 |
| 143651 (2003 QO104) | 3.84e-05 | 0.306 | 2308 | 2.136 | 0.524 | 11.61 | 9.72 |
| 5011 Ptah | 3.68e-05 | 0.152 | 2626 | 1.636 | 0.500 | 7.41 | 12.50 |
| 220839 (2004 VA) | 3.05e-05 | 0.172 | 2856 | 1.902 | 0.595 | 3.69 | 14.88 |
| 66391 Moshup | 1.59e-05 | 0.045 | 2987 | 0.642 | 0.688 | 38.88 | 21.08 |
| 143404 (2003 BD44) | 1.45e-05 | 0.153 | 2587 | 1.968 | 0.606 | 2.66 | 15.93 |
| 190135 (2005 QE30) | 1.43e-05 | 0.074 | 2899 | 2.019 | 0.688 | 6.22 | 19.14 |
| 276732 (2004 EV9) | 1.07e-05 | 0.038 | 2809 | 1.471 | 0.781 | 40.83 | 32.09 |
| 20236 (1998 BZ7) | 1.04e-05 | 0.087 | 2817 | 2.036 | 0.559 | 6.50 | 12.52 |
| 4183 Cuno | 7.37e-06 | 0.123 | 2913 | 1.982 | 0.636 | 6.67 | 17.01 |
| 387793 (2003 WL25) | 4.46e-06 | 0.030 | 2880 | 2.395 | 0.742 | 23.76 | 25.34 |
| 29075 (1950 DA) | 4.22e-06 | 0.104 | 2913 | 1.698 | 0.508 | 12.17 | 14.09 |
| 214869 (2007 PA8) | 3.43e-06 | 0.091 | 2762 | 2.848 | 0.653 | 2.00 | 12.46 |
| 175114 (2004 QQ) | 2.30e-06 | 0.045 | 2648 | 2.249 | 0.664 | 5.72 | 19.74 |
| (2016 CB194) | 2.27e-06 | 0.039 | 2897 | 2.512 | 0.632 | 9.88 | 12.81 |
| 7092 Cadmus | 1.99e-06 | 0.046 | 2680 | 2.542 | 0.695 | 17.77 | 19.74 |
| 90075 (2002 VU94) | 1.95e-06 | 0.082 | 2606 | 2.134 | 0.576 | 8.91 | 12.81 |
| (2019 HC) | 1.78e-06 | 0.015 | 2883 | 2.670 | 0.551 | 35.32 | 19.48 |
| 322966 (2002 KF4) | 1.64e-06 | 0.022 | 2960 | 2.903 | 0.577 | 37.02 | 19.43 |
| 5143 Heracles | 1.38e-06 | 0.032 | 2998 | 1.834 | 0.772 | 9.03 | 25.78 |
| 529718 (2010 KY127) | 1.32e-06 | 0.011 | 2908 | 2.489 | 0.883 | 60.84 | 39.67 |
| 508997 (2005 FL4) | 1.07e-06 | 0.012 | 2823 | 2.651 | 0.721 | 28.43 | 24.40 |
| (1999 XS35) | 5.39e-07 | 0.148 | 2409 | 17.780 | 0.948 | 19.62 | 18.28 |
| 248590 (2006 CS) | 5.34e-07 | 0.005 | 2617 | 2.914 | 0.697 | 52.31 | 31.61 |
| 1620 Geographos | 4.47e-07 | 0.002 | 2861 | 1.246 | 0.335 | 13.34 | 11.88 |

The fact that the position is well determined allows us to determine the geometry of the subsequent close encounters, until the uncertainty grows too large. This assumption leaves a brief period of time between a very well constrained position and the range of validity of the uniformly distributed mean anomaly assumption. For this reason we check if there were actually such very close encounters among the low-MOID NEOs that we found earlier. In general, no close encounters within the Lunar Distance were found in the deterministic part of the trajectories.

There are a few exceptions that should be mentioned: 4179 Toutatis (1989 AC), 220839 (2004 VA) (Both in Figure 5.7), 20236 (1998 BZ7), 214869 (2007 PA8) and 175114 (2004 QQ) experience close encounters right before or right after the date in which $S(\mathrm{MA}) > 10^{\circ}$. In all of these cases, the MOID tends to zero around the dates in which a deep encounter is expected. In some cases, uncertainty in the position grows largely due to preceding close encounters. In general, we find that the Monte Carlo experiment agrees in finding deep encounters. Thus, the current method is successful in identifying their potential for very deep encounters within the next millennium.

## 5.4 Individual KM-sized NEOs Hazard Analyses

In this section we describe in more detail the hazardous nature of a few km-sized NEOs that were previously analyzed. We show the evolution of the MOID as well as the recorded track of close encounters in Figures 5.8-5.12. In addition, we show the sequence of close encounters that precedes the growth in uncertainty and limits the accuracy of the prediction of the position of the NEO. We study their orbital dynamics to provide context of the MOID evolution using the Keplerian elements semi-major axis, eccentricity, inclination, longitude of the ascending node, argument of perihelion and mean anomaly with respect to the nominal propagation. As shown earlier, individual Monte-Carlo runs (N=21) are shown in colors, the nominal trajectory is shown in a continuous black line.

### 5.4.1 Asteroid 7482 (1994 PC1)

7482 (1994 PC1) has been highlighted in every section of this work because of its remarkable MOID evolution. Its Earth MOID is currently $6.09 \cdot 10^{-4}$ au (0.237 LD), has been near zero for centuries and will remain very low for at least another 1000 years as shown in section 5.3.1. This condition is the reason why it is ranked as the most hazardous NEO in the list of Table 5.3.2.

The orbit elements of 7482 (1994 PC1) are shown for reference in figure 5.8. During the period in which the Earth MOID remains small there are close encounters that cause significant variations semi-major axis and eccentricity. However, arguments of node and perihelion follow a

secular drift. In its current orbit within the inner solar system, there is not a large amplitude of short-period oscillations that could disperse the distributions further. However, it is important to highlight that after 500 years the mean anomalies become uncertain.

Figure 5.8 shows the sequence of close encounters that are recorded in the Monte Carlo numerical propagation. It appears that the uncertainty in the encounter of 2525 is large enough that the range of possible closest approach distances is between 0 and 0.04 au. Right after the 2525 encounter the standard deviation in mean anomaly increases beyond 10 degrees, and we start estimating its probability of collision using the methods of section 5.2.3. Encounters below the Lunar Distance were found after this period, which is consistent with the higher probability that we previously estimated.

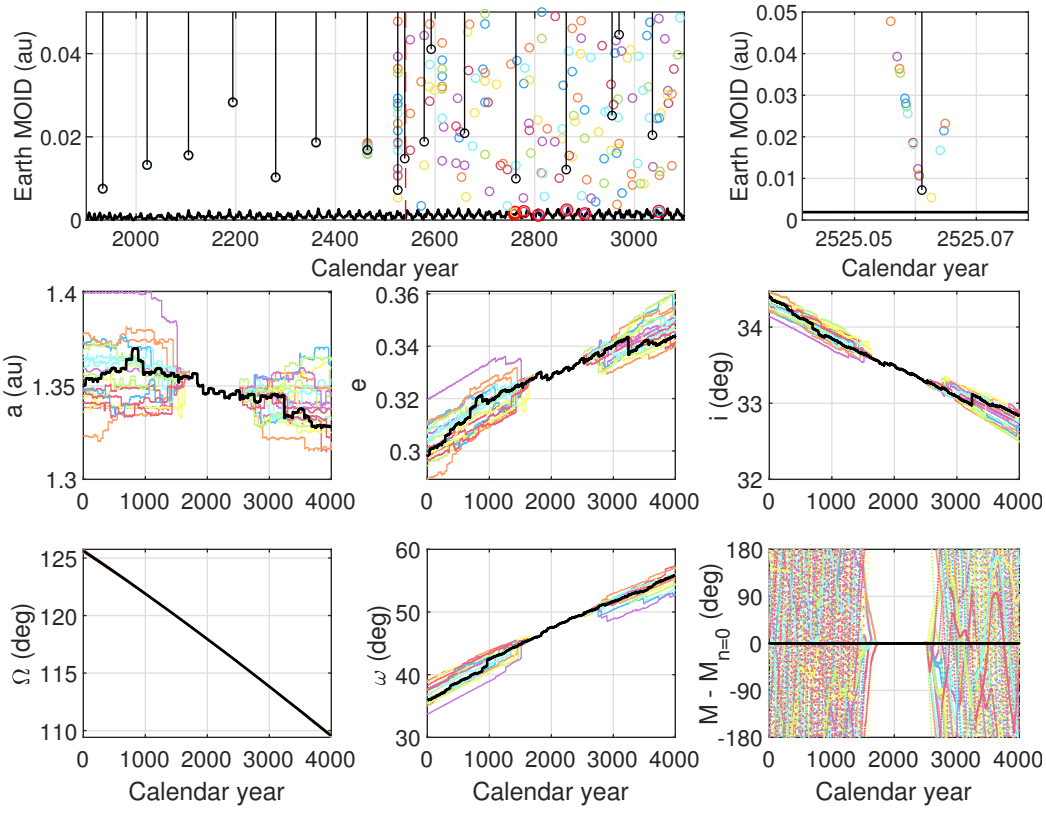


Figure 5.8 Earth close encounters and orbit elements of 7482 (1994 PC1).

### 5.4.2 Asteroid 143651 (2003 QO104)

The km-sized NEO with the shortest deterministic horizon is 143651 (2003 QO104), which was also previously introduced in Figure 5.6. The orbit solution of 143651 (2003 QO104) has an observation arc of decades, including light-curve observations [Birtwhistle, 2009] and radar astrometry [Warner et al., 2009]. Thus, we believe that the rapid increase in uncertainty is a dynamical effect of its orbit.

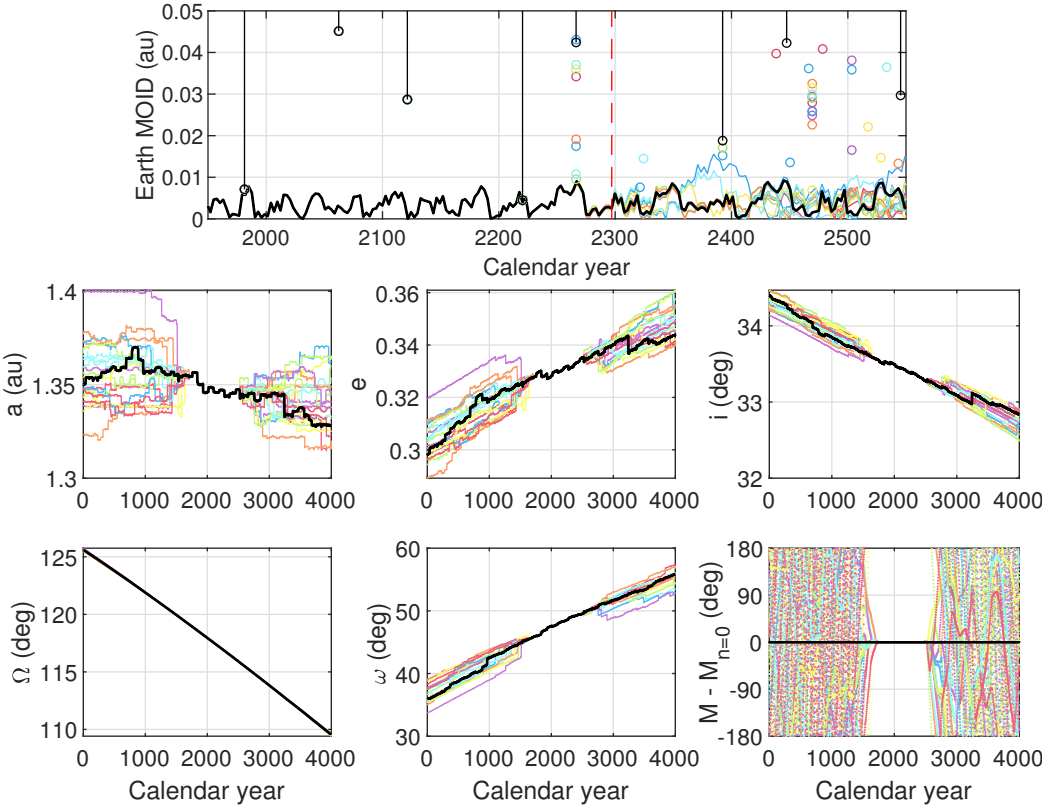


Figure 5.9 Earth close encounters and orbit elements of 143651 (2003 QO104).

Among the list of NEOs in Table 5.3.2 with non-zero estimated probability of having encounters below the Lunar Distance, 143651 (2003 QO104) has the slowest close encounters. These relative velocities imply larger scatter during close encounters, including a rapid increase in mean anomaly uncertainty. As shown in Figure 5.9, there is a close encounter in 2220 after which the sequence of encounters becomes unique for each Monte Carlo run.

Figure 5.9 shows the evolution of the orbital elements. By the end of the millennium there is a wide variety of orbits in which 143651 (2003 QO104), product of an undetermined sequence of both close and slow Earth close encounters.

### 5.4.3 Asteroid 66391 Moshup (1999 KW4)

The binary asteroid 66391 Moshup (1999 KW4) has been the object multiple studies relative to its binary system condition. It consists of a primary and secondary of respectively 1.317 km and 0.59 km of diameter [Ostro et al., 2006, Scheirich et al., 2021]. Its rotation states suggest that it is a product of YORP spin-up and disruption [Scheeres et al., 2006, Davis and Scheeres, 2020], and its orbit is expanding in time due to the BYORP effect [Scheirich et al., 2021].

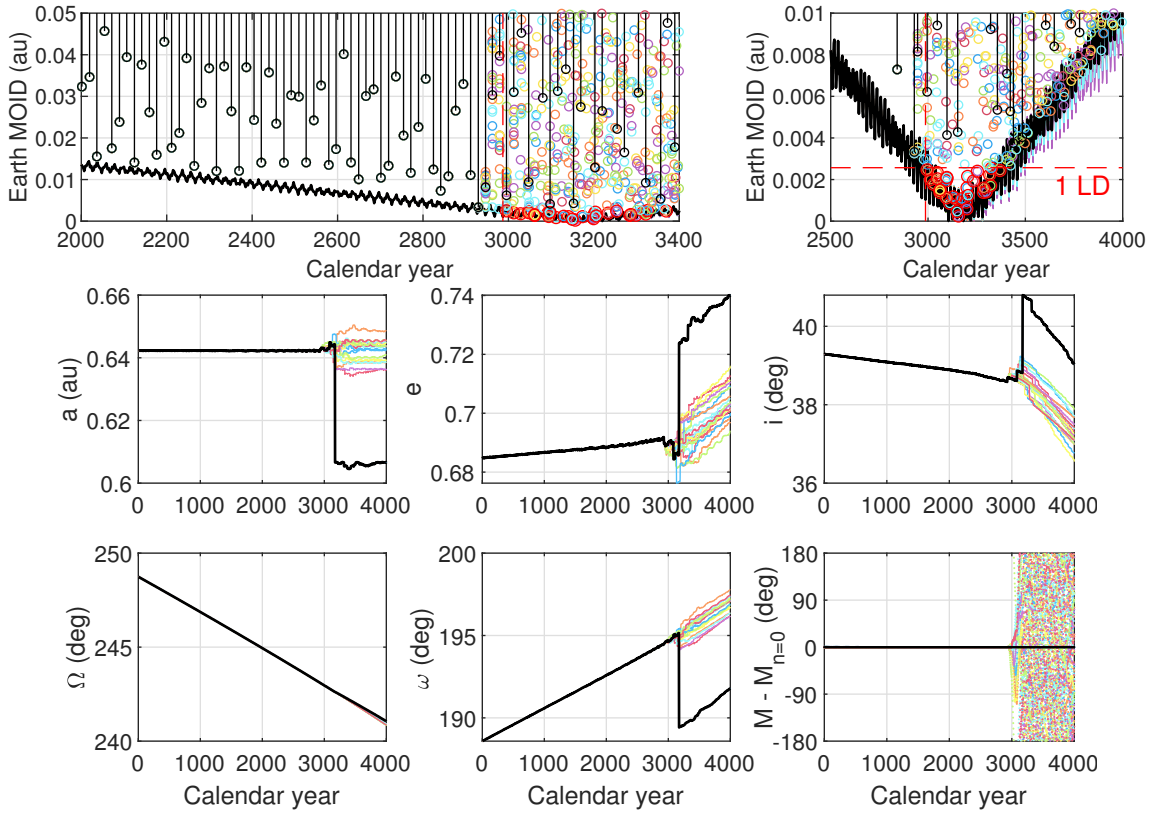


Figure 5.10 Earth close encounters and orbit elements of 66391 Moshup (1999 KW4).

The heliocentric orbit of 66391 Moshup (1999 KW4) is in resonance with the Earth, as it experiences resonant close encounters every 17 or 18 years. The apparition of 2019 allowed observations from multiple observatories, during the 0.0346 au encounter [Scheirich et al., 2021]. The next close encounter will be in May 2036, with a closest distance of 0.0155 au, much closer than the first radar observations obtained using the Goldstone and Arecibo radar systems in May of 2001 [Ostro et al., 2006]. When the MOID becomes small, which is expected to happen slightly before year 3000, many close encounters below the Lunar Distance are recorded in our Monte Carlo analysis. These will cause a large scattering of the orbit as shown in Figure 5.10. Because of how relatively late in the millennium the MOID <1LD condition is held, 66391 Moshup (1999 KW4) is not ranked higher in the list of Table 5.3.2.

### 5.4.4 Asteroid 29075 (1950 AD)

Asteroid 29075 (1950 AD) is representative example of impact probability studies. After it was discovered and tracked for 17 days in 1950 [Wirtanen, 1950], it was lost for 50 years until re-discovered on 2000-12-31. Giorgini et al. [2002] found a close approach in 2880 with the possibility of an impact. Farnocchia and Chesley [2014] modeled the Yarkovsky effect on 29075 (1950 AD) and estimated an impact probability of $2.5 \cdot 10^{-4}$.

The example of 29075 (1950 AD) is paradigmatic in MOID evolution of NEOs. As shown in Figure 5.2, its Earth MOID is secularly drifting to zero. During the decades that this condition is maintained, the probability of experiencing a deep encounter is non-zero. 29075 (1950 AD) was found among the list of km-sized NEOs for which we estimated this probability. As we show in Figure 5.11, the encounters of 2860 and 2880 will occur although with an uncertain closest approach distance.

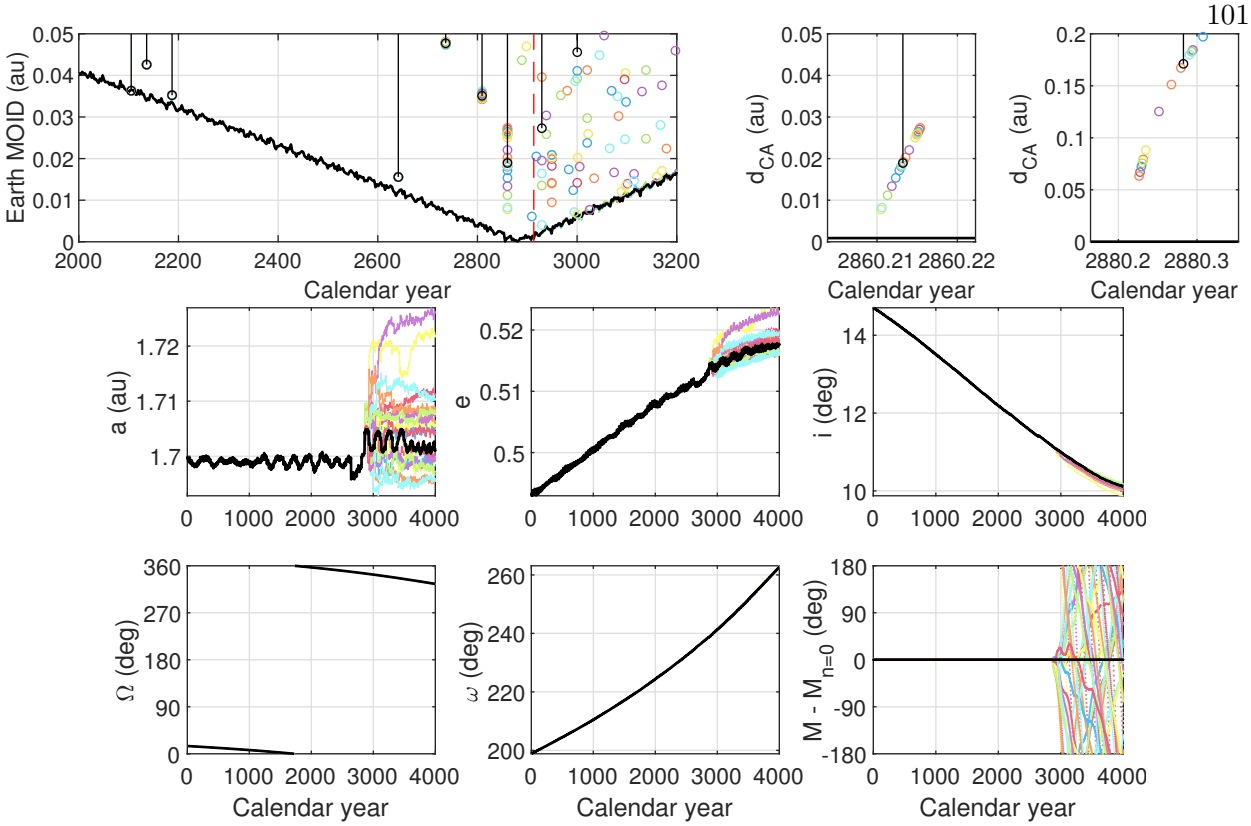


Figure 5.11 Earth close encounters and orbit elements of 29075 (1950 AD).

### 5.4.5 Asteroid 2022 AP7

The km-sized 2022 AP7 is one of the largest PHAs recently discovered [Sheppard et al., 2022]. The orbit of 2022 AP7 is in near-resonance with the orbit of the Earth, meaning that even if its MOID will become small in the next hundreds of years, almost no close encounters are expected in this period of time. The only likely exception is a close encounter in 2363 which will probably to be at a closest approach distance larger than 0.05 au. An interesting finding is that 2022 AP7 comes from a sequence of resonant encounters every 5 years during the 19th century.

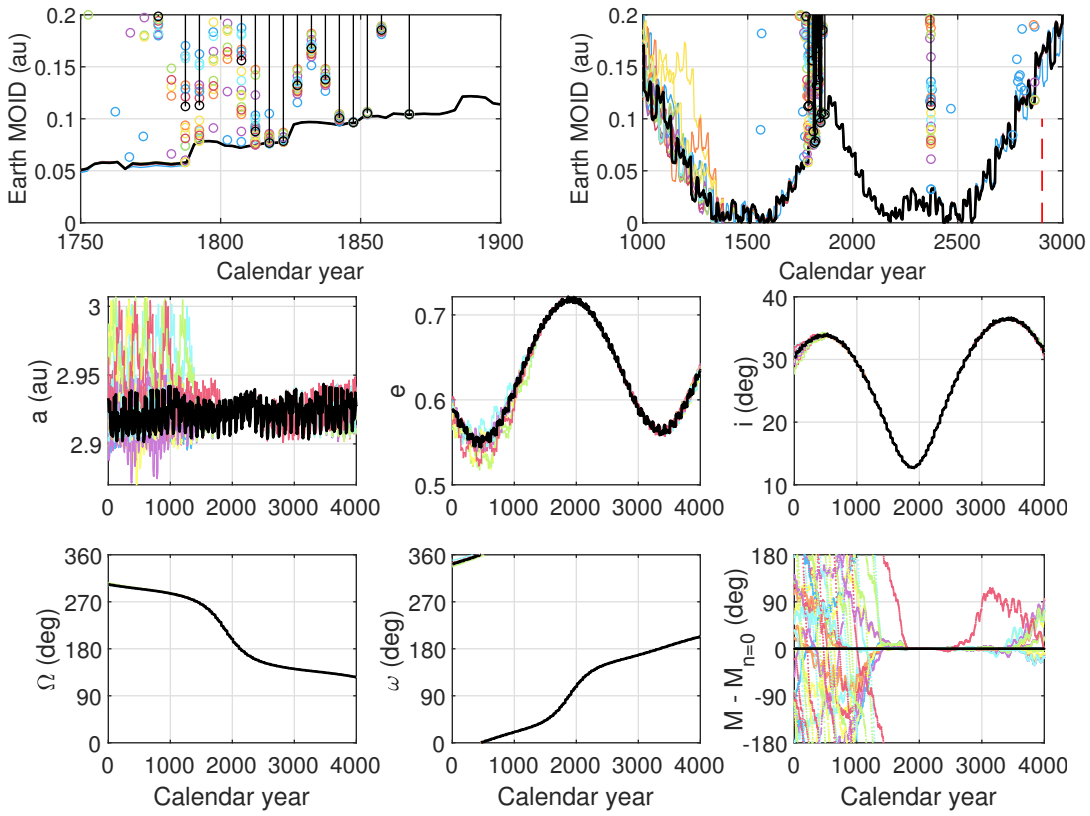


Figure 5.12 Earth close encounters and orbit elements of 2022 AP7.

## 5.5 PHA population evolution by MOID propagation

Another relevant population to understand the background impact hazard is the PHA population. Defined as large enough to cause regional damage ($H < 22$) and currently an Earth MOID $< 0.05$ au, their time-varying nature of the MOID has not been analyzed. We propagate the Earth MOID for a few millennia to determine if the asteroid in question will be hazardous or not over this time-scale, accounting for the stochastic nature of the orbit evolution. This allows us to categorize the orbits of NEOs in groups depending on whether the MOID is secularly increasing/decreasing or they stay in the vicinity of Earth.

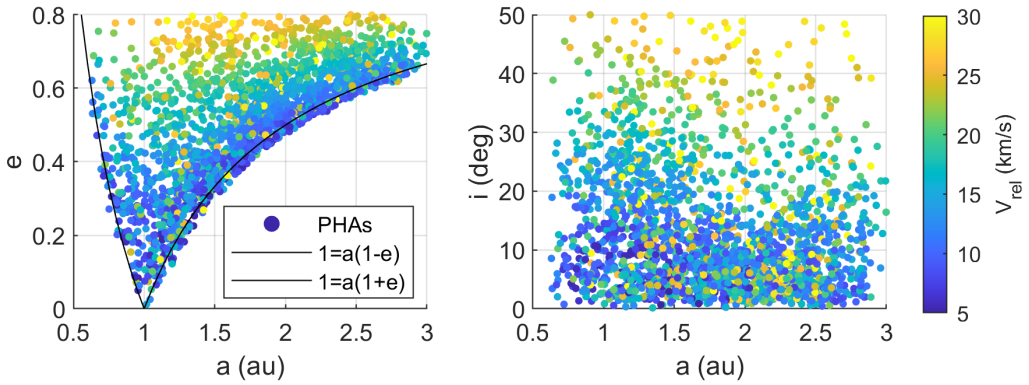


Figure 5.13 Current population of Potentially Hazardous Asteroids by semi-major axis, eccentricity and inclination.

There are currently 2235 PHAs, which represent 7.8% of the discovered NEO population.[5] The population of PHAs is shown in Figure 5.13. We computed their MOIDs with Earth at the reference epoch for the elements of the asteroids. Even if this information is already available, by computing the MOID we can reconstruct the relative geometry at the closest possible flyby, leading to the relative velocities shown in the figure. The relative velocity is a relevant parameter as it drives how energetic the planetary encounters are, influencing the variations in the orbit and physical properties of asteroids.

The influence of eccentricity and inclination can be understood from a geometric point of view, and the ranges of values for PHAs shown in Figure 5.13. The faster the encounter, the smaller is the effect of the flyby on the orbit of the NEO. This means that its long-term orbit is more predictable, since more encounters are required to build-up a significant perturbation. Moreover, on average the NEO spends less time in the vicinity of Earth in which very close encounters can occur.

The other important parameter for the effects of flybys is the closest approach distance, which has an approximate minimum defined by the MOID. This boundary is only surpassed if the exact timing is given and especially in very slow flybys. The condition of being a PHA is already a small MOID, less than 0.05 au. However, this threshold is already large enough such that it can take

[5] As extracted from JPL's Small-body Database (Date accessed: 2022-02-24) - Available for query at: `ssd.jpl.nasa.gov/tools/sbdb_query.html`

hundreds or thousands of years for the asteroid to reach the vicinity of Earth.

The numerical integration tool used in this section consists in the integration in Cartesian space of the trajectory of the asteroid with the 8 planets as third-body perturbers. The orbits of the planets are modelled with an individual set of heliocentric elements, propagated over time with the Laplace-Lagrange secular solutions of section 2.3.1. In particular, we propagate numerically the nominal orbits of the PHA population until we observe the trends in the variation of the MOID. With this result we can already separate the PHAs that pose no threat to Earth in the next few thousands of years and the ones that require deeper study. As we have shown earlier, it is important to identify the next period of very low MOID for each NEO with a decreasing MOID evolution.

In Figure 5.14 we show a few examples of the numerical propagation of the Earth MOID of PHAs over 10,000 years. The PHAs were chosen as the closest to a grid uniformly spaced in semi-major axis and inclination, as shown in Figure 5.14. Because of the NEO and PHA conditions, eccentricity and argument of perihelion are constrained.

With this information we can develop new metrics to identify the current PHAs that pose the highest collision hazard with Earth. For this reason, in addition to the time when the MOID crosses a certain distance threshold, we will also measure the amount of time that the NEO spends under said threshold. This information allows us to distinguish between cases in an extended low MOID period and asteroids that are briefly in the vicinity of Earth, and how briefly.

Figure 5.15 shows the results of the propagation of the MOID for 20 examples of PHAs and histograms for the PHA population over 2000 years. We can see how a few PHAs are drifting away from the region, while others remain in Earth's vicinity. It is also remarkable that the dynamics of some of them are purely secular while others have an oscillatory behavior. The initial population was approximately uniformly distributed in MOID from 0 to the definition threshold of 0.05. After 2000 years there is already a significant decay of the number of PHAs in this threshold, about 45% of the current population. Note that from the overall NEO population there will be additional asteroids falling in the category too, but this gives us an idea of the asteroids currently flagged as PHAs that may leave this category.

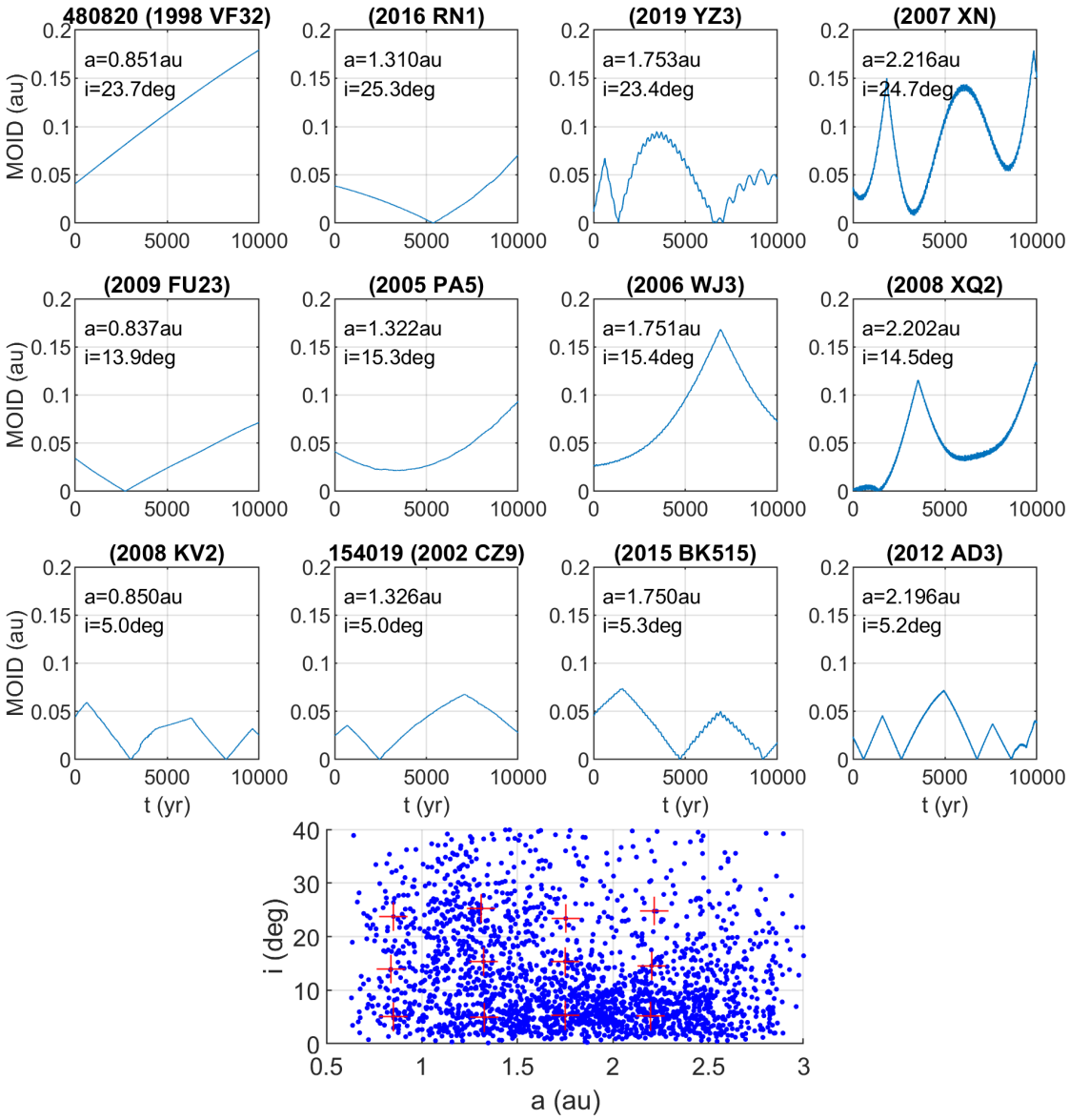


Figure 5.14 10,000 numerical propagation of the MOID of 12 PHAs. The initial conditions of the PHAs are labeled and shown together in the bottom scatter as red crosses.

The dates in which the MOID of every PHA becomes smaller than a Lunar Distance are shown in Figure 5.16. About 6% of the current PHA population have a MOID smaller than a Lunar Distance. After 2000 years, more than 60% of the PHAs have crossed this threshold. Another relevant result is that at all times there are about a hundred PHAs below this threshold. This is important because then the uncertainty in their orbits is more likely to rapidly increase from the presence of close encounters.

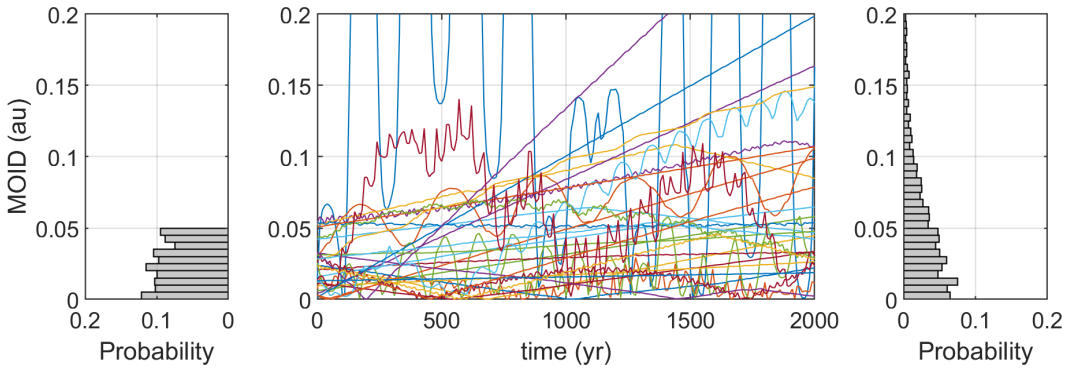


Figure 5.15 Propagation of the MOID of the PHA population. The time history is shown for 20 examples over 2000 years. The left histogram shows the current MOID of the PHA population, the right histogram shows the MOID of the original PHA population after 2000 years.

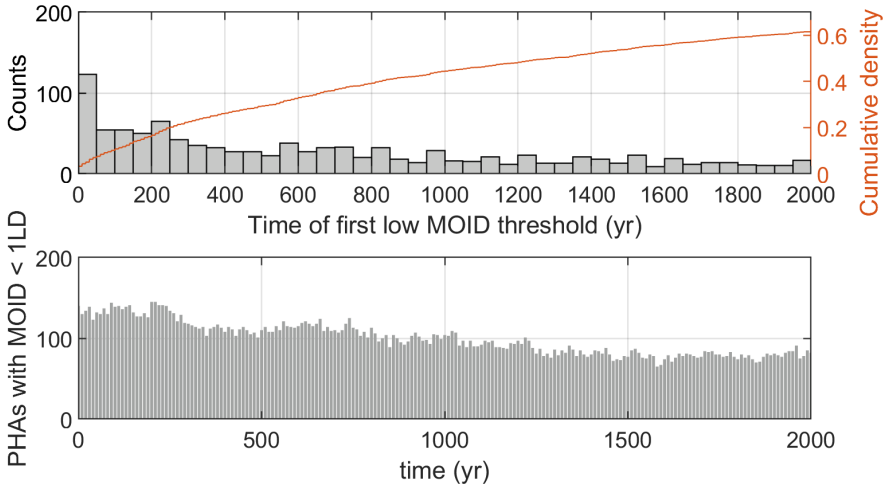


Figure 5.16 Histogram of first date of MOID< 1 LD and number of PHAs with MOID< 1 LD over time.

In this section we propagate the orbits of PHAs once. Thus, the metric for the hazard characterization of equation 5.3 is reduced to the following expression:

$$P(d,T) = \frac{\Delta t_{MOID<d}}{T} P_{MA}(d, \boldsymbol{K}_{Earth}, \boldsymbol{K}_{PHA}) \tag{5.5}$$

In this section we chose $T$=1000 years, as a period of time in which the mean anomaly of the asteroid already becomes unknown but not far enough such that the orbit itself is also completely unknown. The distance threshold chosen is a Lunar Distance.

Table 5.3 Top 10 hazardous asteroids according to $P(d,T)$ for distance threshold of 1 LD and 1000 years.

| PHA | $P$(LD,1000) | $P_{MA}$ | $\Delta t/T$ | $V$ (kms$^{-1}$) | a (au) | e | i (deg) |
|---|---|---|---|---|---|---|---|
| (2021 MU2) | 1.211e-03 | 4.484e-03 | 0.27 | 11.98 | 0.631 | 0.621 | 8.56 |
| 509352 (2007 AG) | 9.456e-04 | 1.576e-03 | 0.60 | 8.83 | 0.721 | 0.374 | 11.95 |
| (2002 AY1) | 5.946e-04 | 1.101e-03 | 0.54 | 17.91 | 0.779 | 0.437 | 29.89 |
| (2009 BE58) | 5.141e-04 | 7.345e-04 | 0.70 | 17.67 | 0.937 | 0.560 | 1.86 |
| (2021 MK1) | 5.042e-04 | 1.050e-03 | 0.48 | 10.54 | 0.808 | 0.288 | 19.24 |
| 416195 (2002 TR190) | 4.736e-04 | 5.776e-04 | 0.82 | 14.54 | 1.077 | 0.160 | 26.92 |
| 415713 (1998 XX2) | 4.628e-04 | 1.543e-03 | 0.30 | 7.93 | 0.741 | 0.368 | 6.97 |
| 164121 (2003 YT1) | 4.535e-04 | 5.890e-04 | 0.77 | 23.71 | 1.110 | 0.292 | 44.06 |
| 468468 (2004 KH17) | 4.380e-04 | 1.460e-03 | 0.30 | 14.13 | 0.712 | 0.498 | 22.12 |
| 469445 (2002 LT24) | 4.338e-04 | 1.668e-03 | 0.26 | 10.23 | 0.720 | 0.496 | 0.76 |

Table 5.5 shows the top 10 PHAs with the highest probability $P(LD, 1000)$ with the intermediate values, relative velocity at the points that define the MOID and initial orbit elements. The probabilities $P$ and $P_{MA}$ are per year (yr$^{-1}$). We compute the relative velocity $V_{inf}$ at the points that define the Earth MOID. Because the probability $P_{MA}$ increases when the relative velocity of the encounters is smaller, this contribution increases for asteroids with a smaller semi-major axis and inclination. It is important to note that the probabilities in the table are not the absolute probabilities of collision as the threshold radius is not the Earth radius.

In this list we find bodies with a significant fraction of time below the Lunar Distance threshold. If we observe the MOID evolution of the top 4 bodies in Figure 5.17 we notice that all of them currently have a MOID <0.01 au and drift towards the zero MOID configuration within the next thousand years. This characteristic is undoubtedly an indication of a potential collision hazard, and was captured by the proposed metric.

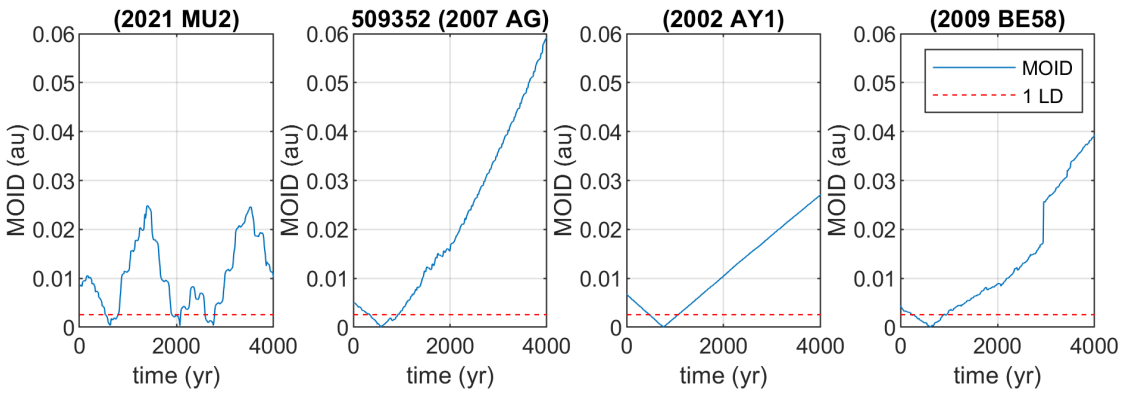


Figure 5.17 Propagation of the MOID of the 4 PHAs with the hightest $P$(1 LD,1000 yr) as given by equation 5.5. The $d = 1$ LD threshold is shown in discontinuous red.

## 5.6 Conclusions

We characterized the long-term collision hazard of NEOs by the evolution of the MOID. The main advantage is that the MOID can be accurately propagated beyond the dates in which the position within the orbit becomes unknown for certain NEOs. In this chapter we push past the typical horizon for impact hazard assessment. Long-term impact hazard assessment can be limited by naturally chaotic dynamics. For example, the orbit of 143651 (2003 QO104) is scattered after a sequence of close encounters. However, in the cases in which the MOID can indeed be propagated confidently for thousands of years, we can point to the dates of interest for hazard characterization or rule out their risk.

**Km-sized NEOs**

We first showed the km-sized NEOs with an Earth MOID $< 0.01$ au of the next centuries. This classification already allowed us to rule out impacts for the majority of the population in the next 1000 years. When the position within the orbit is unknown and the MOID is small, we used an analytical estimation of the impact probability. We used this method to rank the km-sized population by the estimated probability of an Earth encounter of $d_{CA} < 1$ LD. We found that there are a few km-sized near-Earth asteroids whose Earth MOID remains $< 0.01$ au for thousands of years, such as 7482 (1994 PC1), 314082 Dryope (2005 CZ36), or 143651 (2003 QO104).

As we propagate for longer time intervals, it would be possible to simplify further our dynamics and use analytical [Vokrouhlický et al., 2012] or semi-analytical tools that accounted for the growth in uncertainty due close encounters such as derived in chapter 2. The timescales of this study are long enough that the position is stochastic, but short enough that the precise modeling of the long-term effects is required. The range of orbits of the km-sized population allows widely different dynamical regimes. For these reasons, the use of numerical integration is left as the most reliable option.

The metric derived in section 5.2.3 uses an analytical expression that assumes that the mean anomalies are uniformly distributed. This assumption holds when the uncertainty in mean anomaly is large, yet the transition between the deterministic part of the trajectory and this regime must be carefully analyzed. In some cases, these dates contribute the most to the probability of collision of the low-MOID period, as seen in the case of 29075 (1950 AD). We manually checked all the top-ranked asteroids for the presence encounters in this period of time, and displayed some of these examples in section 5.4. The measure of the uncertainty in mean anomaly proves to be useful not only to validate the uniform distribution assumption, but to highlight dates of interest for hazard characterization. With this purpose in mind we find no need to increase the number of Monte Carlo samples to increase the accuracy in our predictions. The present work provides a list of asteroids and dates in which impact monitoring tools can be used to more accurately determine impact probabilities far beyond the default dates reported by impact monitoring systems.

Natural extensions of this work would be to broaden the selected group of asteroids from the km-sized population to PHAs or the whole NEO population. The MOID evolution as characterized in this work suggests a significant flux in and out of Earth's vicinity, implying the flux in and out of the PHA category in timescales of decades to centuries shown in section 5.5. The long-term hazard ranking could be made available to the planetary defense community, as the most hazardous NEOs should be objects of interest for more detailed observations and future exploration missions.

**PHA population**

In this section we study the PHA population to asses their collision risk in timescales of millennia. We characterized when the PHA reaches the vicinity of Earth, and if it does, for how long it stays in this region. This information allows us to classify the asteroids currently in the PHA category, to find that at least 40% of them never come to the vicinity of Earth and so forth they pose no collision hazard to Earth. Similarly, we can identify the PHAs with an upcoming low MOID period as targets of interest. We developed a new metric that allows us to combine this fact with the probability that Earth and the asteroid are in the ranges of mean anomalies compatible with a collision. We ranked this list to point to the PHAs with the higher probability of collision in the next 1000 years.

We studed the asteroids currently identified as Potentially Hazardous, as we want to understand the type of hazard they represent based on their orbit evolution in the next thousands of years. A different question that is left for future work is about the hazard of the NEO population in general, as both of the PHA and NEO catalogs have observational biases. We acknowledge this bias and limit ourselves to solve the initial question, as it already sheds insight into the dynamics of the MOID in the inner Solar System and its relevance to the characterization of the hazard of NEOs.

An exact measurement of the probability of collision requires a large scale Monte Carlo simulation of each of the asteroids. However, including the propagation of the uncertainty in the orbits of the asteroids gives us the uncertainties in our characterization of the upcoming low MOID period. A generalized way to study the whole NEO population is left as future work, as it is challenged by a diversity in the quality of the available orbit solutions.

# Chapter 6

# MOID evolution in Analytical Resonant Encounters

## 6.1 Introduction

Computing the risk of an Earth collision of near-Earth Asteroids (NEAs) is one of the main planetary defense efforts. During a close encounter it is necessary to address whether or not the asteroid will cross a keyhole that leads to a collision in the future. In this chapter we aim to provide tools to better characterize the locations of keyholes in the B-plane, which is assessed throughout the B-plane in preliminary collision hazard analysis. If instead of the radius of the planet we define a larger closest approach distance threshold, the keyholes can refer to the paths to a deep encounter, which also requires future detailed analysis for hazard characterization.

In rare occasions, high-fidelity models of the asteroids are available, which allow for a detailed keyhole analysis for more than 100 years. An example is the analysis of Bennu in Farnocchia et al. [2021], which used OSIRIS-REx data to incorporate high-fidelity dynamics including Yarkovsky effect, solar radiation pressure, and Poynting–Robertson drag. They were able to refine the impact hazard assessment and identified keyholes that persist or else should be ruled out. These results show how sensitive keyholes are to changes in dynamics and the importance to improve the current models. The context of this work is preliminary analysis, such as that performed soon after the discovery of an asteroid, in which we need to study a large region of the B-plane and the trade-off between models of variable fidelity.

The analytical methods to solve for the outcome of planetary close encounters are referred as Öpik theory [Öpik, 1976], which was extended analytically to the full set of Keplerian elements

as extended Öpik theory [Valsecchi et al., 2003]. One of their main outcomes of the theory is the computation of resonant circles (referred to as Valsecchi circles). Valsecchi circles are the locus of points such that a subsequent encounter occurs after $k$ planet periods and $h$ asteroid periods [Valsecchi et al., 2003, 2015]. Within the resonant circles they identify the regions where keyholes exist. However, they assume that the asteroid undergoes Keplerian motion between resonant encounters. i.e., the MOID is assumed constant between close encounters. This assumption can become an important limitation in the frequent case that other bodies perturb the orbit of the asteroid. In some of these works, the authors already discussed that the non-Keplerian MOID effect is important and needs to be included. In particular, they recognize that the MOID evolves according to secular and short-periodic effects between encounters. The short-periodic effects, which are hard to model through an analytical theory, are often of the order of several Earth radii, which limits the application of analytical theories.

In the B-plane and assuming a circular orbit for the planet, the $\xi$ coordinate corresponds to the minimum orbit intersection distance (MOID) [Valsecchi et al., 2003, 2015]. In this chapter we analyze the effects of non-Keplerian dynamics of the MOID between encounters to find the modified location of keyholes or modified keyholes. Milani et al. [2005] assume Keplerian motion between encounters, hence a constant MOID. Gronchi and Tardioli [2013] developed a piecewise continuous averaged solution for the dynamics in the Sun-Earth-asteroid restricted three-body problem based on an averaged treatment for Earth-crossing orbits in Delaunay elements [Gronchi and Milani, 1998, Gronchi, 2002]. They introduce a signed orbit distance that does not present singularities at encounters, and they apply this to estimate crossing times (and thus potential close encounter epochs) of near-Earth asteroids.

Our goal in this chapter is to improve the computation of keyholes by using more realistic dynamics for the trajectory propagation of the asteroid while leveraging the decreased computational time afforded by an analytical theory. Furthermore, in this work we assess the effect of the non-Keplerian MOID evolution on the computation of keyholes. We compute the evolution of the MOID as a result of the analytical secular propagation of the heliocentric orbit considering

the perturbation of Jupiter. This effect drives the long-term evolution of the heliocentric orbit of asteroids, as shown in Chapter 2. Given significant contributions of the shallow encounters between the deep resonant encounters, we also use the semi-analytical propagation tool to rapidly propagate the orbits of the asteroids. Numerical results are provided for each method. We use asteroids 99942 Apophis and 2006 MB14 as benchmarks, in their respective Earth encounters of April 2029 and June of 1985.

We present this chapter as follows: A brief introduction on how to model close encounters in section 6.2, along with relevant tools and definitions. In section 6.3 we describe the different propagation methods used for the MOID between close encounters. Next, in section 6.4, we quantify the amplitudes of the short-period components on the MOID evolution along with their impact on the keyhole locations. Last, after presenting the techniques and theoretical background, we describe the keyhole computation criterion in section 6.5 for both Keplerian and non-Keplerian motion assumptions.

## 6.2 Close encounters and the B-plane

Planetary encounters cause the orbits of near-Earth objects to abruptly change in very short time scales. This change in heliocentric elements is very sensitive to the initial conditions of the flyby. In this section we define in detail the process of extraction of ephemeris, frame transformations and evaluation of the encounter.

We map the heliocentric coordinates of the NEO to the B-plane, a planetocentric reference frame to used analyze the encounter [Farnocchia et al., 2019]. The modified target plane (MTP) allows to uniquely define the flyby using the coordinates at periapses. Hence, we use it to define the encounter coordinates. Then, we solve the encounter and obtain the new set of heliocentric elements.

### 6.2.1 The B-plane

First, we obtain the heliocentric Cartesian coordinates of asteroid and planet when the asteroid is in the vicinity of the planet. The orbit of the planet is assumed circular in consistency with the general Öpik theory [Valsecchi et al., 2003]. We map the heliocentric coordinates to a planetocentric frame defined as follows: centered at the planet, Y-axis aligned with the direction of the planet motion, Z-axis parallel to the angular momentum vector of the planet, and X-axis completing the frame. The B-plane orientation is normal to the relative asymptotic velocity $U$ in the planetocentric frame [Greenberg et al., 1988]. Using the vector components of $U$ we obtain the angles $\theta, \phi$:

$$\begin{bmatrix} U_x \\ U_y \\ U_z \end{bmatrix} = \begin{bmatrix} U \sin\theta \sin\phi \\ U \cos\theta \\ U \sin\theta \cos\phi \end{bmatrix} \tag{6.1}$$

The angles $\theta, \phi$ map the relative position to the B-plane coordinates $\xi - \eta - \zeta$ as the consecutive following rotations: a rotation of $-\phi$ about $Y$ and a rotation of $-\theta$ about $\xi$ -positive counterclockwise. This rotation can be applied at any time during the planetary flyby, most commonly when the asteroid crosses the sphere of influence of the planet. In this work, we apply this rotation at the time of periapsis passage of the flyby as explained in the next section.

### 6.2.2 The Modified Target Plane

In the definition of the B-plane coordinates the time to switch to the planetocentric frame is a free parameter. Using the modified target plane (MTP) this time is uniquely defined as the time of periapsis $t_p$ [Tommei, 2002]. We transform the MTP coordinates to the B-plane using conservation of energy and angular momentum. Figure 6.1 shows the two reference planes. Then, we use the B-plane coordinates to obtain the coordinates after the encounter.

The process to obtain these elements follows the extended Öpik theory: we convert the relative Cartesian coordinates to planetocentric Keplerian elements, to obtain the time of perapsis $t_p$. From that time we generate the set of planetocentric coordinates at the time of periapsis. We

denote variables at periapses with the subindex $p$. Using the relative velocity at periapsis $\boldsymbol{v_p}$ we obtain the angles $\theta_p, \phi_p$ from equation 6.1:

$$\begin{bmatrix} \cos\theta_p \\ \tan\phi_p \end{bmatrix} = \begin{bmatrix} v_{p,y}/v_p \\ v_{p,x}/v_{p,z} \end{bmatrix} \tag{6.2}$$

Using these angles we obtain the position in the modified target plane $(\xi_p, \zeta_p)$ from the planetocentric coordinates $\boldsymbol{r_p} = \boldsymbol{(X_p, Y_p, Z_p)^T}$:

$$\begin{bmatrix} \xi_p \\ \eta_p \\ \zeta_p \end{bmatrix} = \hat{\boldsymbol{R}}_{\xi_p}(-\theta_p)\hat{\boldsymbol{R}}_{Y_p}(-\phi_p) \begin{bmatrix} X_p \\ Y_p \\ Z_p \end{bmatrix} \tag{6.3}$$

From these coordinates we obtain the B-plane coordinates using conservation of energy and angular momentum:

$$U^2 = 2\frac{GM_p}{r_p} + v_p^2 \tag{6.4}$$

$$r_p v_p = bU \tag{6.5}$$

$$\begin{aligned} \zeta &= \left(\tfrac{v_p}{U}\right)\zeta_p \\ \xi &= \left(\tfrac{v_p}{U}\right)\xi_p \end{aligned} \tag{6.6}$$

We rotate the relative velocity at perigee by an angle $\gamma/2$ about the angular momentum vector of the hyperbola, where $\gamma$ corresponds to the deflection angle (Eq. 6.7). The deflection angle is defined as a function of the relative velocity $U$ and the mass of the planet $m$, which is expressed in Sun mass units.

$$\boldsymbol{U} = U\hat{\boldsymbol{R}}_h\left(-\frac{\gamma}{2}\right)\hat{\boldsymbol{v}}_{\boldsymbol{p}} \tag{6.7}$$

$$\tan\frac{\gamma}{2} = \frac{m}{bU^2} = \frac{c}{b} \tag{6.8}$$

where $c = m/U^2$. The rotated relative velocity defines the orientation of the B-plane $\theta, \phi$. These B-plane coordinates define the effect of the close encounter as explained in detail in the following section.

### 6.2.3 Encounter solution

In Figure 6.1 we introduce the target and modified target planes, as related by equation 6.8. These planes are related by the deflection angle between the relative velocity and velocity at periapses.

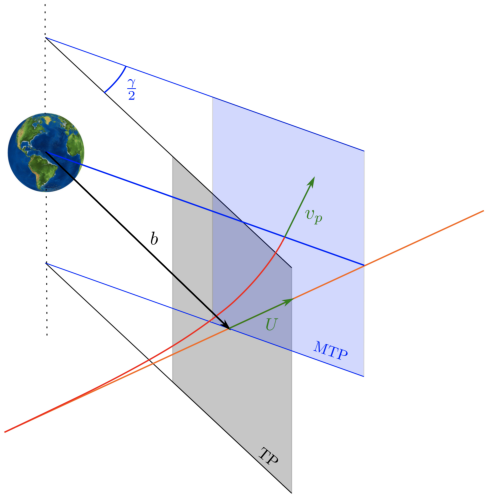


Figure 6.1 Planetary flyby target plane (TP) and modified target plane (MTP).

The effect of the planetary encounter is a rotation of the relative velocity by a deflection angle $\gamma$. The post-encounter B-plane rotates with the relative velocity. Thus, we solve for the post-encounter B-plane coordinates with a rotation of the deflection angle $\gamma$:

$$\boldsymbol{U}' = \hat{\boldsymbol{R}}_h(\gamma)\boldsymbol{U} \tag{6.9}$$

$$\boldsymbol{b}' = \hat{\boldsymbol{R}}_h(\gamma)\boldsymbol{b} \tag{6.10}$$

The solution of the encounter in vectorial equations is referred as pseudo-Öpik theory [Greenberg et al., 1988]. These equations can be rewritten into scalar components for each of the post-encounter coordinates [Valsecchi et al., 2003]. Valsecchi et al. [2015] show how the post-encounter heliocentric elements are obtained from the direct mapping of B-plane coordinates to Keplerian elements. In some cases the scalar equations become singular and pseudo-Öpik theory must be used to robustly compute the outcome of the encounter. The encounters analyzed in this work satisfy the assumptions of the extended Öpik theory and only small regions of the B-plane near the collision singularity require the use of pseudo-Öpik theory.

### 6.2.4 Resonant returns

The condition for a resonant encounter is that the post-encounter semi-major axis $a'$ results in a commensurability between the orbital periods of the planet and the asteroid. In this situation the resonant encounter occurs after $k$ planet periods and $h$ asteroid periods. The condition on the semi-major axis becomes:

$$a_R'^{\,3} = a_p^3 \frac{k^2}{h^2} \tag{6.11}$$

The locus of points in the B-plane that fulfill the condition of a resonant semi-major axis $a'$ is a resonant circle of radius $R$ centered in $(0, D)$ with parameters $R, D$ [Valsecchi et al., 2003]:

$$R = \left| \frac{c \sin \theta_R'}{\cos \theta_R' - \cos \theta} \right| \tag{6.12}$$

$$D = \frac{c \sin \theta}{\cos \theta_R' - \cos \theta} \tag{6.13}$$

where

$$\cos \theta_R' = \frac{1 - U^2 - 1/a_R'}{2U} \tag{6.14}$$

Figure 6.2 shows the resonant circles of the 1985 flyby of 2006 MB14 for up to $k = 20$ Earth revolutions. The white circle represents the Earth radius with its gravitational focusing factor and

physical radius. If unperturbed Keplerian motion is assumed between encounters, no change in geometry happens for the next encounter. Therefore, we can state:

$$U'' = U' = U, \quad \theta'' = \theta', \quad \phi'' = \phi' \tag{6.15}$$

Assuming the planet is in a circular orbit, the B-plane coordinate $\xi$ is the MOID between the asteroid and the planet. Based on the previous assumptions, $\xi$ remains constant between encounters, thus:

$$\xi'' = \xi' \tag{6.16}$$

and the timing component of the flyby $\zeta''$ becomes:

$$\zeta'' = \zeta' - [\mathrm{mod}(h \cdot 2\pi a'^{3/2} + \pi, 2\pi) - \pi] \sin\theta' \tag{6.17}$$

Based on the assumption of equation 6.16, the keyholes in the B-plane are located in the pre-encounter coordinates that lead to a post-encounter $|\xi'| < \gamma R_E$. Thus, they are in the band around $\xi = 0$ that is shown in the right panel of Figure 6.2.

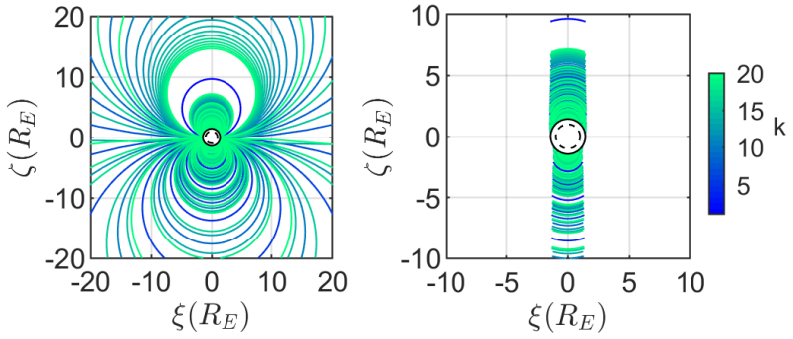


Figure 6.2 Resonant circles and keyholes of the Earth flyby of asteroid 2006 MB14.

## 6.3 MOID propagation

The Minimum Orbit Intersection Distance (MOID) is defined as the minimum distance between any two points in the orbits of the two bodies at a given instant of time. In Öpik theory the coordinates in the B-plane are $\xi - \zeta$, which correspond to the signed MOID and a timing condition.

Thus, a MOID smaller than the collision radius is a necessary condition for a collision. The collision radius is the radius of the planet with a gravitational focusing factor. To compute the MOID we implemented the algorithm proposed by Wiśniowski and Rickman [2013].

The initial conditions for the propagation using either of the models are extracted from the incoming hyperbolic asymptote of the flyby during the respective Earth close encounters. The trajectory of the asteroid is extracted from JPL's SSD HORIZONS system.[1] Then, these coordinates are transformed to the MTP as defined in section 6.2.2. In the case of 2006 MB14, the nominal closest approach date of the encounter is 1985-Jun-28 00:40 TDB, whereas for 99942 Apophis, the closest approach date is 2029-Apr-13 21:46 TDB.

### 6.3.1 MOID propagation by Secular Model

We can also propagate the MOID using the secular solution of the perturbation from Jupiter of equations 2.12. In order to compute the MOID at a future time, we compute the orbit at the desired time and use the regular MOID algorithm.

In the case of 2006 MB14, we find that the post-encounter secular rates of the MOID are in the range of $\sim$0.05-0.3 $R_E/yr$, which correspond roughly to the maximum and minimum semi-major axes resulting from the encounter at any resonant circle. In the case of Apophis, the rate goes up to 0.1 $R_E/yr$, in general smaller than this value.

### 6.3.2 MOID semi-analytical propagation

In addition to the purely analytical secular propagation of the orbit, we can use the semi-analytical tool of section 2.4 that includes the evaluation of close encounters. The main difference form the usage in chapter 2 is that we increase the threshold of the closest approach distance to 0.15 or 0.2 au so that we include smaller effects, since these can already be in orders of magnitude of a few Earth radii.

[1] Publicly available at: `https://ssd.jpl.nasa.gov/horizons/`

### 6.3.3 MOID propagation by Numerical integration of n-3BP

In this approach, we propagate the heliocentric orbit of the asteroid numerically under the influence of gravitational perturbations from all planets. We account for all the planets of the solar system and work under the assumption that they follow Keplerian orbits. This choice is made so that we maintain the encounters as well as capture long and short-term perturbations effects over time. In this case we are not solving for the gravitational interactions between the planets. Thus, the model includes the perturbation of n third-body perturbers (n-3BP).

The perturbing force contribution to the equations of motion for $n_p$ bodies is:

$$\boldsymbol{f}_{3B} = \sum_{j=3}^{n_p} GM_j \left( \frac{\boldsymbol{r}_{2j}}{r_{2j}^3} - \frac{\boldsymbol{r}_{1j}}{r_{1j}^3} \right) \tag{6.18}$$

where the subscript $j$ refers to each body. In this case, $j = 1$ refers to the central body (Sun) and $j = 2$ to the asteroid. Thus, $\boldsymbol{r}_{1j}$ is the position vector of body $M_j$ with respect to the Sun and $\boldsymbol{r}_{2j}$ with respect to the asteroid. The elements of the planets are constant and extracted from planetary ephemeris [Folkner et al., 2014] at the same date that the asteroid ephemeris was retrieved.

We integrate these equations using MATLAB's *ode113* numerical integrator. *ode113* is a variable-step, variable-order (VSVO) Adams-Bashforth-Moulton PECE solver of orders 1 to 13. The highest order used for the integration is 12, whereas the 13th order is used for the error estimate [Shampine and Reichelt, 1997].

In figure 6.3 we demonstrate all of the previously described models of the propagation of the MOID. Asteroid 2006 MB14 is a good example of a MOID evolution dominated by the secular drift. The case of 99942 Apophis is more difficult to model, as there are frequent shallow encounters with the Earth or other inner solar system planets. In both cases the MOID shows perturbations of short period that can be of the order of a few Earth radii.

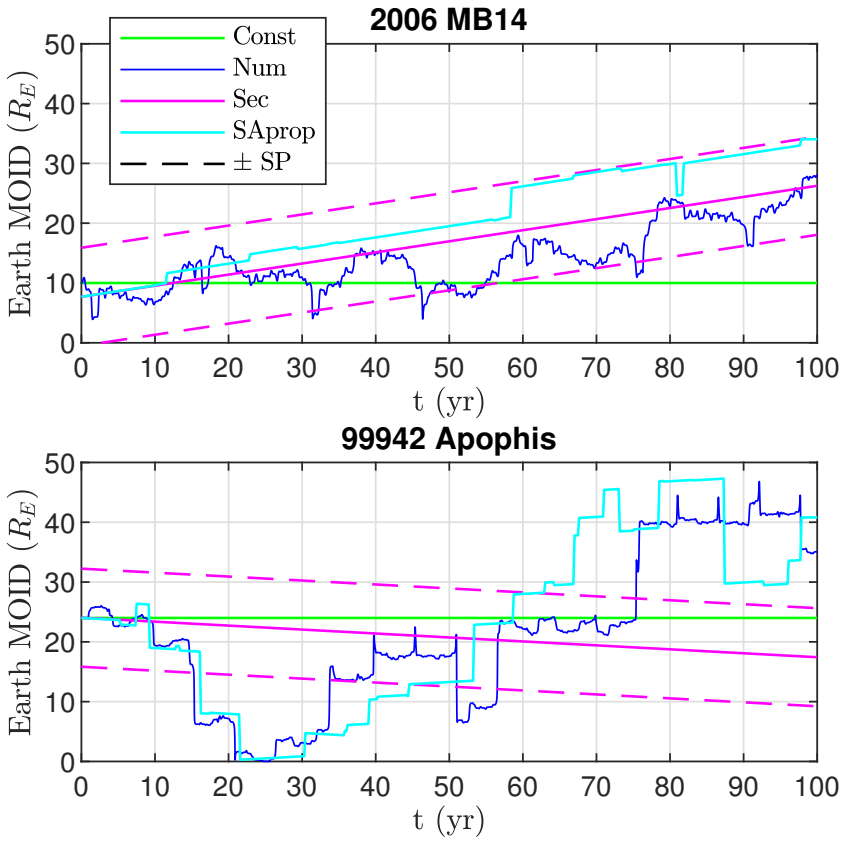


Figure 6.3 Examples of the Earth MOID ($R_E$) of 2006 MB14 and 99942 Apophis after crossing the B-plane.

## 6.4 Short-period component characterization

As we presented in the previous section, the propagation of the MOID in the absence of close encounters has a secular component and a short-period oscillation. Quantifying this amplitude we can define a bound around the secular propagation in which we would expect to find the MOID in the future. Figure 6.3 shows the propagation of the MOID with the bounds defined around the secular component of the MOID (magenta, dashed) and the previously described models. In the example of 2006 MB14, the secular bounds capture most of the evolution of the MOID. These bounds are computed using the method below. Other cases such as 99942 Apophis experience larger perturbations such that the numerically propagated MOID is captured by the bounds for a limited amount of time.

The amplitude of the short-period component $\Delta_{SP}$ can be obtained semi-analytically, from

the difference between the perturbing potential in equation 2.1 and the analytical expression of the averaged potential in equation 2.3 [Scheeres, 2016]. However, we find that the computational cost of the quadrature of the Lagrange Planetary Equations is comparable to a few numerical propagations of the MOID. For this reason and to investigate a wide variety of post-encounter orbits, we compute this amplitude for a grid of points in the B-plane.

The amplitude is approximated by the difference between the maximum and minimum $\xi$:

$$\Delta_{SP} = \max(\xi(t)) - \min(\xi(t)) \tag{6.19}$$

This estimation doubles the typical definition of a sinusoidal oscillation. Thus, we are making a conservative estimation of this amplitude. In the examples of this work we propagate the orbit for 10 years, which accounts for a few orbital periods. In this timescale very close encounters were not found among the post-encounter trajectories and the secular contribution is small.

Next, we investigate whether or not the short-period amplitude of the MOID remains constant among the post-encounter trajectories, and its potential use to predict the overall evolution. To do this, we propagate the MOID numerically among a fine grid of points of the B-plane. Figure 6.4 shows that along the B-plane, most post-encounter trajectories have a similar amplitude of the short-period component. This result motivates the use of a unique amplitude value for the propagation of the MOID.

Another result of the numerical propagation of the MOID along the B-plane is the minimum MOID throughout the 100 years, also shown in Figure 6.4. The secular component of the MOID evolution is clearly distinguished: in the region with a negative MOID trend (either $\pm\xi$) there is at least one future zero-MOID crossing. On the other semi-plane of the B-plane the MOID grows secularly, which implies that keyholes are less likely to be found. In the next section we sample points among resonant circles, and we find that it is indeed possible to have future low-MOID configurations in the semi-plane of the B-plane with secularly increasing MOID.

The analytical and semi-analytical propagation models can be compared to the numerical

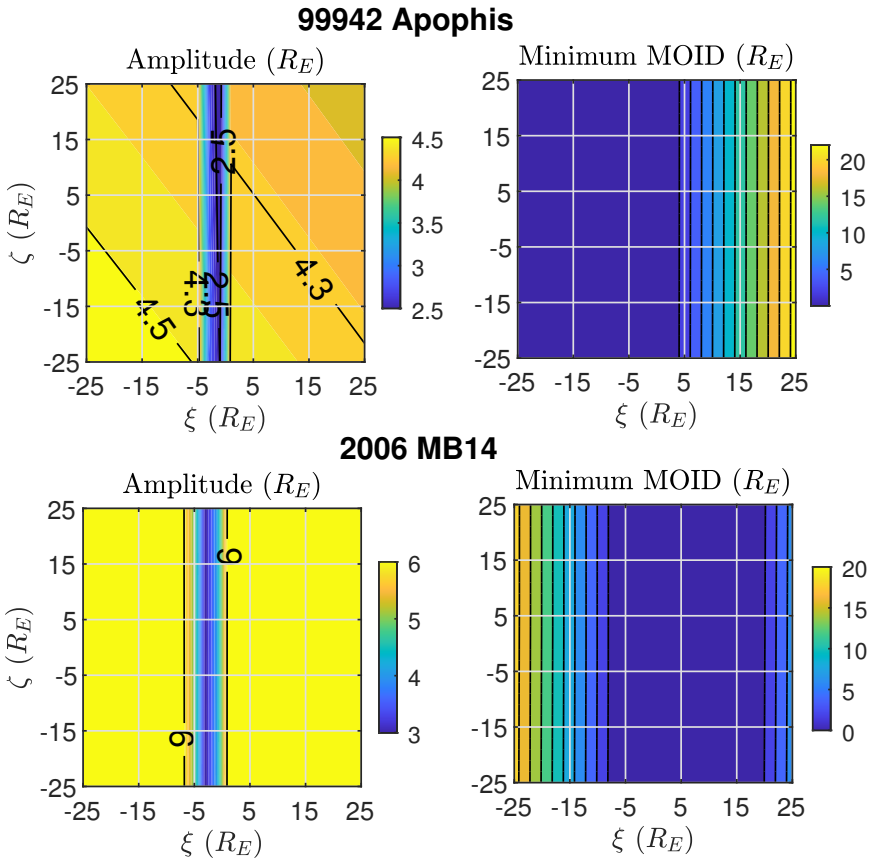


Figure 6.4 Amplitude of short-period component of MOID and minimum MOID over 100 years.

propagation taking into account the short-period component amplitude as conservative bounds. Thus, we can test if the numerical propagation remains within these bounds. The amplitude of the short-period component is found to be of 5.05 $R_E$ for 99942 Apophis and of 6.77 $R_E$ for 2006 MB14. We extend these bounds by the Earth radius expanded with the corresponding focusing factor for consistency with the computation of keyholes in the next section. The result after propagating the MOID for 50 years is that the estimated bounds around the secular model only capture the trajectories for 89% of the time for 2006 MB14, and only 35% for Apophis.

When the MOID obtained numerically is out of the defined bounds we can measure how far it is from this expected region. In the 100 years propagated, maximum deviation from the bounds for 2006 MB14 was of 12 Earth radii, on average in the B-plane. For 99942 Apophis, this maximum deviation is between 25 and 64 Earth Radii. This means that the combined secular and short-period

bounds approach for 99942 Apophis does not consistently capture the long-term dynamics of the MOID.

## 6.5 Modified keyhole computation

A keyhole is the locus of points on the B-plane leading to a collision at a subsequent encounter; i.e., it is the pre-image of the Earth on the B-plane of the first encounter. In order to find keyholes we test multiple points along the resonant circles. The concept of keyhole can be generalized to distance threshold larger than the focusing factor radius, highlighting deep encounters that do not necessarily correspond to a collision. We describe the conditions for a point to be a keyhole and how these are modified by a time-varying MOID.

If we assume that the heliocentric post-encounter Keplerian elements remain constant between encounters, the $\xi$ coordinate that represents the MOID also remains constant. However, using the MOID propagation methods we can model different perturbing effects and include them in the computation of keyholes. As an extension of this theory we define the modified keyholes as the points that fulfil the keyhole conditions accounting for the MOID variation between encounters. First, we detail the method of Valsecchi et al. [2003] for the computation of keyholes under unperturbed MOID. Then, we show the derived modification to obtain the new keyhole regions and the application to the Earth flybys of asteroid 2006 MB14 and 99942 Apophis.

We sample points among the resonant circles, which are virtual asteroids that will experience a subsequent encounter. We propagate the virtual asteroids from the post-encounter elements using the three models described above for the corresponding $h$ asteroid periods or $k$ Earth periods. As an example of this propagation, we show a virtual Apophis that crosses the resonant circle $\{k = 5, h = 7\}$ and assuming the Earth is in a circular-ecliptic orbit.

In Figure 6.5 we show the distance between the asteroid and the Earth recorded with the three approaches used and constant elements: Keplerian propagation, secular model, semi-analytical propagation and n-3BP model. For context we show the MOID evolution in this time frame as well as the distance in detail at the resonant encounter after 5 years. The differences between Earth-

asteroid distance models are in the order of Earth Radii, and the difference becomes apparent at the resonant encounter date. The propagated MOID defines whether a collision is possible at the time of the resonant encounter. Thus, we consider the variation of the MOID in the definition of the modified keyholes.

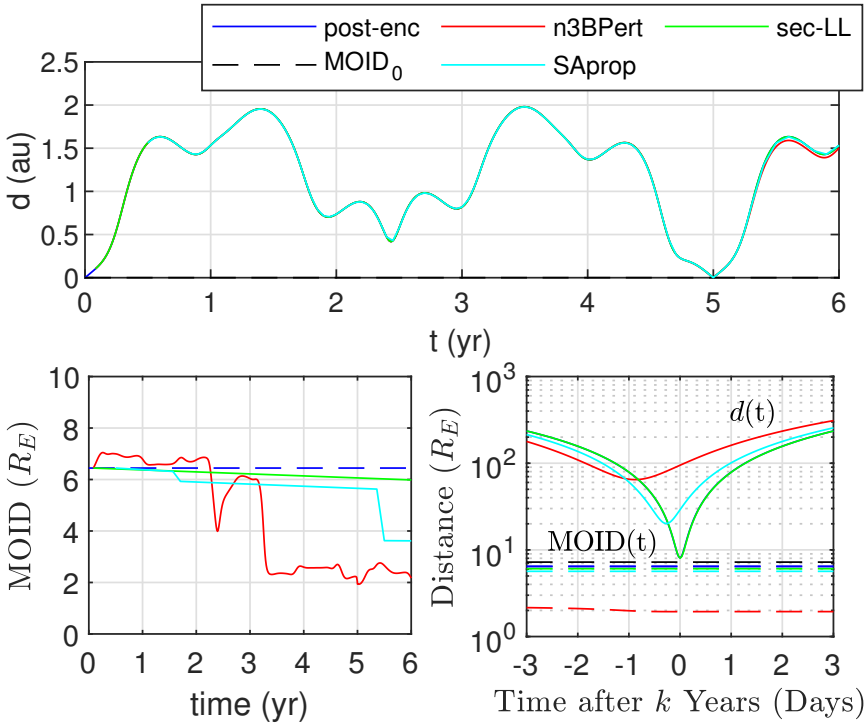


Figure 6.5 Distance between Earth and 2006 MB14 after it crosses the resonant circle $\{k = 5, h = 7\}$ and MOID evolution.

### 6.5.1 Constant elements between encounters

We find the keyholes coordinates $(\xi_K, \zeta_K)$ using the following method. The condition for a collision in the subsequent resonant encounter ($''$) is that the MOID $|\xi''|$ is smaller or equal to the radius of collision $b_p$. Under the assumption that the MOID is unchanged by the Keplerian propagation ($\xi'' = \xi'$), we can define the necessary condition for a given $(\xi_K, \zeta_K)$ to belong to a keyhole as:

$$|\xi''_K| = |\xi'_K| = |\xi'(U, \theta, \xi_K, \zeta_K)| \leq R_c \tag{6.20}$$

where $R_c$ is the planet radius extended by the gravitational focusing factor:

$$R_c = R_P\sqrt{1+\frac{2GM_P}{R_pU^2}} \tag{6.21}$$

where $R_P$ and $M_P$ are the planet's physical radius and mass, respectively. If the above condition is satisfied, we use a root-finding algorithm to find the value $\zeta_{K,0}$ that corresponds to a direct impact with Earth,

$$\zeta''_{K,0} = \zeta''(U,\theta,\xi_K,\zeta_{K,0}) = 0 \tag{6.22}$$

where the function $\zeta''$ is obtained from the solution of the encounter as described in section 6.2.3. Thus, using the approximation in $\zeta$":

$$\zeta'' \approx \frac{\partial\zeta''}{\partial\zeta}|_{\zeta=\zeta_{K,0}}(\zeta-\zeta_{K,0}) \tag{6.23}$$

the upper and lower bounds of the keyhole are:

$$\zeta_{K,u} = \zeta_{K,0} + \frac{\sqrt{b_P^2-{\xi''_K}^2}}{(\partial\zeta''/\partial\zeta)_{\zeta=\zeta_{K,0}}} \tag{6.24}$$

$$\zeta_{K,l} = \zeta_{K,0} - \frac{\sqrt{b_P^2-{\xi''_K}^2}}{(\partial\zeta''/\partial\zeta)_{\zeta=\zeta_{K,0}}} \tag{6.25}$$

where the derivative $(\partial\zeta''/\partial\zeta)_{\zeta=\zeta_{K,0}}$ is

$$\frac{\partial\zeta''}{\partial\zeta} = hs(U',\theta')\frac{\partial\cos\theta'}{\partial\zeta} + \frac{\partial\zeta'}{\partial\zeta} \tag{6.26}$$

The expressions to find the factor $s(U',\theta')$ and $\frac{\partial\zeta'}{\partial\zeta}$ are reported in Valsecchi et al. [2003]. The keyhole is constructed by repeating this procedure for each $(\xi_k,\eta_k)$ on $k$: $h$ resonant circle.

### 6.5.2 Modified keyholes by propagation of the MOID

We propose the modification of the keyhole criterion on $\xi_K$ by including the time propagated variation $\Delta\xi$. The modified keyholes are the regions that fulfill the new keyhole conditions, having considered the $\Delta\xi$. We estimate $\Delta\xi$ computing the MOID both at the initial and subsequent encounter, such that:

$$\Delta MOID = \Delta\xi = \xi'' - \xi' \tag{6.27}$$

We follow two different approaches to compute the MOID as presented in Section 6.3: a semi-analytical propagation and the numerical integration including $n_p$ third-body perturbers. In addition, we observed how the MOID has a short-period component of the same order of magnitude of $\Delta\xi$. For this reason we include the amplitude in the MOID threshold and search for deep encounters within this distance. The criteria to determine if a point of the B-plane $(\xi, \zeta)$ is part of the keyhole is obtained similarly: An updated necessary condition on $\xi$ and the same computation of the timing component $\zeta$ as in Section 6.5.1. The necessary condition on $\xi$ becomes:

$$|\xi''| = |\xi' + \Delta\xi| \leq R_c + \Delta_{SP} \tag{6.28}$$

Along the resonant circle the post-encounter semi-major axis remains constant (See eq. 6.11). However, the rest of post-encounters elements depend on the location of the pre-image within the resonant circle. Figure 6.6 shows the variation $\Delta\xi$ along two resonant circles using the two propagation methods. Within the circle there are regions clearly distinguishable by having similar values of $\Delta\xi$. This observation could allow the reduction of the computational burden of propagating numerous trajectories in these regions of the resonant circle.

The short-period perturbations have a very important role in the propagation of the MOID, as described in section 6.4. We show this effect in Figure 6.3, where we observe the propagation in time for a single point of the resonant circle. However, within the same resonant encounter circle, it is possible to find a certain agreement between both theories. We further observe this in Figure

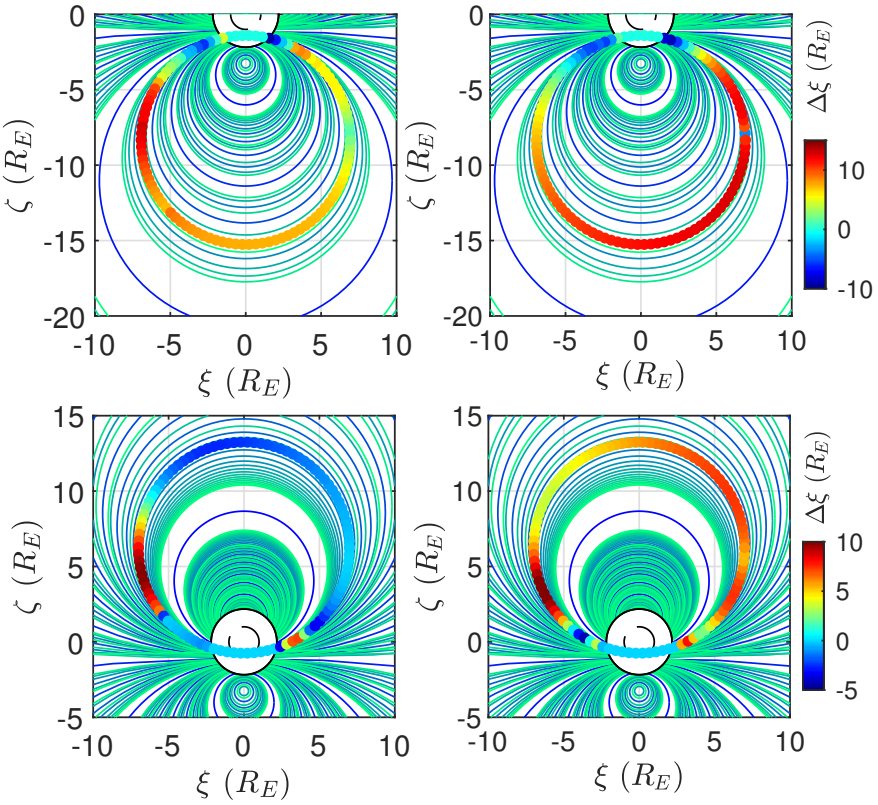


Figure 6.6 Variation of the MOID ($R_E$) at the 2029 encounter of Apophis around the resonant circles $\{k = 11, h = 15\}$ (top) and $\{k = 12, h = 13\}$ (bottom), using semi-analytical propagation (left) and numerical integration (right).

6.6, where the variation of the MOID $\Delta\xi$ is computed using both methods. In some regions of the circle the semi-analytical propagation matches the variation obtained numerically. In other regions the variation obtained numerically is larger than predicted. Note that the amplitude of the short-period component should include the variations found within this resonant circle.

These results show the potential of the semi-analytical secular model to be used for preliminary analysis. However, this agreement needs to be taken carefully since it depends on the flyby geometry and on the resonant circle.

The variation $\Delta\xi$ is computed in every point of the resonant circle to determine the modified keyholes. Figure 6.7 shows the modified keyholes computing the variation $\Delta\xi$ with the semi-analytical model and the amplitude of the short-period as margin, and numerical integration. A large fraction of the keyholes that were obtained assuming constant heliocentric elements between

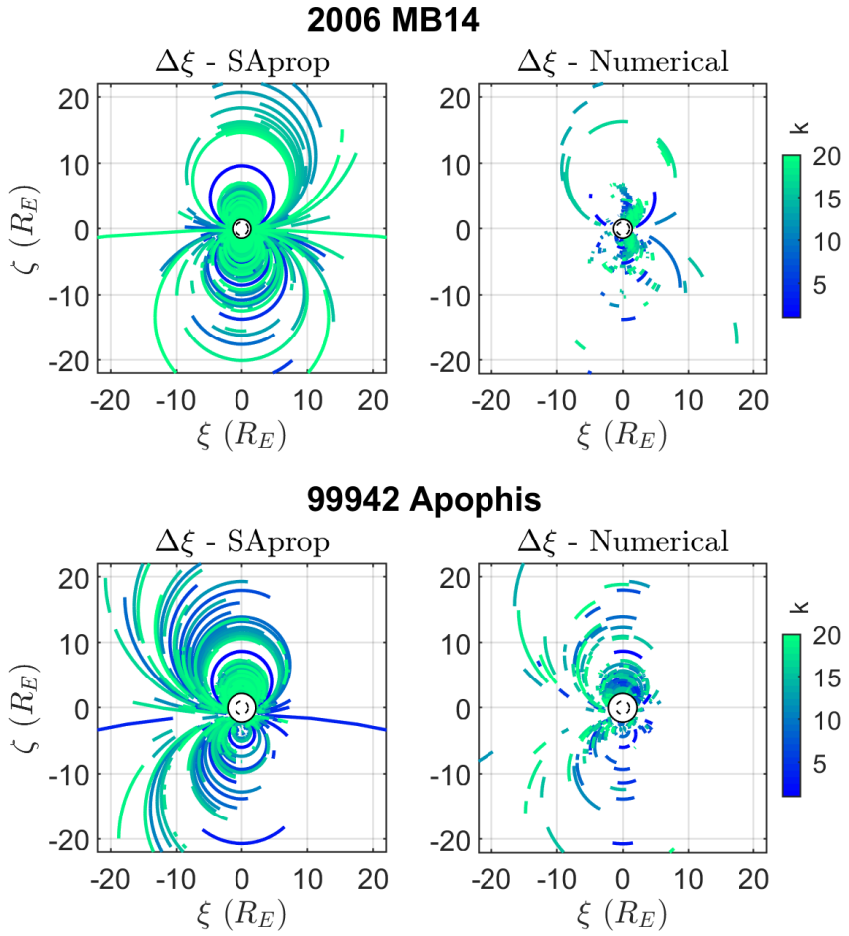


Figure 6.7 Modified keyholes of the Earth flyby of 99942 Apophis and 2006 MB14.

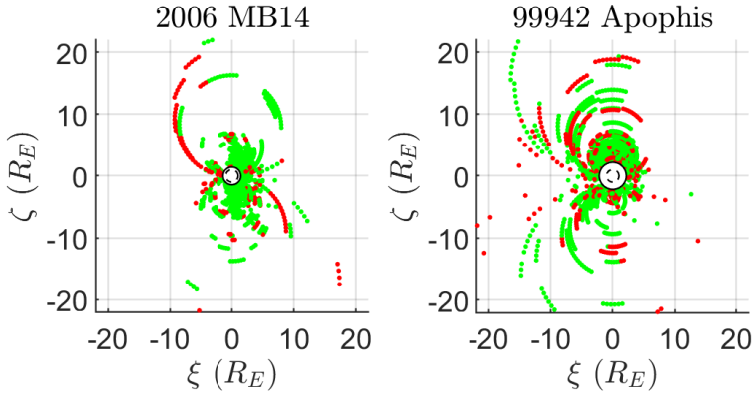


Figure 6.8 Success finding numerical keyholes by propagating the MOID between encounters semi-analytically for 99942 Apophis and 2006 MB14.

encounters disappear or are translated to a different region of the B-plane.

When we set up the threshold distance to a deep encounter (as given by equation 6.28), we generate additional keyhole regions further from the planet, which is a more conservative estimate. Thus, in both examples we find that the semi-analytical method accounting for the short-period amplitude highlights more regions.

Figure 6.8 shows the keyholes found numerically color coded by whether or not the semi-analytical propagation tool actually found them. We can see how the case of 2006 MB14, with a MOID evolution dominated by the secular drift is better captured by the semi-analytical propagation tool.

### 6.5.3 Computational speed-up

The secular propagation represents a significant speed-up as opposite to computing $\Delta\xi$ numerically. The computation of the modified keyholes requires the propagation of a grid of points among each of the resonant circles for $k$ Earth periods. In this work we discretize the resonant circles in 100 points. For up to $k = 20$ Earth periods, we find 226 and 393 resonant circles respectively for 99942 Apophis and 2006 MB14.

We computed the modified keyholes using the two methods with the same 2.5GHz Intel Core i7 processor. In comparison, computing the modified keyholes of 2006 MB14 with the secular method was 600x faster. In the case of 99942 Apophis, the speed-up was of 540x. Thus, from the computational cost standpoint the secular model is significantly superior. Using the semi-analytical propagation tool, which takes into account the close encounters, the speed-up is about x150, a considerable speed-up compared to numerical integration.

## 6.6 Conclusions

The extended Öpik theory of close encounters assumes that the orbit elements of the asteroid remain constant between close encounters. We show how the variation in the orbit elements between encounters projected to the MOID is of the order of magnitude of several Earth radii. This finding motivates the modelling of non-Keplerian effects in the heliocentric orbit of the asteroid in the preliminary analysis of keyholes. We propose three propagation methods to model these effects: a secular analytical model, semi-analytical propagation considering planetary close encounters, and numerical integration. Through this propagation we model the variation of the MOID to obtain a modified location of the keyholes in the B-plane of the asteroid initial close encounter. We find significant displacements of the keyholes, with new sections of the B-plane for further study and regions absent of keyholes.

We model two asteroid flybys: the 2029 encounter of 99942 Apophis and the 1985 encounter of 2006 MB14. In both cases the Earth MOID has a short-period oscillation amplitude of a few Earth Radii. In the case of 99942 Apophis, the perturbations between resonant encounters cause significantly larger variations in the Earth MOID, challenging the applicability of the lower fidelity models.

On the other hand, in order to reduce the computational cost of the numerical approach, propagating only selected points in the resonant circles could help reduce the required time significantly. The presented approach is to uniformly distribute in space the points of the circle so that we can still capture regional behaviors. A direct application would be to make the selection based on the flyby uncertainty if available. In such case, the search for modified keyholes could be based on the intersections between the known line of variations and the resonant circles.

These results encourage the study of additional asteroids to explore the potential of finding modified keyholes without the use of large scale Monte Carlo simulations. We prove that the changes in $\Delta\xi$ can be significant and that an analytical secular model can partially capture the dynamics of the MOID, especially after quantifying the amplitude of the short-period oscillations.

The shallow close encounters between encounters can also contribute significantly to the overall MOID evolution and the keyholes during close encounters.

The proposed methodology leaves room to improve our dynamics models to ensure higher fidelity of the results. For example, the effect of Earth eccentricity in the MOID propagation is left outside the scope of the present work. Further, the analytical condition on $\zeta''$ for a keyhole could be corrected by the variation in elements between encounters. Here we mention a few possible improvements of the dynamical models. Most importantly, we show the challenging topology of the $\Delta\xi$ variations among the B-plane, which should be addressed in future work.

# Chapter 7

# Conclusions

This dissertation explored semi-analytical methods to analyze the orbits of near-Earth asteroids. The motion of NEOs in the inner solar system is characterized by the presence of planetary close encounters, with a range of implications on the orbit and the physical properties of the asteroid. We developed a rapid propagation tool consisting in using an analytical solution for the 100,000-year timescale secular effect from Jupiter. Then, we use a numerical scheme for the evaluation of planetary close encounters, with significant effects in timescales of days. This allows an overall fast propagation while gathering statistics of close encounters and the growth in uncertainty.

Chapter 2 elaborates on the methodology and long-term stochastic characterization of near-Earth asteroids. The solution of the long-term perturbation that we modeled is valid in a range of semi-major axes, eccentricity and inclination that we defined by having a small error in the secular frequencies. A natural extension of this dissertation would be to broaden this range, for example, by including other analytical solutions for different regions of near-Earth space such as the Lidov-Kozai effect.

As soon as we consider time-scales beyond the hundreds-to-thousands of years, we can utilize the fact that the MOID must be small for deep close encounters to be possible. Depending on the application we can use different methods to estimate the probability of such encounters to occur. First, we can sample many particles and propagate them in a Monte Carlo simulation, for which a rapid tool such as the one developed in this dissertation becomes a powerful tool. If the orbit must be propagated numerically, we can use analytical approximations of the probability that exploit

the fact that the orbit eventually becomes stochastic.

In chapter 3 we estimate the probability of experiencing a disruptive close encounter by the Janus and DART mission targets. This analysis was a contribution to the overall understanding of the dynamics of binary asteroids, in which we quantify the frequency of this perturbation. Within the context of the evolution of binary asteroid systems, these should be leveraged with other effects such as dissipation or binary YORP. In the meantime, the prediction of recent low-MOID windows for close encounters can inform whether or not planetary close encounters are a plausible explanation for the chaotic state of binary asteroid orbits.

Another dynamic physical property observed in nature that we contributed to explain is the distribution of obliquities of asteroids, as analyzed in chapter 4. Near-Earth space is a natural benchmark for the understanding of thermal torques. Near Earth we are able to observe more smaller objects, which experience a stronger effect by stronger torques and smaller inertias. The small asteroids that have been explored are not exactly in the equilibrium configurations predicted by YORP theories. We show how the fact that the orbit is experiencing planetary close encounters could be a reason why this is. This step in the understanding of the rotational dynamics of NEOs should be combined with models for the evolution of the spin rate. For example, considering Tangential YORP, which in come cases is expected to be dominant and bring asteroids to equilibrium rotation periods.

The last chapters of this dissertation continue to characterize the frequency of planetary close encounters. In chapters 5 and 6, the analysis is done for planetary defense. We exploit the fact that a low Earth MOID is a necessary condition for a collision. In chapter 5 we use it to push further than typical impact hazard analyses. While this approach is not as rigorous as the direct computation of the probability of collision, it allowed us to rule out the risk of large fractions of the km-sized and PHA population for an order of magnitude longer than previously analyzed. Future work should address the smaller asteroid populations with a higher uncertainty in their orbit solutions.

In chapter 6 we aim to contribute to the understanding of NEO orbital dynamics for impact hazard assessment. We develop a correction to the analytical extended Öpik theory to find keyholes by modeling the evolution of the MOID between close encounters. We find that additional complexity should be added to the lower fidelity models to fully recreate the dynamical landscape of the search for keyholes in the B-plane.

Overall, throughout this dissertation we explored the potential of analytical, semi-analytical and numerical methods to model a few of the dynamical properties of NEOs. Even in the era of exponential growth of computational power, the exploration of these lower-fidelity theories continues to provide valuable insight of the underlying dynamics. Our improved understanding will continue to ease the analysis of large populations and databases. Especially, as we continue to survey the Solar System looking for answers to our most fundamental questions.

## Bibliography


E.M. Alessi and J.P. Sánchez. Semi-Analytical Approach for Distant Encounters in the Spatial Circular Restricted Three-Body Problem. Journal of Guidance, Control, and Dynamics, 39: Number 2, 2015. ISSN 0731-5090. doi: 10.2514/1.g001237.

R. Armellin, P Di Lizia, M. Berz, and K. Makino. Computing the critical points of the distance function between two Keplerian orbits via rigorous global optimization. Celestial Mechanics and Dynamical Astronomy, 2010. ISSN 09232958. doi: 10.1007/s10569-010-9281-7.

R. Ballouz, K.J. Walsh, O.S. Barnouin, D.N. DellaGiustina, M. Al Asad, E.R. Jawin, M.G. Daly, W.F. Bottke, P. Michel, C. Avdellidou, et al. Bennu's near-Earth lifetime of 1.75 million years inferred from craters on its boulders. Nature, 587(7833):205–209, 2020.

F. Benitez and T. Gallardo. The relativistic factor in the orbital dynamics of point masses. Celest Mech Dyn Astr, 101:289–307, 2008. doi: 10.1007/s10569-008-9146-5.

P. Birtwhistle. Lightcurves for Five Close Approach Asteroids. Minor Planet Bulletin, 36(4): 186–187, October 2009.

W. F. Bottke, A. Morbidelli, R. Jedicke, J. Petit, H. F. Levison, P. Michel, and T. S. Metcalfe. Debiased orbital and absolute magnitude distribution of the near-earth objects. Icarus, 156(2): 399–433, 2002.

W. F. Bottke, D. Vokrouhlickỳ, D. P. Rubincam, and D. Nesvornỳ. The Yarkovsky and YORP effects: Implications for asteroid dynamics. Annu. Rev. Earth Planet. Sci., 34:157–191, 2006.

E. Bowell and K. Muinonen. Earth-crossing asteroids and comets: Groundbased search strategies. Hazards due to Comets and Asteroids, 149, 1994.

D. Brouwer and G. M. Clemence. Secular Perturbations. In Methods of Celestial Mechanics, page 610. Academic Press, 1961. doi: 10.1016/b978-1-4832-0075-0.50013-7.

G. M. Brown and D. J. Scheeres. Temporal evolution of the dynamical environment around asteroid (101955) Bennu. Icarus, page 115632, 2023.

A.B. Chamberlin, S.R. Chesley, P.W. Chodas, J.D. Giorgini, M.S. Keesey, R.N. Wimberly, and D.K. Yeomans. Sentry: An Automated Close Approach Monitoring System for Near-Earth Objects. In AAS/Division for Planetary Sciences Meeting Abstracts #33, volume 33 of AAS/Division for Planetary Sciences Meeting Abstracts, page 41.08, November 2001.

J. E. Chambers. A hybrid symplectic integrator that permits close encounters between massive bodies. Monthly Notices of the Royal Astronomical Society, 304(4):793–799, 1999. ISSN 0035-8711. doi: 10.1046/j.1365-8711.1999.02379.x. URL https://doi.org/10.1046/j.1365-8711.1999.02379.x.

P. W. Chodas. Orbit uncertainties, keyholes, and collision probabilities. volume 31, page 111728.04, January 1999. URL https://ui.adsabs.harvard.edu/abs/1999BAAS...31R1117C. Conference Name: Bulletin of the American Astronomical Society ADS Bibcode: 1999BAAS...31R1117C.

A. B. Davis and D. J. Scheeres. High-fidelity modeling of rotationally fissioned asteroids. The Planetary Science Journal, 1(1):25, jun 2020. doi: 10.3847/PSJ/ab9a39. URL https://dx.doi.org/10.3847/PSJ/ab9a39.

A. Del Vigna, F. Guerra, and G. B. Valsecchi. Improving impact monitoring through Line Of Variations densification. Icarus, 351:113966, nov 2020. ISSN 0019-1035. doi: 10.1016/J.ICARUS.2020.113966.

L. Dones, B. Gladman, H. J. Melosh, W. B. Tonks, H. F. Levison, and M. Duncan. Dynamical Lifetimes and Final Fates of Small Bodies: Orbit Integrations vs ÖPik Calculations. Icarus, 142 (2):509–524, 1999. ISSN 00191035. doi: 10.1006/icar.1999.6220.

J. Fang and J. L. Margot. Binary asteroid encounters with terrestrial planets: Timescales and effects. Astronomical Journal, 2012. ISSN 00046256. doi: 10.1088/0004-6256/143/1/25.

P. Farinella, C. Froeschlé, C. Froeschlé, R. Gonczi, G. Hahn, A. Morbidelli, and G. B. Valsecchi. Asteroids falling into the Sun. Nature, 371:314–317, 1994. ISSN 00280836. doi: 10.1038/371314a0.

D. Farnocchia and S. R. Chesley. Apophis trajectory, impact hazard, and sensitivity to spacecraft contact. In Apophis T-7 Years (2022), 2022. URL https://www.hou.usra.edu/meetings/apophis2022/pdf/2007.pdf.

D. Farnocchia and S.R. Chesley. Assessment of the 2880 impact threat from Asteroid (29075) 1950 DA. Icarus, 229:321–327, 2014. ISSN 0019-1035. doi: https://doi.org/10.1016/j.icarus.2013.09.022. URL https://www.sciencedirect.com/science/article/pii/S0019103513004132.

D. Farnocchia and P. W. Chodas. A Recipe for Estimating the Frequency of Asteroid Close Approaches to Earth. Research Notes of the AAS, 5(11):257, nov 2021. doi: 10.3847/2515-5172/ac3519. URL https://dx.doi.org/10.3847/2515-5172/ac3519.

D. Farnocchia, S. R. Chesley, P. W. Chodas, M. Micheli, D. J. Tholen, A. Milani, G. T. Elliott, and F. Bernardi. Yarkovsky-driven impact risk analysis for asteroid (99942) Apophis. Icarus, 2013a. ISSN 00191035. doi: 10.1016/j.icarus.2013.02.020.

D. Farnocchia, S. R. Chesley, D. Vokrouhlický, A. Milani, F. Spoto, and W. F. Bottke. Near Earth Asteroids with measurable Yarkovsky effect. Icarus, 224:1–13, 5 2013b. ISSN 0019-1035. doi: 10.1016/J.ICARUS.2013.02.004.

D. Farnocchia, S. R. Chesley, A. Milani, G. F. Gronchi, and P. W. Chodas. Orbits, Long-Term Predictions, and Impact Monitoring, pages 815–834. University of Arizona Press, 2015. ISBN 9780816532131. URL http://www.jstor.org/stable/j.ctt18gzdvc.48.

D. Farnocchia, S. Eggl, P. W. Chodas, J. D. Giorgini, and S. R. Chesley. Planetary Encounter Analysis on the B-Plane: A Comprehensive Formulation. Celestial Mechanics and Dynamical Astronomy, 131(8):36, aug 2019. ISSN 0923-2958, 1572-9478. doi: 10.1007/s10569-019-9914-4.

D. Farnocchia, S. R. Chesley, Y. Takahashi, B. Rozitis, D. Vokrouhlický, B. P. Rush, N. Mastrodemos, B. M. Kennedy, R. S. Park, J. Bellerose, D. P. Lubey, D. Velez, A. B. Davis, J. P. Emery, J. M. Leonard, J. Geeraert, P. G. Antreasian, and D. S. Lauretta. Ephemeris and hazard assessment for near-Earth asteroid (101955) Bennu based on OSIRIS-REx data. Icarus, 369:114594, 2021. ISSN 0019-1035. doi: 10.1016/j.icarus.2021.114594.

W. M. Folkner, J. G. Williams, D. H. Boggs, R. S. Park, and P. Kuchynka. The Planetary and Lunar Ephemerides DE430 and DE431. Interplanet. Netw. Prog. Rep, 2014.

C. Froeschle, G. Hahn, R. Gonczi, A. Morbidelli, and P. Farinella. Secular Resonances and the Dynamics of Mars-Crossing and Near-Earth Asteroids. Icarus, 117(1):45–61, 1995. ISSN 0019-1035. doi: https://doi.org/10.1006/icar.1995.1141. URL https://www.sciencedirect.com/science/article/pii/S0019103585711414.

O. Fuentes-Munoz and D. J. Scheeres. Secular evolution of the MOID for Near-Earth Objects. In 2020 AAS/AIAA Astrodynamics Specialist Conference - Lake Tahoe, 2020a.

O. Fuentes-Munoz and D. J. Scheeres. Extremely long-term asteroid propagation. In AIAA Scitech 2020 Forum, Orlando, FL, 2020b. AIAA 2020-0464. URL https://doi.org/10.2514/6.2020-0464.

O. Fuentes-Munoz, A. Pedrós Faura, and D. Amato. Effect of non-Keplerian MOID evolution on preliminary keyhole analyses. In 7th IAA Planetary Defense Conference, page 223, April 2021.

O. Fuentes-Muñoz, A. J. Meyer, and D. J. Scheeres. Semi-analytical Near-Earth Objects Propagation: The Orbit History of (35107) 1991 VH and (175706) 1996 FG3. The Planetary Science Journal, 3(11):257, nov 2022. ISSN 2632-3338. doi: 10.3847/PSJ/ac83c6. URL https://iopscience.iop.org/article/10.3847/PSJ/ac83c6.

O. Fuentes-Muñoz and D. J. Scheeres. On the long-term hazardous nature of NEOs. In 2022 AIAA/AAS Astrodynamics Specialists Conference, Charlotte, NC, 2022.

O. Fuentes-Muñoz, D. J. Scheeres, D. Farnocchia, and R. S. Park. The Hazardous km-sized NEOs of the Next Thousands of Years. The Astronomical Journal, 166(1):10, jun 2023. doi: 10.3847/1538-3881/acd378. URL https://dx.doi.org/10.3847/1538-3881/acd378.

J. D. Giorgini, S. J. Ostro, L. A. M. Benner, P. W. Chodas, S. R. Chesley, R. S. Hudson, M. C. Nolan, A. R. Klemola, E. M. Standish, R. F. Jurgens, R. Rose, A. B. Chamberlin, D. K. Yeomans, and J.-L. Margot. Asteroid 1950 DA's Encounter with Earth in 2880: Physical Limits of Collision Probability Prediction. Science, 296(5565):132–136, 2002. doi: 10.1126/science.1068191. URL https://www.science.org/doi/abs/10.1126/science.1068191.

J.D. Giorgini and JPL Solar System Dynamics. NASA/JPL Horizons On-Line Ephemeris System, 2021. URL http://ssd.jpl.nasa.gov/?horizons.

B. J. Gladman, F. Migliorini, A. Morbidelli, V. Zappalà, P. Michel, A. Cellino, C. Froeschlé, H. F. Levison, M. Bailey, and M. Duncan. Dynamical lifetimes of objects injected into asteroid belt resonances. Science, 277(5323):197–201, 1997. ISSN 00368075. doi: 10.1126/science.277.5323.197.

O. Golubov and V. Lipatova. Analytic theory for the tangential YORP produced by the asteroid regolith. Astronomy & Astrophysics, 666:A146, 2022.

O. Golubov and D. J Scheeres. Systematic structure and sinks in the YORP effect. The Astronomical Journal, 157(3):105, 2019.

O. Golubov, D. J. Scheeres, and Y. N. Krugly. A three-dimensional model of tangential YORP. The Astrophysical Journal, 794:22, 9 2014. ISSN 1538-4357. doi: 10.1088/0004-637X/794/1/22. URL https://iopscience.iop.org/article/10.1088/0004-637X/794/1/22.

O. Golubov, V. Unukovych, and D. J. Scheeres. Limiting behavior of asteroid obliquity and spin using a semi-analytic thermal model of the YORP effect. The Astronomical Journal, 162(1):8, 2021.

M. Granvik, A. Morbidelli, R. Jedicke, B. Bolin, W. F. Bottke, E. Beshore, D. Vokrouhlický, D. Nesvorný, and P. Michel. Debiased orbit and absolute-magnitude distributions for near-Earth objects. Icarus, 312:181–207, 2018. ISSN 0019-1035. doi: 10.1016/j.icarus.2018.04.018.

R. Greenberg, A. Carusi, and G. B. Valsecchi. Outcomes of planetary close encounters: A systematic comparison of methodologies. Icarus, 1988. ISSN 10902643. doi: 10.1016/0019-1035(88)90125-X.

G. F. Gronchi. Generalized averaging principle and the secular evolution of planet crossing orbits. Celestial Mechanics and Dynamical Astronomy, 83:97–120, 2002.

G. F. Gronchi. An algebraic method to compute the critical points of the distance function between two Keplerian orbits. Celestial Mechanics and Dynamical Astronomy, 2005. ISSN 09232958. doi: 10.1007/s10569-005-1623-5.

G. F. Gronchi and A. Milani. Averaging on Earth-Crossing Orbits. Celestial Mechanics and Dynamical Astronomy, 71:109–136, 1998.

G. F. Gronchi and C. Tardioli. Secular evolution of the orbit distance and asteroid hazard. In EPSC-DPS Joint Meeting 2011, volume 2011, page 1472, October 2011.

G. F. Gronchi and C. Tardioli. The evolution of the orbit distance in the double averaged restricted 3-body problem with crossing singularities. Discrete, Continuous Dynamical Systems - B, 18(5): 1323–1344, 2013. doi: 10.3934/dcdsb.2013.18.1323.

G. F. Gronchi and G. Tommei. On the uncertainty of the minimal distance between two confocal Keplerian orbits. Discrete and Continuous Dynamical Systems - B, 7(4): 755–778, 2007. ISSN 1531-3492. doi: 10.3934/dcdsb.2007.7.755. URL /article/id/93cc3928-6b66-4c22-9ca5-812cf1e248e7.

A. W. Harris and P. W. Chodas. The population of near-earth asteroids revisited and updated. Icarus, 365:114452, 2021. ISSN 0019-1035. doi: https://doi.org/10.1016/j.icarus.2021.114452. URL https://www.sciencedirect.com/science/article/pii/S0019103521001342.

J. M. Hedo, M. Ruíz, and J. Peláez. On the minimum orbital intersection distance computation: A new effective method. Monthly Notices of the Royal Astronomical Society, 2018. ISSN 13652966. doi: 10.1093/mnras/sty1598.

J. M. Hedo, E. Fantino, M. Ruíz, and J. Peláez. Minimum orbital intersection distance, an asymptotic approach. Astronomy & Astrophysics, 2020. ISSN 0004-6361. doi: 10.1051/0004-6361/201936502.

D. C. Heggie and F. A. Rasio. The effect of encounters on the eccentricity of binaries in clusters. Monthly Notices of the Royal Astronomical Society, 282(3):1064–1084, 1996. doi: 10.1093/mnras/282.3.1064.

P. Jenniskens, M. H. Shaddad, D. Numan, S. Elsir, A.M. Kudoda, M. E. Zolensky, L. Le, G.A. Robinson, J.M. Friedrich, D. Rumble, et al. The impact and recovery of asteroid 2008 TC3. Nature, 458(7237):485–488, 2009.

Y. JeongAhn and R. Malhotra. Simplified derivation of the collision probability of two objects in independent Keplerian orbits, 2017. ISSN 23318422.

R. L. Jones, C. T. Slater, J. Moeyens, L. Allen, T. Axelrod, K. Cook, Željko, M. Jurić, J. Myers, and C. E. Petry. The Large Synoptic Survey Telescope as a Near-Earth Object discovery machine, 2018. ISSN 10902643.

JPL Solar System Dynamics and Center for NEO Studies (CNEOS). JPL Small-Body Database Search Engine, 2021.

H. Kinoshita and H. Nakai. Analytical Solution of the Kozai Resonance and its Application. Celestial Mechanics and Dynamical Astronomy 1999 75:2, 75:125–147, 1999. ISSN 1572-9478. doi: 10.1023/A:1008321310187. URL https://link.springer.com/article/10.1023/A:1008321310187.

H. Kinoshita and H. Nakai. General solution of the Kozai mechanism. Celestial Mechanics and Dynamical Astronomy, 2007. ISSN 09232958. doi: 10.1007/s10569-007-9069-6.

Y. Kozai. Secular perturbations of asteroids with high inclination and eccentricity. The Astronomical Journal, 67:591–598, 1962.

A. La Spina, P. Paolicchi, A. Kryszczyńska, and P. Pravec. Retrograde spins of near-Earth asteroids from the Yarkovsky effect. Nature, 428(6981):400–401, 2004.

M.L. Lidov. The evolution of orbits of artificial satellites of planets under the action of gravitational perturbations of external bodies. Planetary and Space Science, 9(10):719–759, 1962. ISSN 0032-0633. doi: https://doi.org/10.1016/0032-0633(62)90129-0. URL https://www.sciencedirect.com/science/article/pii/0032063362901290.

S.C. Lowry, P.R. Weissman, S.R. Duddy, B. Rozitis, A. Fitzsimmons, S.F. Green, M.D. Hicks, C. Snodgrass, S.D. Wolters, S.R. Chesley, et al. The internal structure of asteroid (25143) Itokawa as revealed by detection of YORP spin-up. Astronomy & Astrophysics, 562:A48, 2014.

J. McMahon and D. Scheeres. Secular orbit variation due to solar radiation effects: a detailed model for BYORP. Celestial Mechanics and Dynamical Astronomy, 106:261–300, 2010.

A. J. Meyer and D. J. Scheeres. The effect of planetary flybys on singly synchronous binary asteroids. Icarus, 367:114554, 2021. ISSN 0019-1035. doi: https://doi.org/10.1016/j.icarus.2021.114554. URL https://www.sciencedirect.com/science/article/pii/S001910352100227X.

A. J. Meyer, D. J. Scheeres, S. Naidu, L. Benner, P. Pravec, and P. Scheirich. Modeling Fully Coupled Dynamics of Janus Binary Asteroid Mission Targets. In AAS/Division of Dynamical Astronomy Meeting, volume 53 of AAS/Division of Dynamical Astronomy Meeting, page 405.06, June 2021.

P. Michel and C. Froeschlé. The location of linear secular resonances for semimajor axes smaller than 2 AU. Icarus, 1997. ISSN 00191035. doi: 10.1006/icar.1997.5727.

P. Michel, P. Farinella, and C. Froeschlé. The orbital evolution of the asteroid Eros and implications for collision with the Earth. Nature, 380(6576):689–691, 1996a.

P. Michel, C. Froeschlé, and P. Farinella. Dynamical Evolution of Neas: Close Encounters, Secular Perturbations and Resonances. In H Rickman and M J Valtonen, editors, Worlds in Interaction: Small Bodies and Planets of the Solar System, pages 151–164, Dordrecht, 1996b. Springer Netherlands. ISBN 978-94-009-0209-1.

P. Michel, C. Froeschlé, and P. Farinella. Secular dynamics of asteroids in the inner solar system. Celestial Mechanics and Dynamical Astronomy, 69:133–147, 1997. ISSN 09232958. doi: 10.1007/978-94-017-1321-4-11.

P. Michel, A. Morbidelli, and W. F. Bottke. Origin and dynamics of Near Earth Objects. Comptes Rendus Physique, 6(3):291–301, 2005. ISSN 16310705. doi: 10.1016/j.crhy.2004.12.013.

A. Milani and Z. Knežević. Secular perturbation theory and computation of asteroid proper elements. Celestial Mechanics and Dynamical AStronomy, 49:347–411, 1990. ISSN 15729478. doi: 10.1007/BF00049444.

A. Milani, M. Carpino, G. Hahn, and A. M. Nobili. Dynamics of planet-crossing asteroids: Classes of orbital behavior. Project SPACEGUARD. Icarus, 78(2):212–269, 1989. ISSN 10902643. doi: 10.1016/0019-1035(89)90174-7.

A. Milani, S. R. Chesley, M. E. Sansaturio, G. Tommei, and G. B. Valsecchi. Nonlinear impact monitoring: Line of variation searches for impactors. Icarus, 2005. ISSN 00191035. doi: 10.1016/j.icarus.2004.09.002.

A. Morbidelli and D. Vokrouhlickỳ. The Yarkovsky-driven origin of near-Earth asteroids. Icarus, 163(1):120–134, 2003.

A. Morbidelli, R. Brasser, K. Tsiganis, R. Gomes, and H. F. Levison. Constructing the secular architecture of the solar system. Astronomy and Astrophysics, 507:1053–1065, 2009. ISSN 00046361. doi: 10.1051/0004-6361/200912876.

C. D. Murray and S. F. Dermott. Solar System Dynamics. Cambridge University Press, 2000. doi: 10.1017/cbo9781139174817.

D. Nesvorný and W. F. Bottke. Detection of the Yarkovsky effect for main-belt asteroids. Icarus, 170(2):324–342, aug 2004. ISSN 0019-1035. doi: 10.1016/J.ICARUS.2004.04.012.

E. J. Öpik. Collision Probabilities with the Planets and the Distribution of Interplanetary Matter. Proceedings of the Royal Irish Academy. Section A: Mathematical and Physical Sciences, 1951.

E. J. Öpik. Interplanetary encounters: close-range gravitational interactions. Developments in solar system- and space science. Elsevier Scientific Pub. Co., 1976. ISBN 9780444413710. URL https://books.google.com/books?id=-HXvAAAAMAAJ.

S. J. Ostro, J. Margot, L. Benner, J. D. Giorgini, D. J. Scheeres, E. G. Fahnestock, S. B. Broschart, J. Bellerose, M. C. Nolan, C. Magri, P. Pravec, P. Scheirich, R. Rose, R. F. Jurgens, E. M. De Jong, and S. Suzuki. Radar Imaging of Binary Near-Earth Asteroid (66391) 1999 KW4. Science, 314(5803):1276–1280, 2006. doi: 10.1126/science.1133622. URL https://www.science.org/doi/abs/10.1126/science.1133622.

Michel P. and F. Thomas. The Kozai resonance for near-Earth asteroids with semimajor axes smaller than 2 AU. Astronomy and Astrophysics, 1996. ISSN 00046361.

R. S. Park, W. M. Folkner, J. G. Williams, and D. H. Boggs. The JPL Planetary and Lunar Ephemerides DE440 and DE441. The Astronomical Journal, 161(3), 2021. ISSN 0004-6256. doi: 10.3847/1538-3881/abd414.

P. Pokorný and D. Vokrouhlický. Öpik-type collision probability for high-inclination orbits: Targets on eccentric orbits. Icarus, 2013. ISSN 00191035. doi: 10.1016/j.icarus.2013.06.015.

P Pravec, P Scheirich, P Kušnirák, K Hornoch, A Galád, SP Naidu, DP Pray, J Világi, Š Gajdoš, L Kornoš, et al. Binary asteroid population. 3. secondary rotations and elongations. Icarus, 267: 267–295, 2016.

H. Rein and D. S. Spiegel. IAS15: A fast, adaptive, high-order integrator for gravitational dynamics, accurate to machine precision over a billion orbits. Monthly Notices of the Royal Astronomical Society, 2014. ISSN 13652966. doi: 10.1093/mnras/stu2164.

D. C. Richardson, H. F. Agrusa, B. Barbee, W. F. Bottke, A. F. Cheng, S. Eggl, F. Ferrari, M. Hirabayashi, Ö. Karatekin, J. McMahon, et al. Predictions for the Dynamical States of the Didymos System before and after the Planned DART Impact. The Planetary Science Journal, 3 (7):157, jul 2022. doi: 10.3847/PSJ/ac76c9. URL https://dx.doi.org/10.3847/PSJ/ac76c9.

A. S. Rivkin and A. F. Cheng. Planetary defense with the Double Asteroid Redirection Test (DART) mission and prospects. nature communications, 14(1):1003, 2023.

J. Roa, D. Farnocchia, and S. R. Chesley. A Novel Approach to Asteroid Impact Monitoring. The Astronomical Journal, 162(6):277, 2021. ISSN 1538-3881. doi: 10.3847/1538-3881/ac193f. URL https://doi.org/10.3847/1538-3881/ac193f.

A Roy. Orbital Motion, Fourth Edition. Routledge, 2004. doi: 10.1201/9781420056884.

D. P. Rubincam. Radiative spin-up and spin-down of small asteroids. Icarus, 148(1):2–11, 2000.

P. Sánchez and D. J. Scheeres. Disruption patterns of rotating self-gravitating aggregates: A survey on angle of friction and tensile strength. Icarus, 271:453–471, 2016.

D. J. Scheeres. Rotational fission of contact binary asteroids. Icarus, 189(2):370–385, 2007.

D. J. Scheeres. Orbital motion in strongly perturbed environments: applications to asteroid, comet and planetary satellite orbiters. Springer, 2016.

D. J. Scheeres, E. G. Fahnestock, S. J. Ostro, J.-L. Margot, L. A. M. Benner, S. B. Broschart, J. Bellerose, J. D. Giorgini, M. C. Nolan, C. Magri, P. Pravec, P. Scheirich, R. Rose, R. F. Jurgens, E. M. De Jong, and S. Suzuki. Dynamical Configuration of Binary Near-Earth Asteroid (66391) 1999 KW4. Science, 314(5803):1280–1283, 2006. doi: 10.1126/science.1133599. URL https://www.science.org/doi/abs/10.1126/science.1133599.

D.J. Scheeres and R.W. Gaskell. Effect of density inhomogeneity on YORP: The case of Itokawa. Icarus, 198(1):125–129, 2008.

D.J. Scheeres, M. Abe, M. Yoshikawa, R. Nakamura, R.W. Gaskell, and P.A. Abell. The effect of YORP on Itokawa. Icarus, 188(2):425–429, 2007.

D.J. Scheeres, J.W. McMahon, E. Bierhaus, J. Wood, L. Benner, C. Hartzell, P. Hayne, J. Hopkins, R. Jedicke, L. Le Corre, A. Meyer, S. Naidu, P. Pravec, M. Ravine, and K. Sorli. Janus: A NASA SIMPLEx mission to explore two NEO Binary Asteroids. Bulletin of the AAS, 52(6), 10 2020. URL https://baas.aas.org/pub/2020n6i217p06. https://baas.aas.org/pub/2020n6i217p06.

P. Scheirich, P. Pravec, P. Kušnirák, K. Hornoch, J. McMahon, D.J. Scheeres, D. Čapek, D.P. Pray, H. Kučáková, A. Galád, J. Vraštil, Yu N. Krugly, N. Moskovitz, L.D. Avner, B. Skiff, R.S. McMillan, J.A. Larsen, M.J. Brucker, A.F. Tubbiolo, W.R. Cooney, J. Gross, D. Terrell, O. Burkhonov, K.E. Ergashev, Sh.A. Ehgamberdiev, P. Fatka, R. Durkee, E. Lilly Schunova, R. Ya Inasaridze, V.R. Ayvazian, G. Kapanadze, N.M. Gaftonyuk, J.A. Sanchez, V. Reddy, L. McGraw, M.S. Kelley, and I.E. Molotov. A satellite orbit drift in binary near-Earth asteroids (66391) 1999 KW4 and (88710) 2001 SL9 — Indication of the BYORP effect. Icarus, 360: 114321, 2021. ISSN 0019-1035. doi: https://doi.org/10.1016/j.icarus.2021.114321. URL https://www.sciencedirect.com/science/article/pii/S0019103521000208.

L. F. Shampine and M. W. Reichelt. The MATLAB ODE suite. SIAM journal on scientific computing, 18(1):1–22, 1997.

S. S. Sheppard, D. J. Tholen, P. Pokornỳ, M. Micheli, I. Dell'Antonio, S. Fu, C. A. Trujillo, R. Beaton, S. Carlsten, A. Drlica-Wagner, et al. A Deep and Wide Twilight Survey for Asteroids Interior to Earth and Venus. The Astronomical Journal, 164(4):168, sep 2022. doi: 10.3847/1538-3881/ac8cff. URL https://dx.doi.org/10.3847/1538-3881/ac8cff.

SSD/CNEOS API Service. SSD/CNEOS Small-Body DataBase API, 2021. URL https://ssd.jpl.nasa.gov/tools/sbdb_lookup.

G. Tancredi. Chaotic dynamics of planet-encountering bodies. Celestial Mechanics and Dynamical Astronomy, 70(3):181–200, 1998. ISSN 09232958. doi: 10.1023/A:1008331422678.

C. Tardioli, D. Farnocchia, B. Rozitis, D. Cotto-Figueroa, S. R. Chesley, T. S. Statler, and M. Vasile. Constraints on the near-Earth asteroid obliquity distribution from the Yarkovsky effect. Astronomy and Astrophysics, 608, 2017. ISSN 14320746. doi: 10.1051/0004-6361/201731338.

S. Tardivel, P. Sánchez, and D. J. Scheeres. Equatorial cavities on asteroids, an evidence of fission events. Icarus, 304:192–208, 2018.

C. A. Thomas, S. P. Naidu, P. Scheirich, N. A. Moskovitz, P. Pravec, S. R. Chesley, A. S. Rivkin, D. J. Osip, T. A. Lister, L. Benner, et al. Orbital period change of Dimorphos due to the DART kinetic impact. Nature, 616(7957):448–451, 2023.

G. Tommei. Algoritmi per il monitoraggio di possibili impatti asteroidali. PhD thesis, Thesis, University of Pisa, Pisa, Italy, 2002.

G. B. Valsecchi, A. Milani, G. F. Gronchi, and S. R. Chesley. Resonant returns to close approaches: Analytical theory. Astronomy & Astrophysics, 408(3, September IV 2003):1179–1196, 2003. ISSN 0004-6361. doi: 10.1051/0004-6361:20031039.

G. B. Valsecchi, E. M. Alessi, and A. Rossi. An analytical solution for the swing-by problem. Celestial Mechanics and Dynamical Astronomy, 123:151–166, 2015. ISSN 15729478. doi: 10.1007/s10569-015-9631-6.

D. Vokrouhlický, A. Milani, and S. R. Chesley. Yarkovsky Effect on Small Near-Earth Asteroids: Mathematical Formulation and Examples. Icarus, 148(1):118–138, nov 2000. ISSN 0019-1035. doi: 10.1006/ICAR.2000.6469.

D Vokrouhlickỳ, WF Bottke, and D Nesvornỳ. The spin state of 433 Eros and its possible implications. Icarus, 175(2):419–434, 2005.

D. Vokrouhlický, P. Pokorný, and D. Nesvorný. Öpik-type collision probability for high-inclination orbits. Icarus, 2012. ISSN 00191035. doi: 10.1016/j.icarus.2012.02.021.

D. Vokrouhlický, D. Farnocchia, D. Čapek, S. R. Chesley, P. Pravec, P. Scheirich, and T. G. Müller. The Yarkovsky effect for 99942 Apophis. Icarus, 252:277–283, may 2015. ISSN 0019-1035. doi: 10.1016/J.ICARUS.2015.01.011.

D. Vokrouhlický, S. Breiter, D. Nesvorný, and W.F. Bottke. Generalized YORP evolution: Onset of tumbling and new asymptotic states. Icarus, 191(2):636–650, 2007. ISSN 0019-1035. doi: https://doi.org/10.1016/j.icarus.2007.06.002. URL https://www.sciencedirect.com/science/article/pii/S0019103507002631.

D. Vokrouhlický, W. F. Bottke, S. R. Chesley, D. J. Scheeres, and T. S. Statler. The Yarkovsky and YORP Effects, pages 509–532. University of Arizona Press, 2015. ISBN 9780816532131. URL http://www.jstor.org/stable/j.ctt18gzdvc.33.

D. Vokrouhlický and D. Čapek. YORP-Induced Long-Term Evolution of the Spin State of Small Asteroids and Meteoroids: Rubincam's Approximation. Icarus, 159(2):449–467, 2002. ISSN 0019-1035. doi: https://doi.org/10.1006/icar.2002.6918. URL https://www.sciencedirect.com/science/article/pii/S0019103502969186.

K. J. Walsh, D. C. Richardson, and P. Michel. Spin-up of rubble-pile asteroids: Disruption, satellite formation, and equilibrium shapes. Icarus, 220(2):514–529, 2012.

B. D. Warner, R. D. Stephens, and A. Carbognani. Analysis of the Slow Rotator (143651) 2003 QO104. Minor Planet Bulletin, 36(4):179–180, October 2009.

B. D. Warner, A. W. Harris, and P. Pravec. Asteroid Lightcurve Data Base (LCDB) Bundle V4.0. NASA Planetary Data System, 2021. doi: 10.26033/j3xc-3359. URL urn:nasa:pds:ast-lightcurve-database::4.0.

G. W. Wetherill. Collisions in the asteroid belt. Journal of Geophysical Research, 72(9):2429–2444, 1967.

C.A. Wirtanen. Minor planet circular. MPC 416, 1950.

J. Wisdom and M. Holman. Symplectic maps for the n-body problem. The Astronomical Journal, 102:1528–1538, 1991. ISSN 00046256. doi: 10.1086/115978.

T. Wiśniowski and H. Rickman. Fast geometric method for calculating accurate Minimum Orbit Intersection Distances. Acta Astronomica, 2013. ISSN 00015237.

# Appendix A

## Computation of Laplace coefficients

The expansion of the potential requires the computation of Laplace coefficients, as introduced by Laplace (1798). Brouwer and Clemence [1961], Murray and Dermott [2000] detail both the expansion and computation of coefficients. In the case of the expansion in equation 2.4:

$$\langle R_j \rangle = n_j a_j^2 \left[ \frac{1}{2} A_{jj} e_j^2 + \frac{1}{2} B_{jj} I_j^2 + \sum_{\substack{k=1 \\ k \neq j}}^{N} A_{jk} e_j e_k \cos\left(\varpi_j - \varpi_k\right) + B_{jk} I_j I_k \cos\left(\Omega_j - \Omega_k\right) \right]$$

The coefficients $A_{jk}$,$B_{jk}$,$B_{jj}$ and $A_{jj}$ are:

$$A_{jk} = -n_j \frac{1}{4} \frac{m_k}{m_c + m_j} \alpha_{jk} \bar{\alpha}_{jk} b_{3/2}^{(2)}\left(\alpha_{jk}\right) \tag{A.1}$$

$$B_{jk} = +n_j \frac{1}{4} \frac{m_k}{m_c + m_j} \alpha_{jk} \bar{\alpha}_{jk} b_{3/2}^{(1)}\left(\alpha_{jk}\right) \tag{A.2}$$

$$A_{jj} = \sum_{k=1, k \neq j}^{N} B_{jk} \tag{A.3}$$

$$B_{jj} = -\sum_{k=1, k \neq j}^{N} B_{jk} \tag{A.4}$$

The definition of Laplace coefficient is:

$$\frac{1}{2} b_s^{(k)}(\alpha) = \frac{1}{2\pi} \int_0^{2\pi} \frac{\cos\left(k\psi\right) d\psi}{\left(1 - 2\alpha \cos\psi + \alpha^2\right)^s} \tag{A.5}$$

This integral can be rewritten in a series expansion that simplifies the computation of the Laplace coefficients numerically as function of the rising factorial or Pochhammer symbol. However,

it is found to be computationally more efficient to compute the quadrature integral above. There are many recursion and derivative rules that avoid computing the coefficients based on the definition. These expressions use the nomenclature of $D$ being the derivative operator $\frac{\mathrm{d}}{\mathrm{d}\alpha}$.

$$b_{s+1}^{(j)} = \frac{s+j}{s}\frac{(1+\alpha^2)}{(1-\alpha^2)^2}b_s^{(j)} - \frac{2(j-s+1)}{s}\frac{\alpha}{(1-\alpha^2)^2}b_s^{(j+1)} \tag{A.6}$$

$$b_{s+1}^{(j+1)} = \frac{j}{j-s}\left(\alpha + \frac{1}{\alpha}\right)b_{s+1}^{(j)} - \frac{j+s}{j-s}b_{s+1}^{(j-1)} \tag{A.7}$$

$$Db_s^{(j)} = s\left(b_{s+1}^{(j-1)} - 2\alpha b_{s+1}^{(j)} + b_{s+1}^{(j+1)}\right) \tag{A.8}$$

$$D^n b_s^{(j)} = s\left(D^{n-1}b_{s+1}^{(j-1)} - 2\alpha D^{n-1}b_{s+1}^{(j)} + D^{n-1}b_{s+1}^{(j+1)} - 2(n-1)D^{n-2}b_{s+1}^{(j)}\right) \tag{A.9}$$

# Appendix B

## Initial Conditions and uncertainties

The initial conditions of the cases represented in this chapter and chapter 3 are found in table B.1. The elements of asteroids 1991 VH and 1996 FG3 were retrieved from HORIZONS [Giorgini and JPL Solar System Dynamics, 2021]. Using DE431 and SB431-N16. Orbit solution dates for real asteroids are respectively 2021 April 15, 2021 April 26 and 2021 July 1.

The statistical representation of the uncertainty in the orbit solutions can be done using the covariance matrix. This information is available for multiple asteroids in JPL's SBDB.[1] The covariance matrices for (35107) 1991 VH, (175706) 1996 FG3 and (65803) Didymos that are used in this work are found in tables B.2,B.3 and B.4.

[1] As extracted from JPL's Small-body Database Lookup (Date accessed: 2021-04-25) - Available for query at: `ssd.jpl.nasa.gov/tools/sbdb_lookup.html`

In the case of the artificial cases used to illustrate the long-term dynamics, we set the covariance matrix to be a diagonal matrix of 1e-6 in the Keplerian set $\{a, e, i, \Omega, \omega, \sigma\}$. While this is orders of magnitude larger than the uncertainties of (175706) 1996 FG3 and (35107) 1991 VH, the uncertainty without further observations increases exponentially after only tens of encounters. Thus, it is adequate for the studies in long-term simulations of this work. The individual particles are sampled considering a multidimensional normal distribution centered around the nominal values shown in Table B.1. Then, we use the Cholesky factorization of the covariance matrices to add the corresponding perturbation from the nominal.

Table B.1 Near-Earth objects used as example cases for the demonstration of the semi-analytical propagation tool.

| Asteroid | $a(au)$ | $e$ | $i$ (deg) | $\Omega$ (deg) | $\omega$ (deg) | $M_0$ (deg) | JD (TBD) |
|---|---|---|---|---|---|---|---|
| Case 1 | 1.1 | 0.15 | 10 | 90 | 90 | 90 | 2451545.0 |
| Case 2 | 1.2 | 0.35 | 40 | 90 | 90 | 90 | 2451545.0 |
| Case 3 | 1.3 | 0.5 | 10 | 90 | 270 | 90 | 2451545.0 |
| Case 4 | 0.95 | 0.07 | 20 | 90 | 90 | 90 | 2451545.0 |
| Case 5 | 0.9 | 0.25 | 15 | 90 | 90 | 90 | 2451545.0 |
| 1991 VH | 1.1373 | 0.14426 | 13.912 | 139.37 | 206.88 | 302.39 | 2456902.5 |
| 1996 FG3 | 1.0543 | 0.34987 | 1.9903 | 299.88 | 23.930 | 147.277 | 2454796.5 |
| Didymos | 1.6444 | 0.38370 | 3.4077 | 73.199 | 319.32 | 298.33 | 2459396.5 |

Table B.2 Initial covariance of the orbit of NEO binary (35107) 1991 VH [SSD/CNEOS API Service, 2021]. Using DE431 and SB431-N16 (Sol. Date: 2021 April 26)

| 1991 VH | e | q (au) | $t_p$ (TDB) | $\Omega$ (deg) | $\omega$ (deg) | $i$ (deg) |
|---|---|---|---|---|---|---|
| e | 3.0691e-16 | -3.5095e-16 | -8.8918e-14 | -7.2651e-15 | -5.2217e-14 | 3.6255e-15 |
| q (au) | -3.5095e-16 | 4.0175e-16 | 1.0484e-13 | 8.2268e-15 | 6.1722e-14 | -4.1006e-15 |
| $t_p$ (TDB) | -8.8918e-14 | 1.0484e-13 | 7.5479e-11 | -7.8662e-12 | 6.4146e-11 | -3.8102e-12 |
| $\Omega$ (deg) | -7.2651e-15 | 8.2268e-15 | -7.8662e-12 | 3.104e-11 | -3.4282e-11 | -4.876e-12 |
| $\omega$ (deg) | -5.2217e-14 | 6.1722e-14 | 6.4146e-11 | -3.4282e-11 | 8.1951e-11 | 1.9766e-12 |
| $i$ (deg) | 3.6255e-15 | -4.1006e-15 | -3.8102e-12 | -4.876e-12 | 1.9766e-12 | 8.4244e-12 |

Table B.3 Initial covariance of the orbit of NEO binary (175706) 1996 FG3 [SSD/CNEOS API Service, 2021]. Using DE431 and SB431-N16 (Sol. Date: 2021 April 26)

| 1996 FG3 | e | q (au) | $t_p$ (TDB) | $\Omega$ (deg) | $\omega$ (deg) | $i$ (deg) |
|---|---|---|---|---|---|---|
| e | 1.2362e-16 | -1.3026e-16 | 7.9966e-15 | -4.1649e-14 | 3.9787e-14 | -2.3726e-14 |
| q (au) | -1.3026e-16 | 1.3752e-16 | -9.0726e-15 | 4.7436e-14 | -4.5397e-14 | 2.5036e-14 |
| $t_p$ (TDB) | 7.9966e-15 | -9.0726e-15 | 2.9877e-12 | 6.6638e-11 | -6.6225e-11 | -2.4698e-12 |
| $\Omega$ (deg) | -4.1649e-14 | 4.7436e-14 | 6.6638e-11 | 7.0256e-09 | -6.9647e-09 | -6.8055e-11 |
| $\omega$ (deg) | 3.9787e-14 | -4.5397e-14 | -6.6225e-11 | -6.9647e-09 | 6.9046e-09 | 6.7284e-11 |
| $i$ (deg) | -2.3726e-14 | 2.5036e-14 | -2.4698e-12 | -6.8055e-11 | 6.7284e-11 | 6.7136e-12 |
| $i$ (deg) | 3.6255e-15 | -4.1006e-15 | -3.8102e-12 | -4.876e-12 | 1.9766e-12 | 8.4244e-12 |

Table B.4 Initial covariance of the orbit of NEO binary (65803) Didymos [SSD/CNEOS API Service, 2021]. Using DE431 and SB431-N16 (Sol. Date: 2021 July 1)

| 1991 VH | e | q (au) | $t_p$ (TDB) | $\Omega$ (deg) | $\omega$ (deg) | $i$ (deg) |
|---|---|---|---|---|---|---|
| e | 7.5835e-18 | -1.3289e-17 | -6.9723e-15 | 2.2832e-14 | -2.6868e-14 | -2.6164e-15 |
| q (au) | -1.3289e-17 | 2.4125e-17 | 1.3904e-14 | -3.9510e-14 | 4.6506e-14 | 4.5567e-15 |
| $t_p$ (TDB) | -6.9723e-15 | 1.3904e-14 | 3.6196e-11 | -2.9160e-11 | 3.5176e-11 | 3.4930e-12 |
| $\Omega$ (deg) | 2.2832e-14 | -3.9510e-14 | -2.9160e-11 | 9.3506e-11 | -1.0600e-10 | -1.1732e-11 |
| $\omega$ (deg) | -2.6868e-14 | 4.6506e-14 | 3.5176e-11 | -1.0600e-10 | 1.2093e-10 | 1.3246e-11 |
| $i$ (deg) | -2.6164e-15 | 4.5567e-15 | 3.4930e-12 | -1.1732e-11 | 1.3246e-11 | 1.7622e-12 |